An experimental and computational investigation of dynamic ductile fracture in stainless steel welds

by

Vasanth S. Kothnur

B. Tech., Mechanical Engineering, Indian Institute of Technology - Madras, 1995

M. S., Mechanical Engineering, Cornell University, 1997

A dissertation submitted in partial fulfillment of the
requirements for the Degree of Doctor of Philosophy
in the Division of Engineering at Brown University

Providence, Rhode Island

May, 2002

This dissertation by Vasanth S. Kothnur is accepted in its present form by the Division of Engineering as satisfying the dissertation requirement for the degree of Doctor of Philosophy.

Date 12/20/01

Professor R. J. Clifton, Advisor

Recommended to the Graduate Council

Date 12/20/01

Professor S. Briant, Reader

Date 12/20/01

Professor A. Needleman, Reader

Approved by the Graduate Council

Date 12/27/01

Peder J. Estrup
Dean of the Graduate School and Research

Vita

Vasanth S. Kothnur was born in Thirthahalli, Karnataka on the 12^{th} day of October, 1973. He graduated from P.S. Senior Secondary School, Madras in May of 1991. He then studied at the Indian Institute of Technology, Madras and graduated with a B. Tech. in Mechanical Engineering in May 1995. In September of 1995, he joined Cornell University as a graduate student in the Sibley School of Mechanical and Aerospace Engineering. While at Cornell, he majored in Materials and Manufacturing Engineering, minored in Theoretical and Applied Mechanics and held a Teaching Assistantship. He graduated with a Master of Science from Cornell University in August of 1997.

After completion of his Masters degree, Vasanth joined the graduate program at the Division of Engineering, Brown University. He majored in Solid Mechanics and minored in Materials Science and Applied Mathematics. While at Brown, he worked under the guidance of Prof. R. J. Clifton and was supported as a Research Assistant on a grant by the Office of Naval Research. He met is future wife, Saritha V. Kumar while at Brown. They were married on the 28^{th} of May, 2000.

Acknowledgements

I am deeply grateful to Prof. Clifton for his patient guidance during my graduate study at Brown. His enormous insight and intellect have been crucial for culmination of this thesis.

I would like to acknowledge Prof. Needleman and Prof. Briant for their valuable comments as readers of this thesis. I would also like to thank Richard Everett, Andy Geltmacher and Kirth Simmonds for their assistance with X-ray Tomography in Brookhaven.

I would like to thank Chris Bull, Alan Schwartzman, Brian Corkum, Reese Webb and Allan Rydberg for their critical input. Special thanks go to Laurenz Hermann for help with ABAQUS. I am grateful to Bob Dean, Raymond Pagliarini, Peter Neri and Charlie Vickers for the machining in Prince Laboratory. In addition, I would like to thank Peggy Mercurio, Lorayn Palumbo, Patricia Capece and Rosanne Smith for all the wonderful assistance over the last four years at Brown.

My fellow graduate students have had a significant influence on this thesis through many informal discussions I have had with them. My discussions with Amine Benzerga have been critical in my formulation of a computational ductile fracture model in Chapter 3. I would like to acknowledge Amy Wagoner, Nitin Bhate, Zhizhou Zhang, Ping Wang, Ram Krishnamurthy, Dnyanesh Pawaskar, Kedar Hardikar, Ashok Rajamani, Deepali Bhate, Reuben Doyoyo, Daniel Fridline, Seung-Yong Yang, Kevin

Duprey, Anand Padmanabhan and Narayanan Ramachandran for valuable discussions and for their friendship. Also, I would love to thank Srikanta Thirthapura and Ashok Rajamani for being such great room-mates over the last four years (and putting up with my cooking). They really made my stay at Brown enjoyable.

I want to acknowledge financial support from the Office of Naval Research which has funded my research assistantship at Brown.

This thesis has been made possible only because of endless support from my parents and from my wife Saritha. They have been essential for me to master the challenges of graduate school and help me sail through difficult times. It is to them that I dedicate this thesis.

To my family

Contents

List of Tables

List of Figures

Chapter 1

Introduction

The primary objective of this thesis is the study of dynamic ductile failure of stainless steel welded plates under high rate loading conditions. We will be concerned with the mechanics of high rate viscoplastic flow and fracture behavior of heterogeneous weldments. We will focus our attention on investigating the mechanical behavior of a superaustenitic AL6XN weld with a Nickel-based superalloy INCONEL-625 as the filler material. The experimental and computational tools developed as part of this investigation are expected to be widely applicable to understanding the micromechanics of failure in other metallic systems.

1.1 Background

The overall strength and deformation characteristics of weldments are controlled by the geometry of the joint and the mechanical properties of the base metal, the weld filler material and the heat-affected zone. The modeling of the plastic flow behavior and prediction of the failure response of welds is a difficult undertaking due to the heterogeneous nature of this underlying microstructure. The complex thermomechanical processing history can lead to the formation of metallurgical defects (porosity,

unwanted phase transformation products) which have a direct relation to the overall structural integrity of the weld. Therefore a detailed characterization of the mechanical properties and microstructure of the various material zones in the weldment is essential to develop a reliable tool to predict damage evolution under impact loading conditions.

Superaustenitic steels like NITRONIC-50 and AL6XN have recently been the focus of attention in the ship building community because of several attractive properties. In the past, they were unsuitable candidates because of their higher initial cost compared to other alloys like HY-80/HY-100. In recent years, the decrease in the cost of these stainless alloys have again brought them into consideration. They exhibit a far greater corrosion resistance (chloride pitting, crevice corrosion and stress-corrosion cracking) than the standard 300 series stainless alloys or their ferritic counterparts. The nonmagnetic nature of these alloys make them a compelling choice as a hull material. The reduced magnetic signature associated with such hulls would enable them to evade detection. In addition, the enhanced yield strength and fracture toughness of these superaustenitic steels make them a promising candidate as a hull material where they would be expected to withstand explosive impact loading under service conditions.

While a selected number of tests were carried out on NITRONIC-50, we will focus attention mainly on the mechanical behavior of AL6XN stainless steel welds. Due to the recent origin and availability of AL6XN welded plates, experimental data on their high strain rate behavior are scarce. Nemat-Nasser, Guo and Kihl (2000) have conducted high strain rate (upto 3500/sec) compression experiments on the base AL6XN material in a split-Hopkinson bar configuration. We will extend their experiments to the weld and heat-affected zones. While the dynamic compression response

of specimens prepared from the various material zones are indicative of the inhomogeneous nature of the welded joint, the dynamic failure response obtained under high rate tensile loading conditions are even more strongly sensitive to the underlying microstructure. As such, a combination of high rate compression and tension experiments provide a true measure of understanding of the mechanical properties of the welded joint.

Giovanola and Kirkpatrick (1993) have studied the ductile fracture of high strength steel T-weldments when subjected to impact loading. They decouple the effects of plastic flow and strain hardening from the progressive evolution of damage. Using a stress-triaxiality dependent critical strain failure criterion, they were able to qualitatively predict the dynamic failure response of steel weldments.

Hval, Thaulow, Lange, Hoydal and Zhang (1998) investigated the ductility and fracture behavior of Type 6005 and Type 6082 aluminum weldments under quasistatic loading conditions. They determined the flow properties of the various material zones in these weldments using weld thermal-simulated testing. Using a Gurson constitutive relation with a critical void volume fraction criterion, they were able to model the ductile failure of welded plates. However, their method of determining a critical void volume fraction for the different material zones in the weldment is questionable. Also, the results of finite element simulations of ductile fracture using a Gurson-type constitutive relation are known to be mesh sensitive. It is not quite clear how Hval *et al.* (1998) address this issue for modeling their complex weld geometries.

The use of Gurson-type constitutive models for modeling ductile fracture is now very well established. This constitutive modeling framework for damage evolution is particularly attractive because of its underlying roots in the micromechanics of void growth. The Gurson constitutive relation is endowed with a yield condition, a flow rule and evolution laws for void nucleation and growth. The onset of void coalescence

has been traditionally modeled by the use of a critical void volume fraction found by fitting numerical predictions to experimental data. Tvergaard and Needleman (1984) formulated a simple approach to model the micromechanics of void coalescence and flow localization by constructing a modified void volume fraction after the onset of coalescence. In this thesis, we will explore more recent efforts to model void coalescence by incorporating the rich geometry of the inter-void microstructure within a finite element framework.

Three-dimensional finite element simulations of ductile fracture have the potential to track the evolution of damage in the microstructure in remarkable detail. However, experimental investigation of damage evolution has lagged behind as it is typically limited to using either one-dimensional (e.g. measuring load-displacement relationships) or two-dimensional (e.g. analysis in a SEM/TEM) techniques. In order to understand the limits of current constitutive models of failure, it is essential that we have the ability to probe the microstructure of the material at a length scale relevant to the construction of the model. In this thesis, we explore the use of X-ray tomography to obtain volumetric images of voided microstructures. The use of tomographic investigative tools allows one to spatially reconstruct the internal microstructure of a material at various stages of its deformation and loading history. While the choice of a heterogeneous stainless steel weldment is not an optimal one for a fundamental study of application of X-ray tomography to experimental solid mechanics, we were limited by the constraints imposed by the engineering problem under investigation.

1.2 Organization of Thesis

In Chapter 2, we briefly review the microstructure and composition of the as received NITRONIC-50 and AL6XN stainless steel welded plates. We discuss the operation of a Kolsky bar (also referred to as the split-Hopkinson bar) system in a compression

configuration to study the dynamic flow response of the base metal, the weld material and the heat-affected zone. Results from an investigation of the dynamic failure response of specimens machined from the various material zones under high rate tensile loading in a novel Koksky bar system are presented in Chapter 2. Appendix A discusses details of stress wave propagation in a Kolsky bar. We then identify the dominant failure mechanisms in the base and weld material zones. As an attempt to reconstruct the microstructural events that precede catastrophic failure, we probe the fracture process zone of notched tensile specimens using X-ray Computed Microtomography. Chapter 2 presents an internal three-dimensional reconstruction of the damaged microstructure from a specimen loaded to incipient failure.

In Chapter 3, we present a theoretical and computational framework to model the various stages of dynamic ductile fracture in stainless steel weldments. A finite-deformation elastic-viscoplastic porous constitutive model is developed to model the flow and fracture response under high rate loading. We present an isotropic constitutive model to describe the high strain rate, large deformation strain hardening behavior of AL6XN and INCONEL-625. We describe the micromechanics of void nucleation, void growth and void coalescence. We analyze the onset of void coalescence through a plastic limit-load model and present details of its implementation. A framework is developed to integrate the accelerated material response from the onset of void coalescence to complete material failure. We present details of an implementation of this failure model as a user-material subroutine VUMAT in ABAQUS/Explicit. Appendix B describes the numerical integration of the material model prior to the onset of void coalescence. Appendix C describes the details of numerical integration of the material response and the evolution of the geometry of the voided microstructure after coalescence.

In Chapter 4, we present the results from a finite element study of the dynamic tensile response of specimens machined from the various material zones of an AL6XN/INCONEL-625 welded plate. We present results from a study of the sensitivity of numerical simulations of ductile fracture to progressive refinements in mesh size. A microstructural length scale is identified to construct a representative finite element model of the Kolsky bar tensile specimen. We conduct fully three-dimensional finite element simulations of the Kolsky bar fracture experiments described in Chapter 2. Results from a simulation of ductile fracture in a notched cylindrical specimen machined from the heat-affected zone are compared with corresponding observations of damage evolution obtained using X-ray tomography. Finally, Chapter 5 presents a discussion of the results of this study of the high rate flow and fracture behavior of stainless steel weldments.

Chapter 2

Experimental Characterization of High Strain Rate Deformation and Ductile Fracture in Stainless Steel Weldments

2.1 Materials

Raw material in the form of 0.5" thick stainless steel welded plates were obtained from the Carderock Division of the Naval Surface Warfare Center. Three different welded plates (referred to as P_A, P_B and P_C in this thesis) were received from the Navy. P_A was a NITRONIC-50 stainless steel welded plate, while P_B and P_C were AL6XN stainless steel welded plates. The cross-section of the three plates was polished and etched to reveal the design of the welded joint. Figure 2.1 shows a schematic of the plates P_A and P_B. Similarly, a schematic of the plate P_C is shown in Figure 2.2. The orientations R, W and T in Figures 2.1 and 2.2 refer to the rolling, weld and

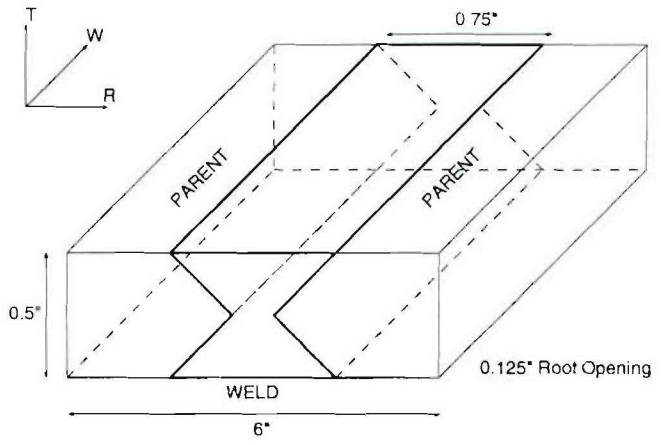

Figure 2.1: Stainless steel welded plates P_A and P_B: Design of the welded joint.

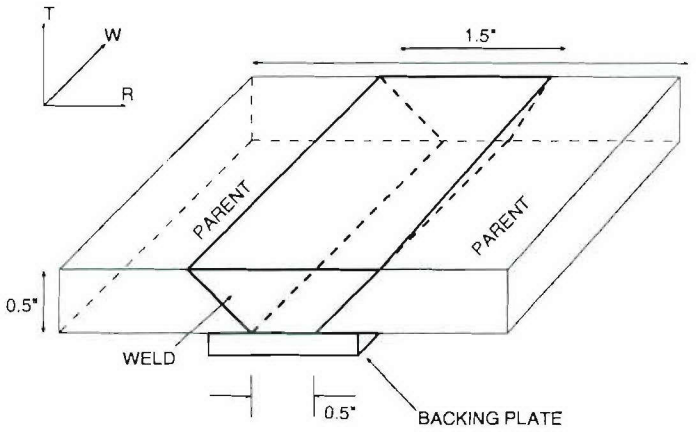

Figure 2.2: Stainless steel welded plate P_C: Design of the welded joint.

transverse directions respectively.

The base metal NITRONIC-50 in plate P_A is an austenitic alloy of composition shown in Table 2.1. A filler material of type ER 209 manufactured by Astrolite Alloys was used in Gas Metal Arc Welding (GMAW) of the 0.5" thick plate. The base metal AL6XN in plates P_B and P_C is also an austenitic alloy of composition as shown in Table 2.2. A filler material of type INCONEL-625 manufactured by Inco Alloys International was used during the welding of the 0.5" thick plate. The composition of the filler material INCONEL-625 is shown in Table 2.3.

Element	Weight Percentage
Carbon	0.039
Manganese	4.950
Phosphorus	0.023
Sulphur	0.005
Silicon	0.46
Chromium	21.11
Nickel	12.19
Molybdenum	2.14
Nitrogen	0.263
Vanadium	0.16
Cobalt	0.15
Iron	58.51

Table 2.1: Compositional analysis of base NITRONIC-50 stainless steel.

NITRONIC-50 and AL6XN are nitrogen-strengthened austenitic stainless steels developed for applications where strength and corrosion resistance are of primary importance. In these alloys, the addition of nitrogen has proven to be the most effective alloying element for increasing the flow stress (Reed 1988). Solid solution hardening is the dominant mechanism of strengthening in these austenitic alloys. The main differences between the compositions of the two stainless alloys appear to be in the additional Nickel and Molybdenum in AL6XN and the higher amount of Nitrogen in NITRONIC-50. The additional Nickel and Molybdenum contribute to the excellent corrosion resistance properties of AL6XN compared to that of other 300 series alloy steels. The additional nitrogen is expected to lead to a higher flow stress for NITRONIC-50 than for AL6XN.

The microstructure of AL6XN, as observed in an optical microscope after standard polishing and etching, is shown in Figures 2.3. The etching agent used in this case is aqua regia (15ml of hydrochloric acid and 5ml of Nitric acid) with 2ml of hydrofluoric acid. Due to the extremely low percentage of sulphur ($< 0.002\%$), the manganese

Element	Weight Percentage
Carbon	0.024
Manganese	0.41
Phosphorus	0.021
Sulphur	0.002
Silicon	0.36
Chromium	20.56
Nickel	23.84
Molybdenum	6.21
Nitrogen	0.213
Copper	0.20
Cobalt	0.20
Iron	47.86

Table 2.2: Compositional analysis of base AL6XN stainless steel.

Element	Weight Percentage
Nickel	61.0
Chromium	21.5
Molybdenum	9.0
Niobium	3.6
Iron	2.5
Carbon	Unknown

Table 2.3: Compositional analysis of weld Inconel-625 superalloy.

sulphide (MnS) inclusions are fewer in number than in such ferritic alloys as HY-100. The rolled and annealed microstructure of the plate also contains several twin boundaries. The average grain size in this microstructure is approximately $40\mu m$. Enlarged grains which were more than $100\mu m$ in size were found adjacent to the weld in the HAZ.

INCONEL-625 is a Nickel-Chromium-Molybdenum based alloy developed for applications in high temperature and corrosive environments. As such, welding of AL6XN stainless steel with the more highly alloyed INCONEL-625 as the filler material is an excellent choice for application in corrosive marine environments. The

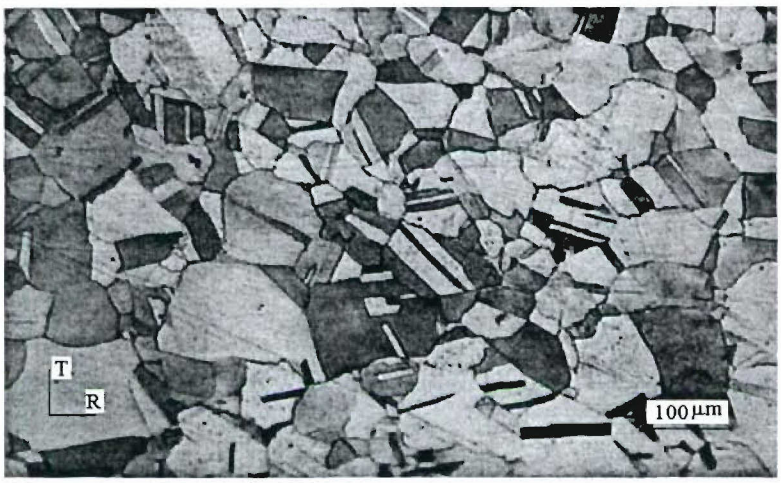

Figure 2.3: Optical micrograph of the base AL6XN stainless steel.

dendritic microstructure of INCONEL-625 adjacent to the weld is as shown in Figure 2.4. The etching agent used was: 30ml distilled water, 10ml nitric acid, 20ml hydrochloric acid with 10ml of hydrogen peroxide.

2.2 High Strain Rate Compression Experiments in a Kolsky Bar

The high strain rate plastic flow behavior of specimens machined from the base metal, weld, and heat-affected zones of NITRONIC-50 and AL6XN welded plates was investigated in compression in a Kolsky bar apparatus. A schematic of the Kolsky bar set-up for compression experiments is shown in Figure 2.5. The operation and construction of this Kolsky bar at Brown University has been described by Wagoner (2001). The test specimen is sandwiched between two long and high strength 4340 steel bars (termed the incident and transmitter bars) and is loaded in compression by the impact of a projectile at one end of the incident bar. A gas gun assembly is used to accelerate the projectile (also 4340 steel) and produce a compressive loading pulse in the incident bar upon impact. The projectile, incident and transmitter bars have

Figure 2.4: Optical micrograph of the weld Inconel-625 superalloy.

nominally the same diameter, which is 1" for the experiments reported here. The magnitude and duration of the loading pulse in the incident bar is determined by the velocity of the projectile at impact and by the length of the projectile.

Upon arrival of the compressive pulse at the incident bar/specimen interface, a portion of it is transmitted through the specimen to the transmitter bar and the remainder is reflected back into the incident bar. The magnitude of the loading pulse and the specimen dimensions are designed so as to induce the desired plastic deformation in the test sample while the incident and transmitter bars remain fully elastic over the duration of the experiment. Strain gage stations are located on the incident and transmitter bars to monitor the incident compressive pulse, the reflected tensile pulse and the transmitted compressive pulse. A momentum bar is used to trap the transmitted compressive pulse and prevent any further reloading of the test sample after passage of the initial loading pulse. A schematic of the time-distance diagram showing the location of the wavefronts in the Kolsky bar compression test is shown in Figure 2.6.

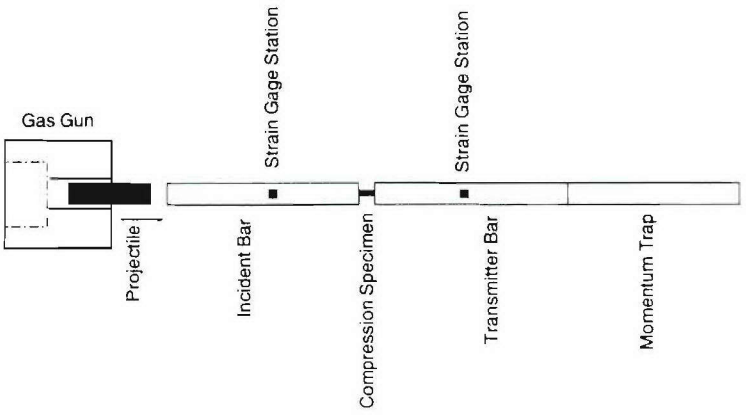

Figure 2.5: Layout of the Kolsky bar compression test configuration.

The strain gage stations on the incident and transmitter bars are located so as to obtain a complete record of the incident, reflected and transmitted signals without any overlap. Figure 2.7 shows a record of a typical strain pulse obtained at the gage stations on the incident and transmitter bars. This experiment was carried out using a 20" projectile; the corresponding duration of the loading pulse is approximately $200\mu sec$. The Kolsky bar compression test specimen is designed to undergo homogeneous plastic deformation. Its length is 4mm and its diameter is 8mm. The specimen/bar interfaces are well lubricated to minimize frictional constraints at the ends of the specimen. The dynamic stress-strain response of specimens obtained under these conditions can be viewed as a material response obtained under homogeneous deformation.

The analysis of the Kolsky bar compression experiment involves an understanding of the plastic flow behavior of the sandwiched test specimen from the elastic wave propagation record at the strain gage stations. Let $\epsilon^I(t)$, $\epsilon^R(t)$ and $\epsilon^T(t)$ represent the trace of the recorded incident, reflected and transmitted signals at the gage stations. Since the strain pulse is recorded far away from the specimen/bar interface, we account for its dispersion as it travels along the length of the incident and transmitter

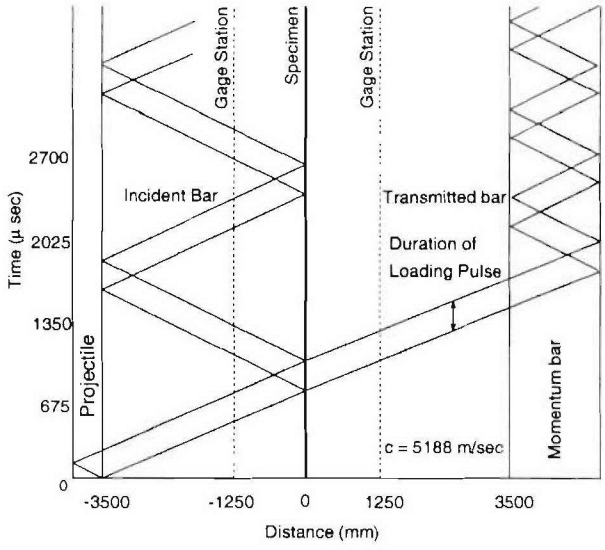

Figure 2.6: Time-distance diagram for Kolsky bar tests in compression.

bars. Appendix A describes the propagation of the measured elastic wave from the strain gage stations to the specimen/bar interfaces based on the Pochhammer-Chree dispersion relation (Pochhammer (1876), Chree (1889)). The dispersion correction to the measured strain-time pulse and a knowledge of the longitudinal wave speed in the incident/transmitter bars allows for an accurate inference of the boundary conditions experienced by the plastically deforming test specimen. Let $[\epsilon^I(t)]^{INT}$, $[\epsilon^R(t)]^{INT}$ and $[\epsilon^T(t)]^{INT}$ represent the synchronized time history of the reconstructed strain pulse at the specimen/bar interfaces. Assuming homogeneous deformation, the strain rate experienced by the specimen is given by

$$\dot{\epsilon_s} = \frac{c_0}{t_s}(-[\epsilon^I(t)]^{INT} + [\epsilon^R(t)]^{INT} + [\epsilon^T(t)]^{INT}). \tag{2.1}$$

The stress transmitted through the specimen is given by

$$\sigma_s(t) = \frac{A_b E_b}{A_s}[\epsilon^T(t)]^{INT}. \tag{2.2}$$

Here, $\dot{\epsilon}_s(t)$ and $\sigma_s(t)$ are the strain rate and stress in the specimen, c_0 is the longitudinal wave speed in the 4340 steel bar, A_s and t_s are the cross-sectional area and

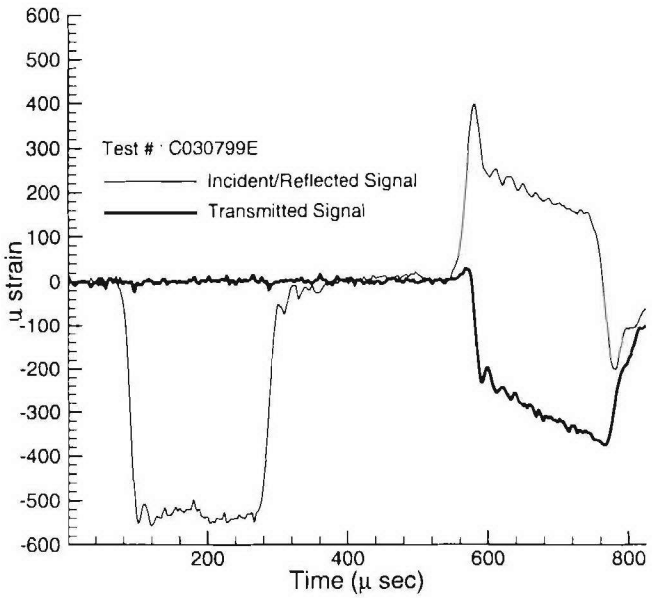

Figure 2.7: Record of strain pulse measured at the gage stations in a compression Kolsky bar configuration.

thickness of the compression test specimen, A_b is the cross-sectional area of the incident/transmitter bar and E_b is its Young's Modulus. The accumulated plastic strain in the specimen is obtained by integrating the strain-rate history over the duration of the loading pulse.

A series of high strain rate ($\approx 500/sec$) compression Kolsky bar experiments was conducted on test specimens machined from the base metal, weld and heat affected zones. Test specimens prepared from the NITRONIC-50 welded plate were dynamically loaded in the Kolsky bar by a 20" projectile. Test results from the AL6XN welded plate were obtained by loading specimens with either a 20" or a 40" projectile to obtain data at larger plastic strains under similar strain rates. The orientation of the compression specimen from the base and HAZ was varied to be either along the rolling direction or along the weld direction. The orientation of the weld specimen was such that the loading was transverse to the weld direction. The stress-strain records

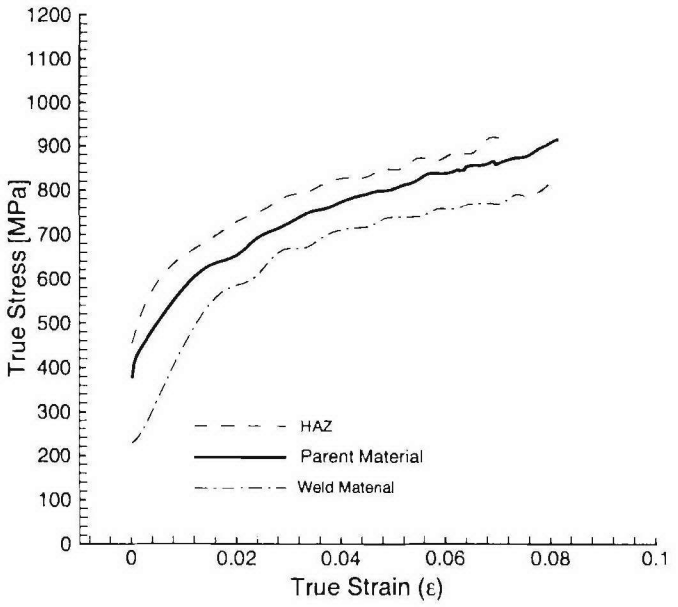

Figure 2.8: Summary of high strain rate compression experiments on Nitronic-50 stainless steel welded plate.

shown below were obtained after correcting for dispersion of the measured strain pulse and represent averaged results obtained from testing at least 3-4 specimens in each orientation.

A summary of the results obtained from high strain rate compression experiments on the NITRONIC-50 stainless steel welded plate is shown in Figure 2.8. Similarly, Figure 2.9 shows a summary of similar results obtained from testing on AL6XN stainless steel welded plates. The strain hardening of the base stainless alloy for either loading direction was found to be similar. The response of HAZ specimens loaded along the weld direction was found to be similar to the response of the base material. However, the response of the HAZ specimens loaded in a direction across the weld had a slightly higher flow stress compared to that of the base metal. In both plates, the flow stress of the weld specimens was clearly less than that of the base metal; that is, the welds are 'undermatched' relative to the plates being joined.

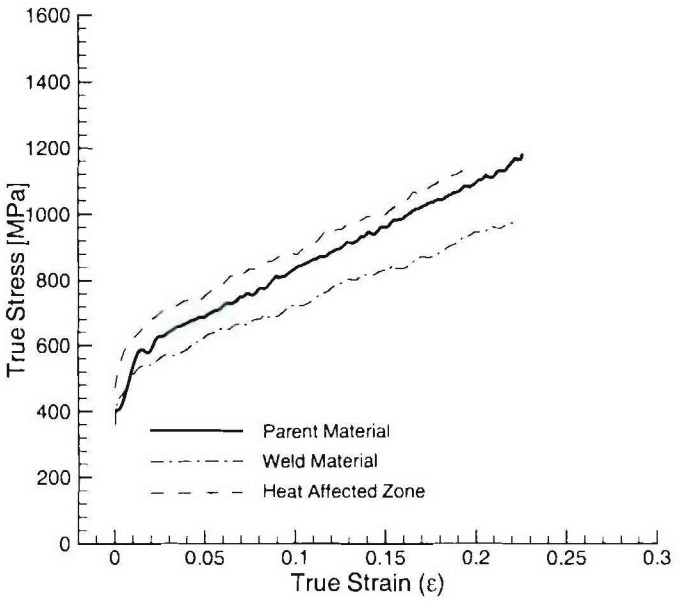

Figure 2.9: Summary of high strain rate compression experiments on AL6XN welded plate.

2.3 High Strain Rate Tension Experiments in a Kolsky Bar

The high-strain-rate plastic flow and fracture behavior of stainless steel welds and the surrounding heat-affected zone was also investigated under dynamic tensile loading conditions. A schematic of the Kolsky bar apparatus used to obtain high-strain-rate tensile loading of the specimen is shown in Figure 2.10. As in the compression Kolsky bar, the test specimen is sandwiched between the incident and transmitter bars which remain elastic during the duration of the experiment. The strain pulse at the incident and transmitter bar strain gage stations are used to examine the plastic behavior of the test specimen under tensile loading conditions. The basic differences between Kolsky bar configurations in tension and compression relate to (a) generation of the tensile loading pulse, (b) design of the high strain rate tensile specimen, (c) method

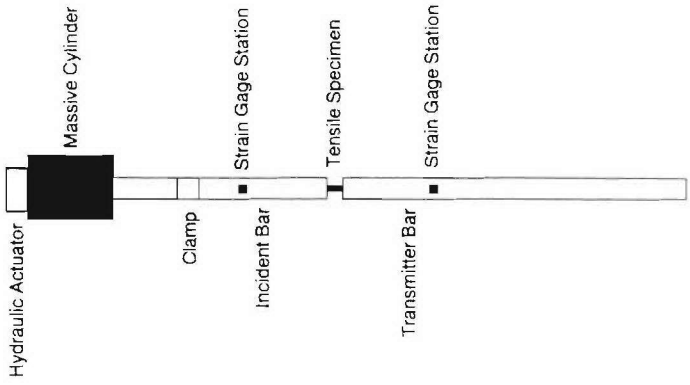

Figure 2.10: Layout of the Kolsky bar tension test configuration.

of attachment of the specimen to the incident/transmitter bars and (d) interpretation of test results.

We generate a tensile loading pulse by the sudden release of stored strain energy in a portion of the incident bar. The incident bar is initially clamped at the location shown in Figure 2.10. Details of the clamp assembly (Hartley, Duffy and Hawley (1985)) are shown in Figure 2.11. The arms of the clamp have steel pads shaped to match the circumference of the Kolsky Bar. The arms of the clamp are held together at the top by a notched 6061 aluminum breaker bar. Under the action of an hydraulic actuator, the clamp is tightened on the Kolsky bar by forcing the lower ends of the arms of the clamp together. The tightening of the clamp also loads the notched breaker bar in tension. After initial tightening of the clamp, the portion of the incident bar between the clamp and the massive cylinder is loaded in tension by an another hydraulic actuator assembly. Further tightening of the clamp results in a brittle fracture of the notched breaker bar and the propagation of a tensile loading pulse toward the specimen. A schematic of the time-distance diagram for the Kolsky bar tension test is shown in Figure 2.12. The magnitude of the loading pulse is determined by the strain energy density in the incident bar prior to release of the

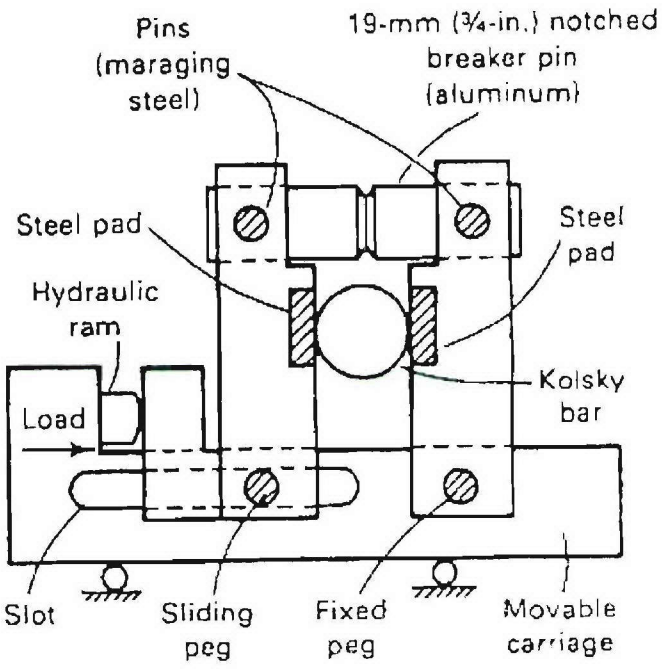

Figure 2.11: Design of the clamp assembly in the tension Kolsky bar.

clamp. The duration of the loading pulse is determined by the distance between the clamp assembly and the massive cylinder.

The transmission of the tensile loading pulse to the test specimen is achieved through the specimen gripper assembly. The grippers (also made of 6061 aluminum) have threaded ends which are attached to the incident and transmitter bars. The test specimen is held between the arms of the gripper by two pins which transmit the tensile loading pulse from the incident bar. The gripper assembly also ensures that the test specimen is loaded in tension only over the duration of the initial tensile incident pulse *i.e.* any subsequent reflections from the ends of the bar do not load the specimen again. This ensures that the observed microstructure of the deformed specimen is the microstructure resulting from the passage of the first tensile loading pulse.

A design for a tensile test specimen to study the plastic flow behavior in tension in Kolsky bar tests is shown in Figure 2.13. Unlike a compression test specimen, only

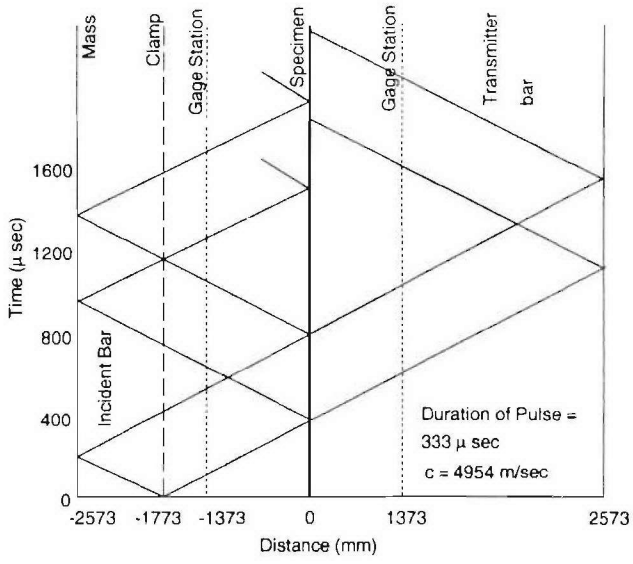

Figure 2.12: Time-distance diagram for Kolsky bar tests in tension.

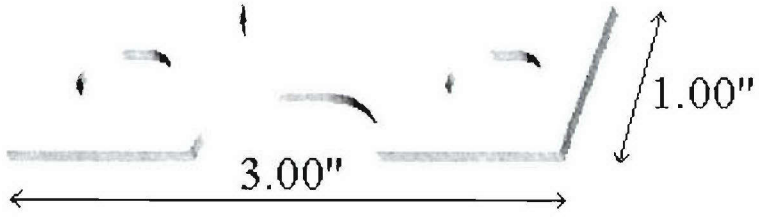

Figure 2.13: Design of a high strain rate flat tensile test specimen.

a central gage section of the test specimen undergoes plastic deformation. For short specimen lengths, the elastic constraint imposed by the material outside of the gage section results in a non-uniform state of plastic deformation inside the gage section. To avoid the concomitant decrease in the applied strain rates that would result if the specimen length were increased, the specimen design allows the plastic deformation in the gage section to be somewhat inhomogeneous. Therefore, the measured strain-time records at the gage stations cannot be processed directly to yield the flow behavior in simple tension.

Our initial investigation focused on the high strain rate response of flat tensile

test specimens machined from the various material zones of stainless steel welded plates P_A and P_B. A total of 20 experiments were conducted on each of the two stainless steel alloys. Test specimens were machined from the NITRONIC-50 and AL6XN welded plates such that the specimen gage section was located in either the base, weld or heat-affected zone. The orientation of the specimen was varied to be either along the rolling direction or along the weld direction. A rich variety of behavior was observed under dynamic tensile loading. Figure 2.14 shows a record of the strain pulses measured at the incident and transmitter bar gage stations for a flat, tensile specimen machined from the base material of AL6XN plate P_B. A finite element simulation of the Kolsky bar tension test revealed the presence of an evolving plastic zone in the specimen gage section. However, the strain hardening of the tensile base material specimen was found to be nevertheless consistent with that observed in compression.

Under nominally identical loading conditions, specimens from the base material zone of NITRONIC-50 plate P_A showed no evidence of failure when loaded along either the weld direction or across it. In contrast, a number of premature failures were observed when test specimens from the HAZ were loaded across the weld direction. An examination of the transmitted strain signal showed that ductile fracture appeared to initiate in most instances even before the onset of plastic deformation over the entire gage length of the tensile specimen. SEM observations of the fracture surface revealed the presence of elongated voids at the HAZ/weld interface. Figure 2.15 shows a fractograph of the ductile fracture surface obtained from a NITRONIC-50 specimen machined from the HAZ. An examination of the cross-section of the welded plate under an optical microscope also revealed the presence of an extensive void sheet at the interface of the HAZ/weld zone. It appears that plate P_A was a particularly poor example of a stainless steel weld due to extensive accumulation of porosity near

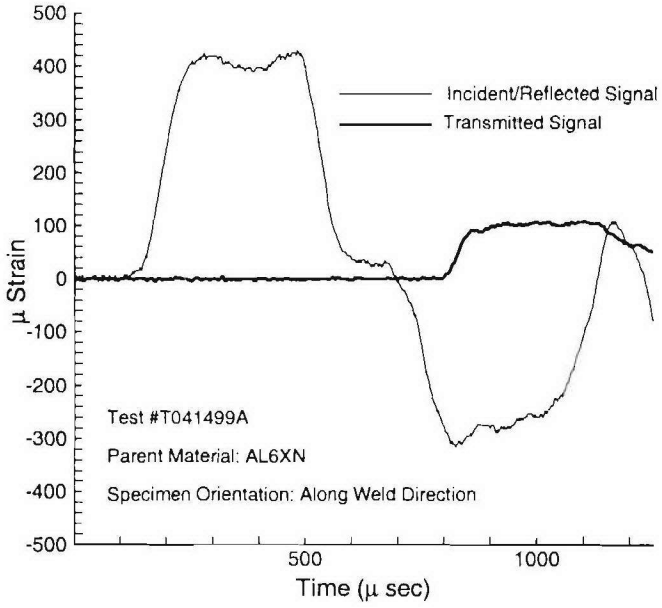

Figure 2.14: Record of strain pulse measured at the gage stations in a tension Kolsky bar configuration. Specimen was machined from the base material of the AL6XN stainless steel welded plate P_B.

the HAZ/weld interface.

A similar set of 20 experiments were carried out on flat tensile specimens machined from the base(4), weld(8) and heat-affected zone(8) of AL6XN stainless steel plate P_B. Under nominally identical loading conditions, specimens machined from the HAZ/weld zones showed a preferential loss of ductility compared to those machined from the base material. Two of the 8 weld specimens tested, fractured even before stress levels were high enough to initiate plastic deformation at the gage section of the specimen. However, an examination of the cross-section of the AL6XN stainless steel welded plate at various locations showed an intact HAZ/Weld interface with no visible accumulation of porosity (unlike the observations for plate P_A).

A more detailed investigation of the fracture behavior of AL6XN stainless steel welded plates was carried out on notched test specimens machined from plate P_C.

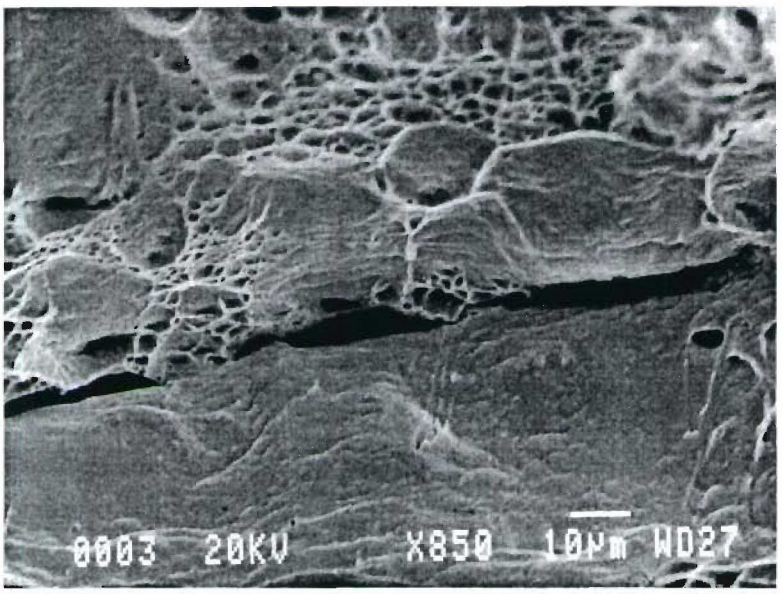

Figure 2.15: Presence of large interface voids in weld/HAZ tensile specimens machined from the NITRONIC-50 stainless steel welded plate P_A

The design for a high strain rate notched tensile test specimen used in our Kolsky bar fracture experiments is shown in Figure 2.16. The specimen has a uniform thickness of 0.09" and contains a 0.0625" diameter notch at the center with a depth of 0.03125". The axis of the notch is along the weld and the specimen gage section is loaded along the rolling direction. A total of 16 experiments were conducted on nominally identical test specimens where the notch was located within the weld zone(6), the base material(4) or in the HAZ(6) adjacent to the weld. The magnitude of the loading pulse was sufficient to initiate complete fracture of the test specimen in all instances. The results of these tests provide a direct comparison of the fracture toughness and ductility of the various material zones in the heterogeneous welded stainless steel plate. An additional set of experiments was conducted on 8 test specimens with a different specimen thickness and notch profile. The results from these experiments are used in Chapter 4 to verify a finite element model of ductile fracture in stainless steel weldments.

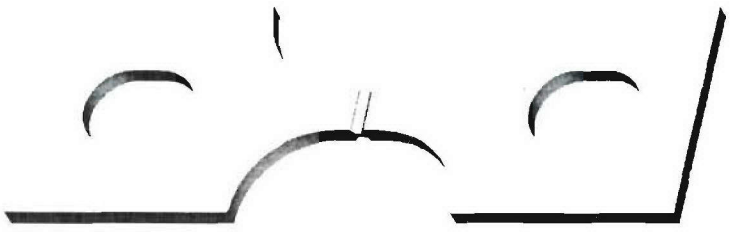

Figure 2.16: Design of a high strain rate notched tensile test specimen.

Figure 2.17 shows a typical response from a notched tensile specimen machined from the base AL6XN stainless steel alloy. Similarly, Figure 2.20 shows a typical response from an identical specimen machined from the weld INCONEL-625 superalloy. The fall in the transmitted stress, indicated by the fall in the transmitted strain pulse, signifies the complete fracture and loss of stress-carrying capacity in the specimen. Simultaneously, the reflected signal shows a sudden rise in the compressive stress until it reaches a level equal to the magnitude of the incident tensile pulse. The shape of the reflected pulse prior to fracture arises from the combined effects of (a) the shape of the incident pulse, (b) wave reflections from the specimen-gripper assembly and (c) the plastic flow response of the test specimen. A comparison of the response of the base and weld tensile specimens under nominally identical test conditions reveals that the flow stress of the weld material is slightly undermatched when compared to the base material. This observation is consistent with the observed plastic flow behavior of the base and weld specimens when loaded in compression in the Kolsky bar configuration. In addition, from the duration of the transmitted pulses, it is evident that the overall ductility of the weld is much less than that of the base material. The reduced ductility of the weld alloy was also confirmed by quasistatic tests in an Instron testing machine on notched axisymmetric tensile test specimens machined from the base and weld material zones.

Figures 2.18 and 2.19 show a micrograph of the base AL6XN stainless steel fracture

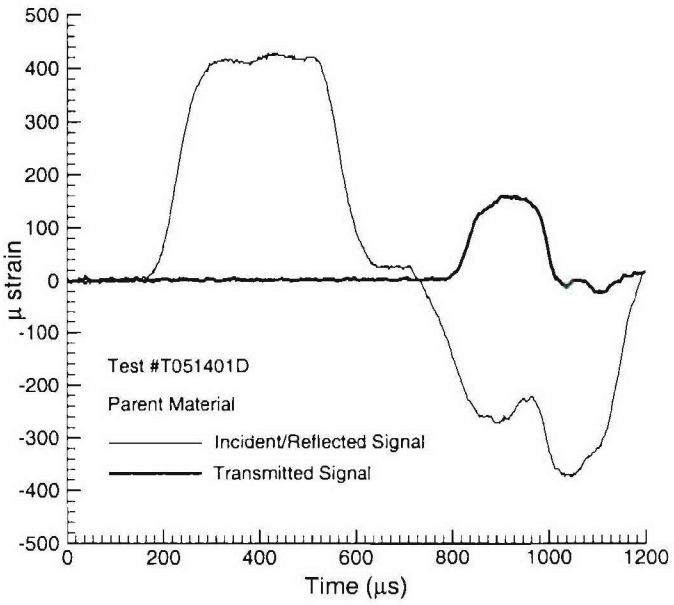

Figure 2.17: Record of strain pulse measured at the gage stations in a tension Kolsky bar configuration. Specimen was machined from the base material of the AL6XN stainless steel welded plate P_C. Loading is along the rolling direction.

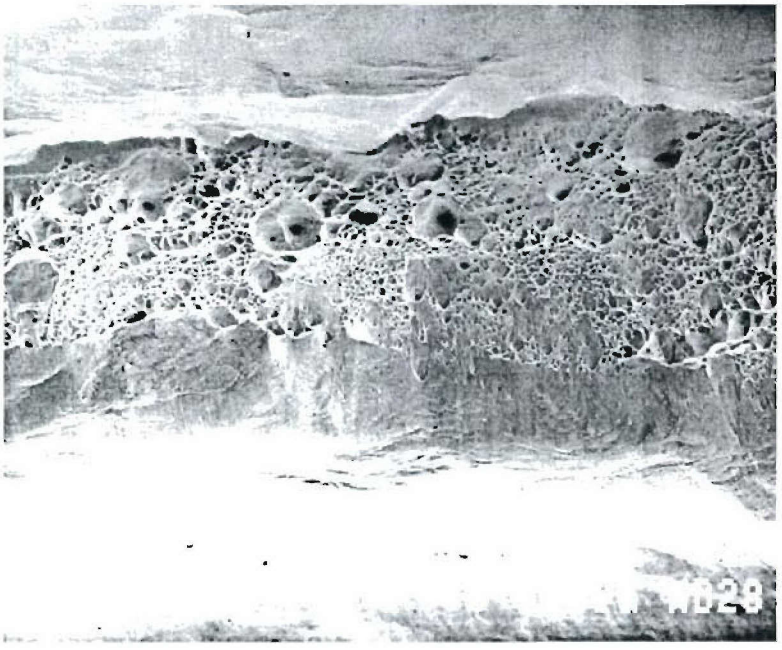

Figure 2.18: SEM micrograph of the ductile fracture surface of AL6XN stainless steel.

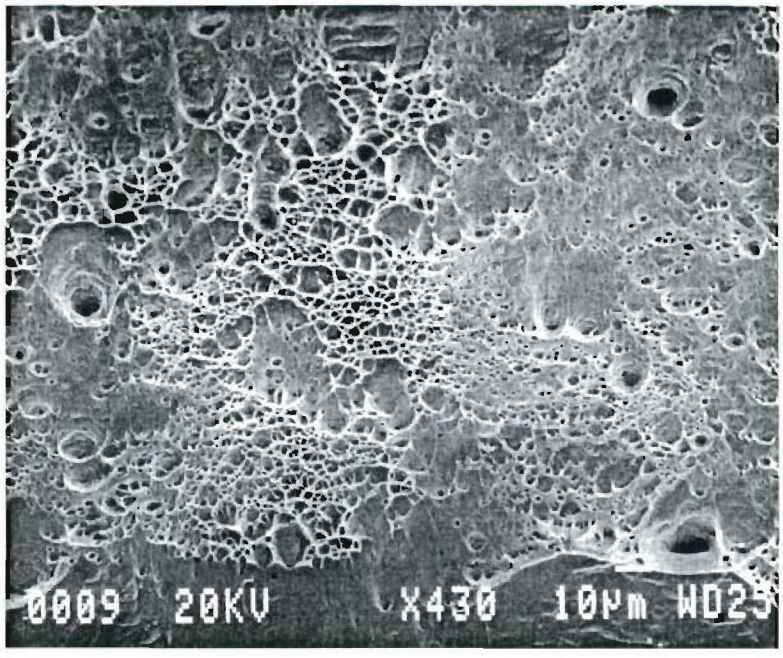

Figure 2.19: SEM micrograph of the ductile fracture surface of AL6XN stainless steel.

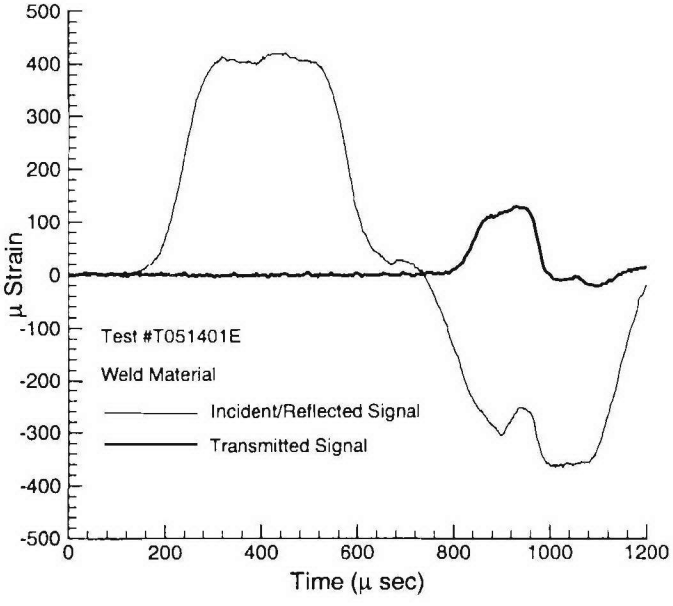

Figure 2.20: Record of strain pulse measured at the gage stations in a tension Kolsky bar configuration. Specimen was machined from the weld material of the AL6XN stainless steel welded plate P_C. Loading is along the rolling direction.

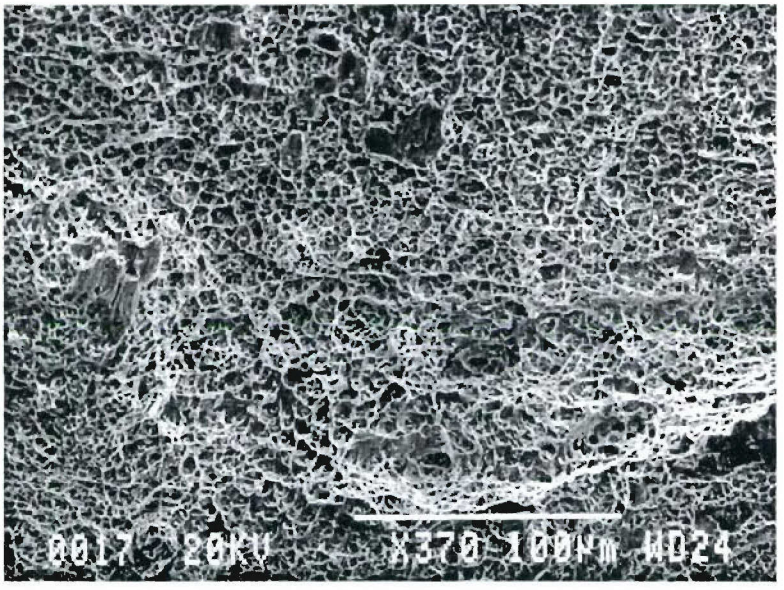

Figure 2.21: SEM micrograph of the ductile fracture surface of weld INCONEL-625 Superalloy.

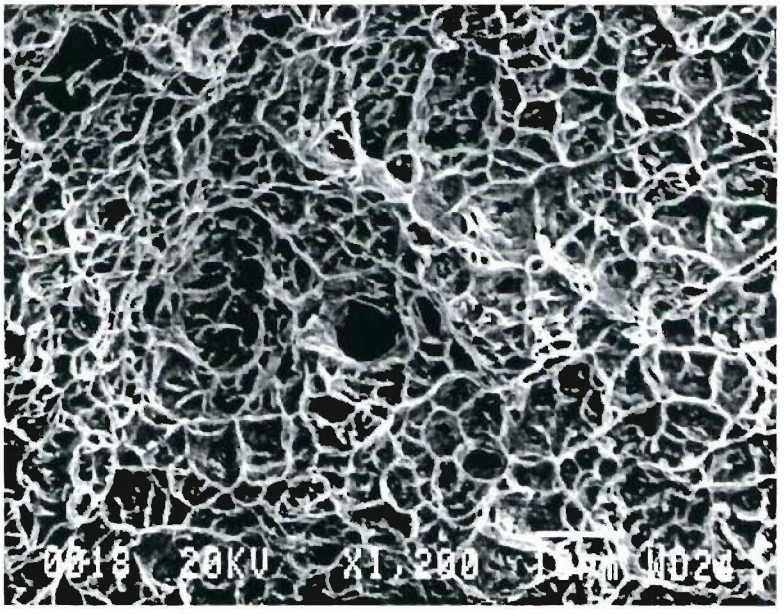

Figure 2.22: Fine-scale void sheet on the ductile fracture surface of weld INCONEL-625 superalloy.

surface obtained in a scanning electron microscope. Similarly, Figures 2.21 and 2.22 show a micrograph of the weld INCONEL-625 fracture surface. Both alloys show a predominantly ductile mode of fracture interspersed with small zones of quasi-cleavage. The high-strength AL6XN stainless alloy clearly shows the presence of a dual-sized population of voids. A population of small-scale voids interlink the ligaments between the larger voids across the fracture surface. In Figure 2.18, the fracture can be seen to initiate in a narrow strip of material at the top of the specimen. After initiation at the voided strip, the fracture surface is observed to propagate through the rest of the specimen cross section by a predominantly quasi-cleavage mode due to the extremely high strain rates of loading. In the weld INCONEL-625 alloy, an extremely fine void sheet is found across most of the fracture surface. The fine scale void sheet is interrupted only by small regions showing a quasi-cleavage mode of separation or by a few voids which have grown much larger than their neighbors.

Unlike the dynamic tensile response of specimens machined entirely from the base or weld material zones, the response of specimens machined from regions adjacent to the weld can be grouped into two distinct regimes (say, HAZ1 and HAZ2). In all instances, the ductility of HAZ tensile specimens was clearly lower than base material or weld specimens tested under nominally identical conditions. However, out of the total of 6 HAZ specimens tested, 4 (Type: HAZ1) had a fairly repeatable fracture response, whereas the remaining two (Type: HAZ2) showed a dramatically lower ductility. Figure 2.23 shows the strain-time record from a high strain rate tension test conducted in a Kolsky bar on a Type HAZ1 specimen (repeatable) while Figure 2.24 shows a similar record for a Type HAZ2 specimen. The location of the notch in both of these experiments was such that the eventual fracture surface was within the weld zone. The large scatter in the HAZ tensile specimen response indicates that the strength of the weld/HAZ interface, and, damage evolution adjacent to it, vary along

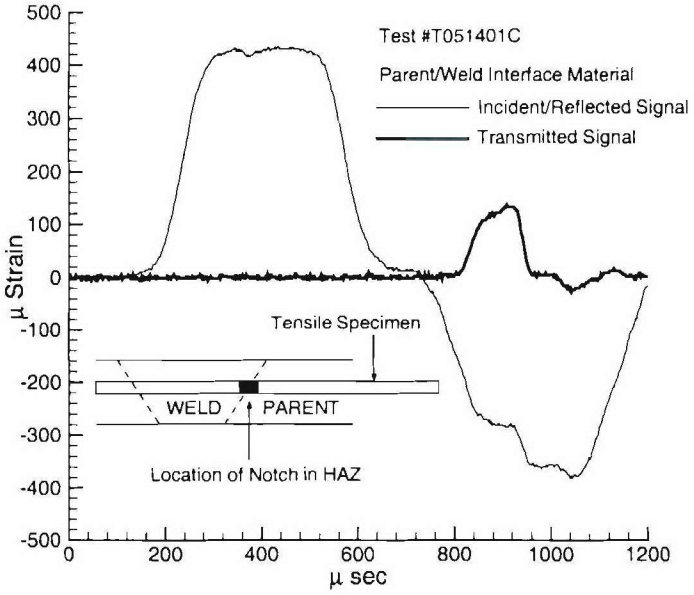

Figure 2.23: Record of strain pulse measured at the gage stations in a tension Kolsky bar configuration. Specimen was machined from the HAZ of the AL6XN stainless steel welded plate P_C. Loading is along the rolling direction.

the length of the welded plate.

2.4 Analysis of the Weld/HAZ Interface Micro structure using XEDS

The results of the previous section suggest that the properties of the HAZ play a significant role in determining the overall flow and fracture behavior of stainless steel weldments. The high strain rate flow and fracture properties of the HAZ have been characterized in sections §2.2 and §2.3. In this section, we attempt to elucidate the role played by compositional fluctuations near the base/weld interface in influencing the mechanical behavior of the HAZ. To obtain an understanding of the compositional fluctuations, EDS (Energy Dispersive Spectroscopy) spectra were obtained in

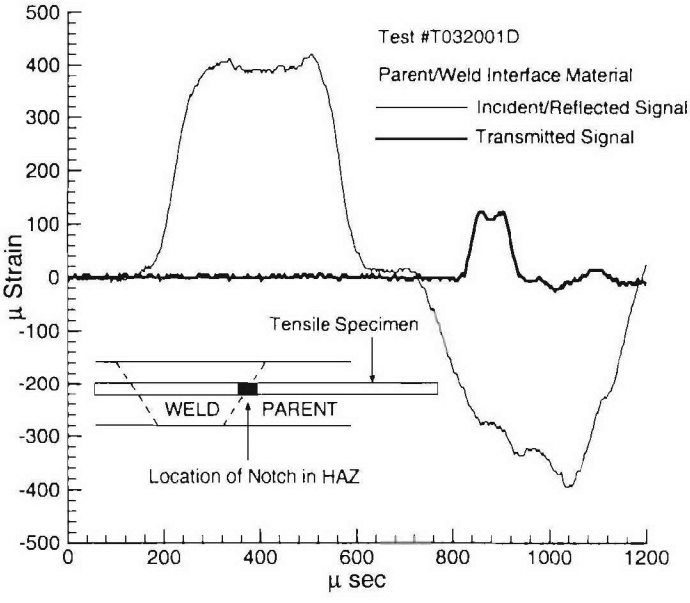

Figure 2.24: Record of Strain Pulse Measured at the Gage Stations in a Tension Kolsky bar configuration. Specimen was machined from the HAZ of the AL6XN stainless steel welded plate P_C. Loading is along the rolling direction.

a JEOL 845 Scanning Electron Microscope at various locations along a line across the base/weld interface in plate P_C. Figure 2.25 shows an optical micrograph of the base/weld interface etched to bring out the microstructure of the base stainless alloy. The orientation of the line along which XEDS spectra were obtained is shown in Figure 2.25. At locations away from the interface, data were obtained at $250\mu m$ intervals. Near the interface, XEDS spectra were obtained at $25\mu m$ intervals.

In our analysis of the XEDS spectra, we were concerned with 4 major components which are common to both the base and weld alloys: Fe, Ni, Cr and Mo. Over the X-ray energy range of 0-10 keV, peaks corresponding to Fe K_α, Ni K_α, Cr K_α and Mo $L_{\alpha 1}$ were identified. Data obtained at 27 different locations were processed using DTSA[1] software to obtain the total number of counts corresponding to each

[1]Desktop Spectrum Analyzer (DTSA): A Macintosh based X-ray spectral analysis and manipulation software developed at the National Institute of Standards and Technology (NIST) in

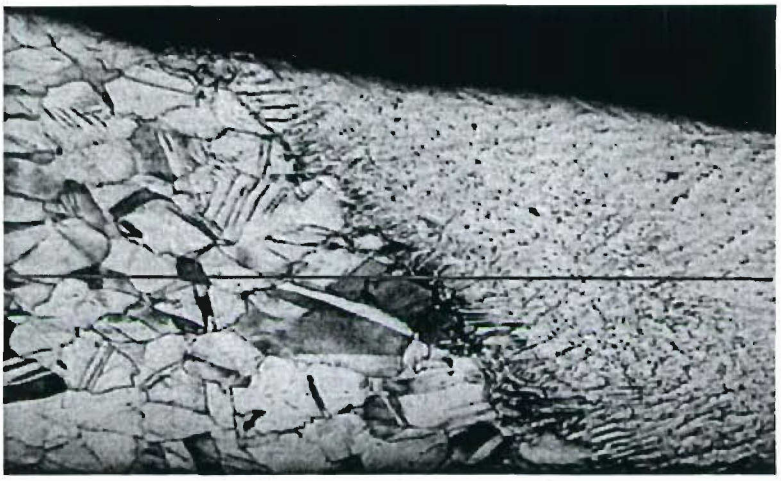

Figure 2.25: Base Material/Weld interface region in AL6XN stainless steel welded plate P_C.

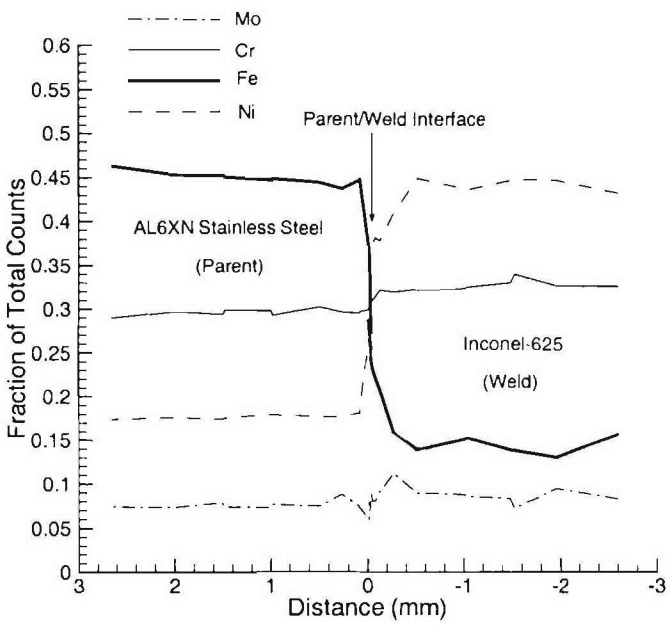

Figure 2.26: Composition of the AL6XN/Inconel-625 alloy interface obtained using X-ray EDS.

element. Figure 2.26 shows the variation of the fractional counts corresponding to each component at various distances from the base/weld interface. Spectra obtained from the base material near the interface indicate that the local composition reaches the equilibrium far-field values at distances less than $75\mu m$. In contrast, the local composition of the weld material differs significantly from its equilibrium values at distances up to $250\mu m$ from the interface. Therefore it can be expected that the properties of the weld will be affected at a much greater distance from the interface than will be the those of the base material.

During the thermomechanical processing of the mismatched base/weld alloy at high temperatures, migration of elemental carbon across the interface from the weld to the base material side of the interface is expected to be the significant factor in modifying the flow and fracture properties of the HAZ. However, an investigation of the carbon concentration across the interface would involve a detailed electron probe microanalysis (EPMA) in a transmission electron microscope. The increased flow strength and reduced ductility of specimens machined from the HAZ points to the presence of a carbon enriched zone in the stainless alloy and a corresponding carbon-depleted zone in the weld zone adjacent to the HAZ. The interplay between the undermatched weld zone and the overmatched heat-affected zone on the overall ductility of stainless steel weldments is studied using detailed three-dimensional finite element simulations in Chapter 4.

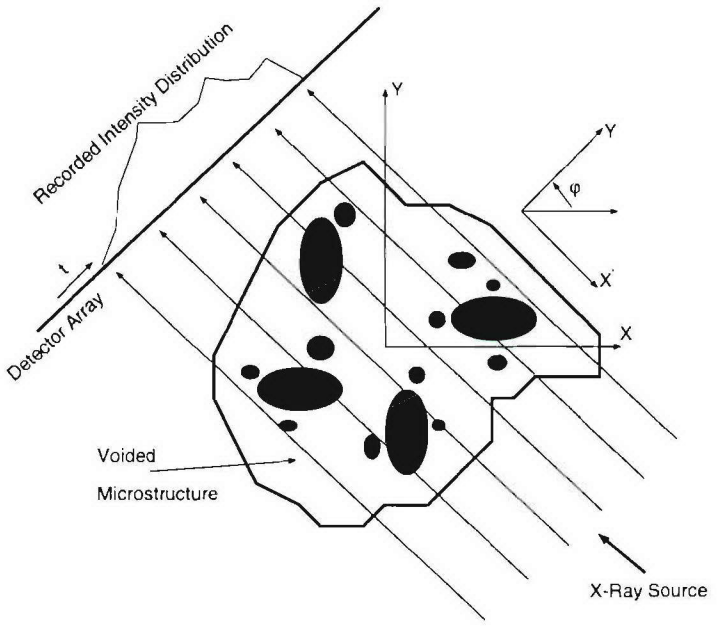

Figure 2.27: Tomographic imaging of a voided test specimen.

2.5 X-ray Computed Microtomography of AL6XN - IN625 Tensile Specimens

As described in §2.3, the dominant mechanism of failure in AL6XN stainless steel weldments under dynamic loading conditions is that of ductile fracture. The mechanism of ductile fracture in these high strength alloys can be characterized by the presence of three successive stages of damage evolution: (1) Microvoid nucleation at the location of second-phase inclusion sites either by particle cracking or by debonding of the particle/matrix interphase; (2) Void growth under the influence of the applied stress and of the deformation of the surrounding incompressible matrix material; and (3) Coalescence of neighboring voids and the resulting failure of the inter-void ligament. Analytical and computational models of ductile fracture have been developed

Gaithesburg, MD and the National Institutes of Health (NIH) in Bethesda, MD.

over the last three decades by various researchers. However, experimental characterization of the voided microstructure and its dependence on with the applied stress state and the deformation history have been rare. Pardoen and Delannay (1998) have investigated the validity of various void growth models for predicting the ductile response of industrial, cold-drawn copper. They identified model parameters in Gurson-type constitutive models for void growth from measurements of density measurements on samples cut from the necking zone of cylindrical tensile specimens. Density measurements were obtained using the Archimedean method in xylene on test samples that were 3.2-4.7 mm in height and approximately 4 mm in diameter. In this study, we will develop a scheme to characterize the damage in plastically deformed tensile specimens at a resolution significantly higher than in Pardoen and Delannay (1998). We will use X-ray Computed Microtomography (XCMT) to obtain preliminary insights into voided, fracture-process zones in AL6XN stainless steel weldments. These experiments were carried out at the National Synchrotron Light Source (NSLS), Brookhaven National Laboratory in collaboration with the Naval Research Laboratory[2].

X-ray tomography offers a convenient tool to obtain a three-dimensional compositional map of the partially voided specimen. Investigation of voided microstructures using tomography are particularly attractive because of the non-destructive nature of imaging (at least for metallic alloys). The objective of X-ray tomography is to obtain a volumetric image of linear X-ray attenuation coefficients in the specimen by measuring X-ray absorption data along various orientations. X-ray attenuation coefficients are known to be sensitive to variations in elemental composition and density (Kinney and Nichols (1992)). Therefore, a three-dimensional image of the voided

[2]XCMT experiments were done in collaboration with Richard Everett, Andrew Geltmacher and Kirth Simmonds, Code 6352, Multifunctional Materials Branch, Naval Research Laboratory, Washington, DC

microstructure can be recreated from a map of X-ray attenuation coefficients over the specimen. A schematic illustrating the principle of X-ray tomographic microscopy is shown in Figure 2.27.

The attenuation of a monochromatic X-ray beam due to passage in a homogeneous medium is given by

$$I_T = I_0 \exp(-\mu_0 L). \tag{2.3}$$

Here, I_T and I_0 are the transmitted and incident X-ray intensities, L is the length traversed by the X-ray beam and μ_0 is the attenuation coefficient of the homogeneous medium. Similarly, the attenuation of a monochromatic beam in a heterogeneous medium is given by a line integral as

$$-\ln\left[\frac{I_T}{I_0}\right] = \int_0^L \mu(s)ds \tag{2.4}$$

where $\mu(s)$ describes the variation of the attenuation coefficient across the path of the beam. To consider the determination of the attenuation coefficients throughout a slice of the material, define a new coordinate system (t, ϕ) for the detector array as shown in Figure 2.27. The projection of the sample is defined by the Radon transform (Radon 1917) of the attenuation coefficient distribution $\mu(x, y)$ as

$$P(t,\phi) = -\ln\left[\frac{I_T(t,\phi)}{I_0}\right] = \int_{-\infty}^{\infty}\int_{-\infty}^{\infty} \mu(x,y)\delta(x\cos(\phi) + y\sin(\phi) - t)dxdy \tag{2.5}$$

where $\delta(x\cos(\phi) + y\sin(\phi) - t)$ is the Dirac delta function which identifies the path of the X-ray beam reaching the detector array at location t. The mathematics of image reconstruction then reduces to solving for the distribution $\mu(x, y)$ from a finite set of measurements of the transmitted X-ray intensities at various orientations of the specimen. In our calculations, we use a Fast Filtered Back Transform (FFBT) technique (Herman 1980) to compute $\mu(x, y)$ from the recorded set of projections.

Experiments on test specimens prepared from AL6XN stainless steel weldments were conducted on beamline X27A at the National Synchrotron Light Source, Brookhaven

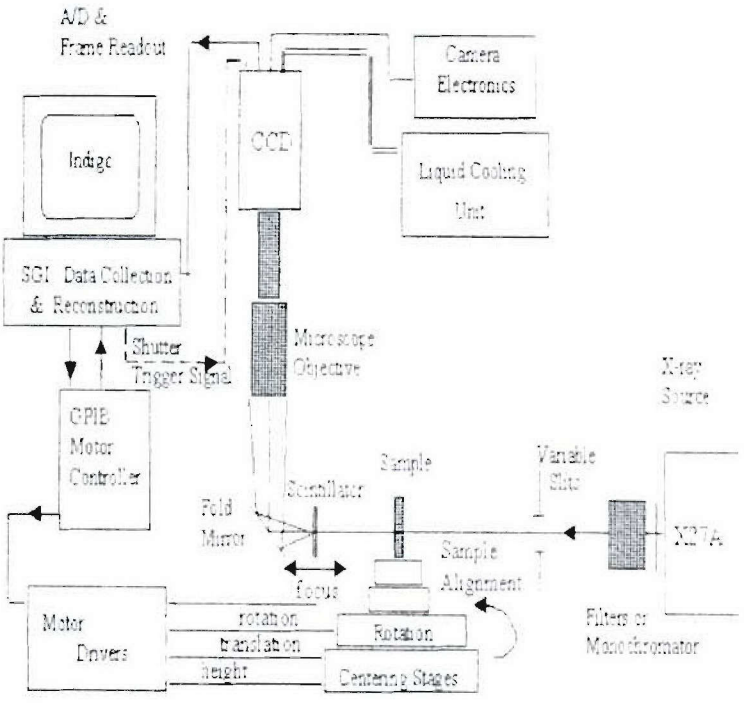

Figure 2.28: Schematic of beam Line X-27A at Brookhaven National Laboratory.

National Laboratory. A schematic of the experimental configuration with the associated instrumentation is shown in Figure 2.28. The test set-up includes (a) a X-ray synchrotron source with an energy range between 5Kev and 50Kev, (b) metal foils (typically aluminum or zirconium) to filter the incoming X-ray beam, (c) specimen alignment and rotation fixtures with precision controls, (d) a YAG:Ce scintillator crystal for converting the transmitted X-ray beam into a visible photon flux, (e) imaging optics and a Kodak KAF-1400 CCD camera with 1317 x 1035 pixels and (f) data acquisition in a Silicon Graphics workstation. Details of the experimental configuration at beam line X27A and its operation have been described by Dowd (1996) and Dowd, Andrews, Marr, Siddons, Jones and Peskin (1999). The overall resolution of tomographic imaging at beam line X27A is approximately $2.25\mu m$. In our experiments, the data read-out obtained at the CCD camera was binned from 2x2 adjacent pixels to increase the signal-to-noise ratio and reduce the overall data acquisition

time. Consequently, the resolution was decreased to approximately $4.5\mu m$.

The imaging sample is initially lowered out of the path of the X-ray beam and several projections of the white field are taken to provide and accurate measure of the intensity of the X-ray source. The sample is centered on the rotation stage and aligned such that its rotational axis is normal to the path of the X-ray beam. Radiographs or X-ray projections of the sample are obtained at fixed angular increments of the rotation stage ($0.5 degrees$) until the sample has rotated by 180 degrees.

The design of an optimal sample for tomographic imaging in X27A from the Al6XN stainless steel welded plate was a major undertaking in this phase of research. The variables involved in design of the sample relate mainly to (a) nature of loading history imposed on the test specimen from which the imaging sample is prepared, (b) location of the plastically deformed zone of the test specimen from which the sample is machined and (c) sample dimensions and shape.

While the schematic of XCMT in Figure 2.27 illustrates tomographic imaging of an irregularly shaped heterogeneous sample, it is not feasible in practice for high strength engineering alloys. Imaging of voided zones and investigation of void coalescence in AL6XN/INCONEL-625 alloys is a challenging experimental task due to the extremely fast and localized nature of the fracture process. The microstructure of these alloys do not contain any significant volume fraction of second phases or precipitates. Therefore, in order to maximize contrast between the intact matrix and any void clusters in the fracture process zone, the sample was chosen to be cylindrical in shape so that the cross-section through which the X-rays pass is circular. A cylindrical sample also allows one to increase the sampling time at each angular increment without saturating the CCD at certain orientations.

The maximum allowable sample dimension along the path of the X-ray beam is determined mainly by the attenuation of the incident X-ray beam and by the energy

conversion efficiency of the scintillator crystal. The attenuation of the X-ray beam is strongly dependent on both the sample thickness and elemental composition. The four major constituents of Al6XN/INCONEL-625 welds (Iron, Nickel, Chromium and Molybdenum) all have high atomic numbers (Z) and strongly attenuate X-rays. In our experiments at beam line X27A, our sample dimension along the path of the X-ray beam was in the range of $750\mu m - 1200\mu m$.

Imaging of cylindrical samples prepared from beneath the fracture surface of test specimens which had been previously loaded to complete failure indicated an absence of voids. It was concluded that the localized nature of the fracture process zone in these high-strength alloys resulted in a majority of the nucleated voids becoming a part of the eventual fracture surface. The remaining voids that are likely to have nucleated beneath the fracture surface are expected to be microvoids that go undetected. Additional difficulties were encountered in imaging these samples cut from the fracture subsurface due to the close proximity of the voided zone to the irregular sample surface. Diffraction of the X-ray beam near the sample edges (where voids are expected) resulted in poor contrast in the projected radiographs. It is therefore essential for the voided, fracture-process zone to be present in the interior of the imaging sample to ensure maximum contrast and visibility.

Figure 2.29 shows a schematic illustrating the preparation of an XCMT sample from a notched cylindrical AL6XN/INCONEL-625 tensile specimen. The tensile specimen was machined from the stainless steel welded plate such that the notch was located near the base/weld interface zone. The specimen was loaded in an Instron testing machine at a strain rate of $10^{-3}/sec$ and the test was interrupted when the specimen started unloading. As discussed previously, it is essential to retain the voided, fracture-process zone within the specimen for tomographic imaging in X27A. After the completion of the test, a section of the tensile specimen, containing the root

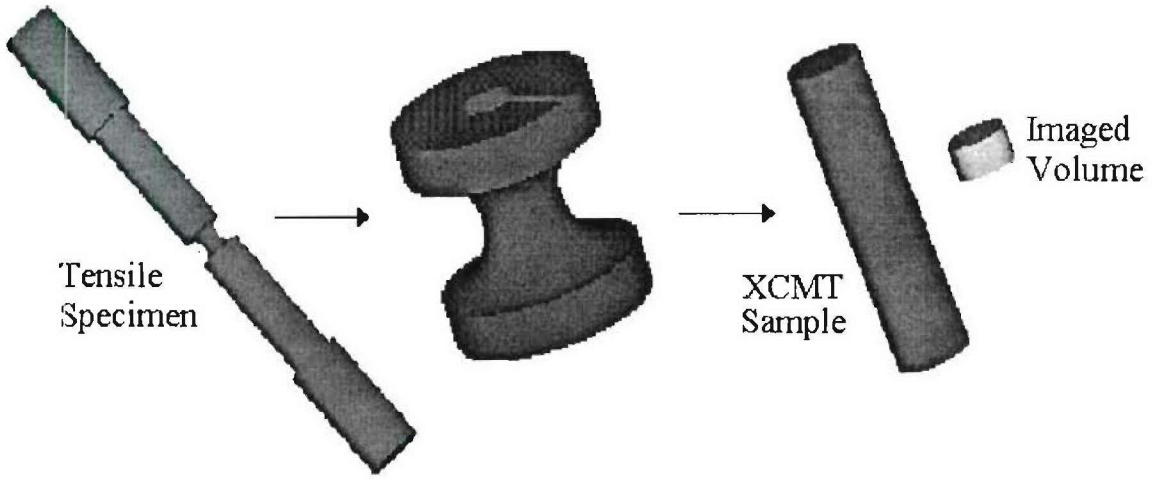

Figure 2.29: Preparation of the tomographic imaging sample from notched tensile specimen S3.

of the notch, was cut from the specimen. Electric Discharge Machining (EDM) was used to cut out a cylindrical imaging sample ($\phi 1.2mm$) from the plastically deformed root of the notch as shown in Figure 2.29. The damage introduced by the EDM process ($\approx 10\mu$ layer) is expected to be localized near the surface of the cylindrical sample and should not affect the interior microstructure.

Radiographs taken along the length of the cylindrical sample revealed the presence of voided zones in the interior. XCMT data slices were acquired in a small window around the location of these void clusters. A schematic of the cross-section of the imaging sample is shown in Figure 2.30. A volumetric reconstruction of the sample ($996\mu m$ height $\times$ $942\mu m$ diameter) is shown in Figure 2.31. The reconstructed image consists of a stack of 220 slices with each slice representative of data acquired by one row of pixels in the CCD. The image of X-ray attenuation coefficients is scaled from 0 to 255 such that white (intensity level 0) represents fully intact material and black (intensity level 255) represents fully voided material. With the specimen oriented as shown in Figure 2.31, the primary void cluster is visible over slices 147-163 ($\approx 77\mu m$). A microvoid cluster was also visible in the sample near the region where the base/weld

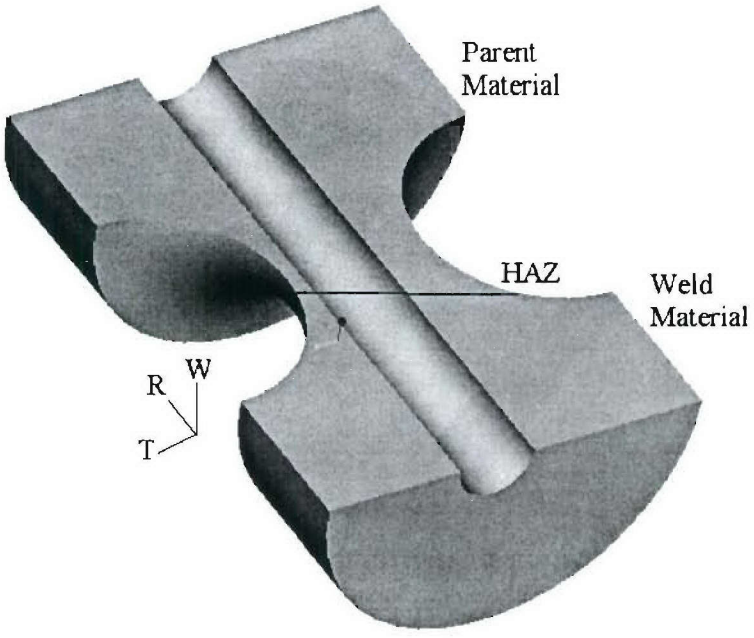

Figure 2.30: Location of acquired tomographic imaging data from the Base/Weld interface test specimen S3.

interface was expected. This location was later confirmed by polishing and etching the surface of the imaging sample to locate the interface. Features within this microvoid cluster were too small to be resolved in our experiments. A higher incident beam energy is needed to resolve the small size scale of the voids in these high strength alloys. Examination of individual data slices revealed additional detail near the region around the primary void cluster. A schematic of reconstructed slices 150, 155 and 160 from within the voided zone is shown in Figure 2.32. Two distinct voids with a narrow inter-void ligament are clearly visible in slice 155. The distance between these two voids ($\approx 100\mu m$) is comparable to the distance between two adjacent large voids on the base material fracture surface (see Figure 2.19).

A finite element simulation of deformation and damage evolution in tensile specimen S3 is presented in §4.4. The finite element model considers effects of the heterogeneous base/weld/HAZ material response to predict the onset of void nucleation,

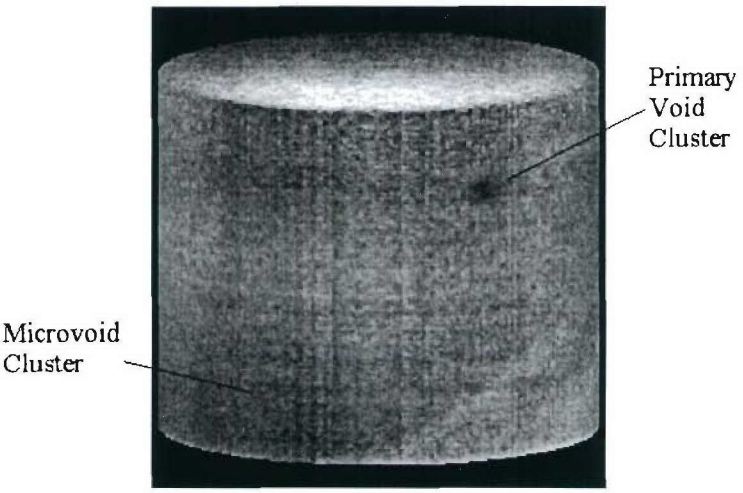

Figure 2.31: Tomographic image of the voided fracture process zone in notched AL6XN/INCONEL-625 tensile specimen S3.

void growth and coalescence. A detailed comparison of the location of the voided zones in the XCMT image with finite element simulations in ABAQUS/Explicit is presented in 4.4.

2.6 Summary

Results have been presented from an experimental investigation of the high rate plastic flow and fracture response of NITRONIC-50 and AL6XN stainless steel welded joints. The dynamic flow response in compression of specimens machined from the various material zones in the welded plate was obtained in a Kolsky bar configuration. These results indicated that the weld zone was undermatched by approximately 10% in comparison to the base material. The experiments also revealed that the HAZ is overmatched by approximately 5% compared to the base material.

The dynamic response of notched tensile specimens from the various material zones of the AL6XN plate P_C was also obtained under high rate tensile loading conditions in a Kolsky bar configuration. The results indicated a strong sensitivity to the location of the plastically deforming zone of the tensile specimen with respect to the HAZ/weld interface. While a full analysis of the tensile experiments on the AL6XN welded plate would require extensive finite element calculations, the ductility of the weld is obviously weaker than that of the base material. Under nominally identical loading conditions, the response of the HAZ tensile specimens showed a significant loss in ductility when compared to similar base/weld specimens. We believe that the preferential loss in ductility of these specimens arises out of the nature of porous viscoplastic flow behavior across the dissimilar HAZ/weld interface. In Chapter 3, we will develop a finite-deformation constitutive model for porous, elastic-viscoplastic materials. Based on this constitutive framework, we will conduct finite element simulations of the evolution of deformation and damage in notched tensile specimens machined from the AL6XN welded plate P_C. The results from these numerical simulations are presented in Chapter 4.

This chapter has also presented the results from a X-ray tomographic investigation of the fracture process zone in Al6XN stainless steel weldments. In Chapter 4, we

will compare the results from a finite element simulation of damage evolution in a notched cylindrical AL6XN/INCONEl-625 tensile specimen with reported XCMT observations.

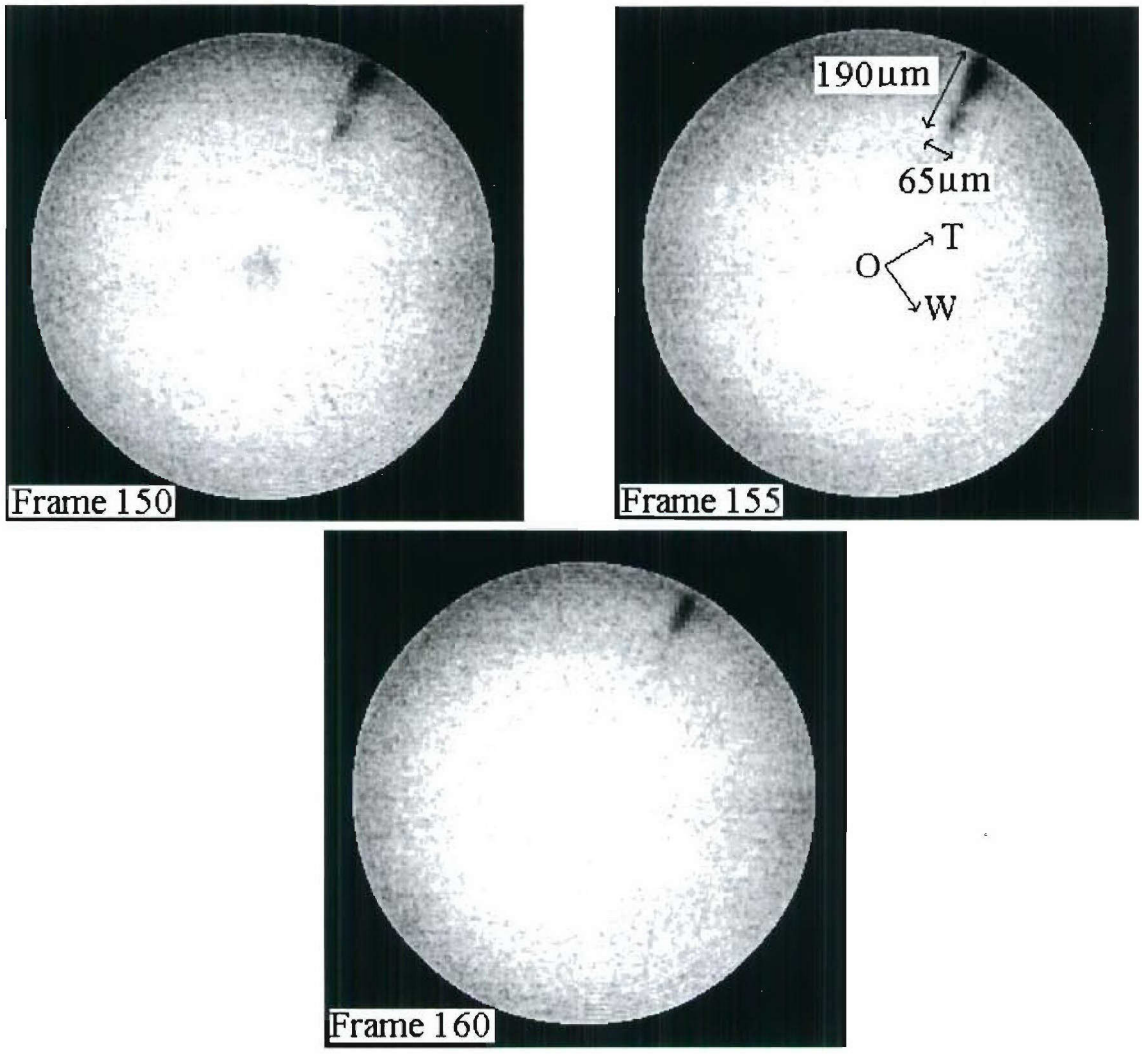

Figure 2.32: Reconstructed images from the primary void cluster in tensile specimen S3 obtained using XCMT. Two distinct voids can be seen within the primary void cluster. The orientation of the Transverse (T) and Weld (W) directions are shown in Frame 155. The center of the tensile specimen is offset from the center of the XCMT data slice (indicated as O) by $220\mu m$ along the positive T-direction.

Chapter 3

A Computational Model for Ductile Fracture based on Void Nucleation, Growth and Coalescence

3.1 Introduction

Experimental observations on the high-strain-rate deformation and fracture of AL6XN stainless steel welded plates were presented in Chapter 2. The flow response of the weld material was shown to be undermatched relative to the response of the base material. The HAZ was shown to be slightly overmatched when compared to both the adjacent weld and base material zones. A rich variety of behavior was also evident in the high-strain-rate tensile response of specimens machined from the various material zones of the welded plate. A dramatic loss in ductility was observed in some specimens where the plastically deforming zone was located near the HAZ/weld

interface.

To advance the understanding of the observed phenomena as well as to provide computational tools for the design of stainless steel welds against failure, we consider next the numerical simulations of the experiments. The modeling of ductile fracture has received considerable attention from researchers over several decades. The micromechanics of the growth of a single void in an infinite elastic-plastic solid was analyzed by McClintock (1968) and Rice and Tracey (1969). Some of the earliest numerical studies of void growth were carried out by Needleman (1972). Gurson (1977) analyzed a cell model for spherical void growth and obtained a phenomenological constitutive relation for a porous plastic solid. This work was later extended by Tvergaard (1981, 1982) and Tvergaard and Needleman (1984). A viscoplastic version of the Gurson constitutive relation was analyzed by Pan, Saje and Needleman (1983). Becker, Needleman, Suresh, Tvergaard and Vasudevan (1989) developed a finite element model based on the Gurson constitutive relation to model crack propagation along grain boundaries. A computational cell model based on the Gurson constitutive relation was developed by Xia and Shih (1995) to study the geometry-dependence of crack-growth resistance curves under plane strain conditions.

The Gurson constitutive model has been generally successful in modeling the void growth stage of ductile fracture. It does not however, provide an explicit failure criterion. The most common criterion used to trigger the onset of void coalescence is to assume that coalescence occurs at a critical void volume fraction. It is not quite clear under what conditions a failure condition based solely on a critical void volume fraction would be valid. Recent investigations intended to improve the application of Gurson-type models for ductile fracture have focused on modeling the onset of coalescence and the post-coalescence behavior. They take into account the influence

of imposed stress triaxiality, void shape and void spacing (Gologanu (1997), Gologanu, Leblond, Perrin and Devaux (2001), Benzerga (2000), Pardoen and Hutchinson (2000)).

A finite-deformation, porous, elastic-viscoplastic constitutive model for dynamic fracture is presented in this chapter. The effects of strain hardening, rate sensitivity, material inertia and adiabatic heating have been included in the simulation of the plastic flow behavior of the base/weld/HAZ material. The model used for simulation of the high-strain-rate tensile response includes void nucleation, a Gurson-type constitutive relation for void growth and a criterion for the onset of void coalescence based on the upper-bound velocity fields of Thomason (1985). Evolutionary equations are developed for characterizing the material response after the onset of void coalescence by accounting for local changes in void shape and spacing. Details regarding the numerical integration of the equations together with a finite element implementation in ABAQUS/Explicit, are presented here.

Second order tensors are indicated with bold face upper case letters, e.g. $\mathbf{F}^e$ and $\mathbf{F}^p$; while fourth order tensors are represented by bold face calligraphic letters, e.g. $\mathcal{C}$. The product of two second order tensors $\mathbf{F}^e$ and $\mathbf{F}^p$ is shown as $\mathbf{F}^e\mathbf{F}^p$ (also a second order tensor). The scalar product of two second order tensors Σ and $\mathbf{D}$ is denoted by $\Sigma : \mathbf{D}$. The dyadic product of two second order tensors $\mathbf{A}$ and $\mathbf{B}$ is indicated by $\mathbf{A} \otimes \mathbf{B}$. The contraction of a fourth order tensor $\mathcal{C}$ with a second order tensor $\mathbf{D}^e$ is indicated by $\mathcal{C} : \mathbf{D}^e$ (and results in a second order tensor).

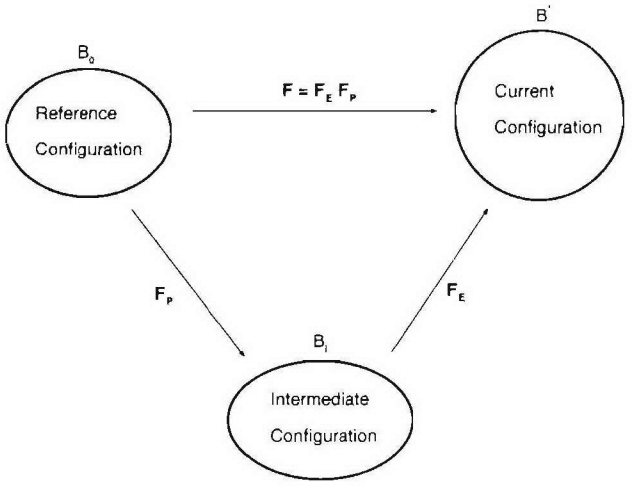

Figure 3.1: Elasto-plastic decomposition of the deformation gradient $\mathbf{F}$.

3.2 A Finite Deformation Porous Elastic Viscoplastic Constitutive Model

The framework of our finite-deformation constitutive model is based on the multiplicative decomposition of the overall deformation gradient (Lee 1969) into its elastic and plastic parts. A schematic of the decomposition of the overall deformation at a material point is shown in Figure 3.1. In Fig. 3.1, B_0 is the reference configuration. The decomposition introduces an intermediate configuration B_I, obtained by elastic unloading of the material point from the current configuration B^*. Consider a multiplicative decomposition of the overall deformation gradient $\mathbf{F}$ as

$$\mathbf{F} = \mathbf{F}^e\mathbf{F}^p \tag{3.1}$$

where $\mathbf{F}^e$ is the deformation due to elastic stretching and rotation and $\mathbf{F}^p$ is due to the plastic flow of material. The velocity gradient $\mathbf{L}$ defined by

$$\mathbf{L} = \dot{\mathbf{F}}\mathbf{F}^{-1} \tag{3.2}$$

can be decomposed into its elastic and plastic components using Eqn. 3.1. The elastic and plastic components of $\mathbf{L}$ can be further decomposed into symmetric and skew-symmetric components according to

$$\mathbf{L} = \mathbf{L}^e + \mathbf{F}^e\mathbf{L}^p\mathbf{F}^{e-1} \tag{3.3}$$

$$\mathbf{L}^e = \dot{\mathbf{F}}^e\mathbf{F}^{e-1} = \mathbf{D}^e + \Omega^e \tag{3.4}$$

$$\mathbf{F}^e\mathbf{L}^p\mathbf{F}^{e-1} = \mathbf{F}^e\dot{\mathbf{F}}^p\mathbf{F}^{p-1}\mathbf{F}^{e-1} = \mathbf{D}^p + \Omega^p. \tag{3.5}$$

The symmetric part of the velocity gradient is defined as the rate of deformation tensor $\mathbf{D}$ and the skew-symmetric part of the velocity gradient is defined as the rate of spin tensor Ω. Assuming the plastic spin Ω^p to vanish, we can write

$$\mathbf{D} = \mathbf{D}^e + \mathbf{D}^p \tag{3.6}$$

$$\Omega = \Omega^e. \tag{3.7}$$

The stress power $\mathbf{P}$, per unit reference volume is given by

$$P = J\mathbf{\Sigma} : \mathbf{D} = \boldsymbol{\tau} : \mathbf{D} \tag{3.8}$$

where $\mathbf{\Sigma}$ and $\mathbf{D}$ are the Cauchy stress and deformation rate measures in the current configuration and $\boldsymbol{\tau}$ is the Kirchoff stress. The quantity J is the Jacobian of the deformation and is given by

$$J = \det(\mathbf{F}). \tag{3.9}$$

Assume that the elastic stresses are derived from a potential ψ, representing the strain energy density per unit volume in the reference configuration. If the elastic deformation is assumed to be infinitesimal, the elastic response can be characterized by

$$\mathbf{S} = \frac{\partial\psi}{\partial\mathbf{E}^e} = \mathcal{C}^e : \mathbf{E}^e \tag{3.10}$$

where $\mathbf{S}$ represents the second Piola-Kirchoff stress tensor and $\mathbf{E}^e$ the corresponding work-conjugate deformation measure, defined by

$$\mathbf{E}^e = \frac{1}{2}(\mathbf{F}^{eT}\mathbf{F}^e - \mathbf{I}). \tag{3.11}$$

For elastic isotropy, $\mathcal{C}^e$ is given by the fourth-order tensor of elastic moduli as

$$\mathcal{C}^e = \frac{E}{1+\nu}(\mathcal{I}^* + \frac{\nu}{1-2\nu}\mathbf{I}\otimes\mathbf{I}) \tag{3.12}$$

where E and ν are the Young's modulus and Poisson's ratio, $\mathcal{I}^*$ is a fourth-order identity tensor, $\mathbf{I}$ is a second-order identity tensor and $\otimes$ represents the tensor dyadic product. The Kirchoff stress $\boldsymbol{\tau}$ is related to the second Piola-Kirchoff stress $\mathbf{S}$ by

$$\boldsymbol{\tau} = \mathbf{F}^e\mathbf{S}\mathbf{F}^{eT}. \tag{3.13}$$

Differentiating Eqn. 3.13 and using Eqn. 3.4, we get

$$\dot{\boldsymbol{\tau}} = (\mathbf{D}^e + \Omega^e)\boldsymbol{\tau} + \mathbf{F}^e\dot{\mathbf{S}}\mathbf{F}^{eT} + \boldsymbol{\tau}(\mathbf{D}^e - \Omega^e) \tag{3.14}$$

where $\dot{\boldsymbol{\tau}}$ is the convected derivative of the Kirchoff stress. For development of constitutive models, a more useful stress rate is the corotational derivative (or the Jaumann rate) of the Kirchoff stress. The Jaumann rate of the Kirchoff stress $\boldsymbol{\tau}$ is given by

$$\overset{\Delta}{\boldsymbol{\tau}} = \dot{\boldsymbol{\tau}} - \Omega^e\boldsymbol{\tau} + \boldsymbol{\tau}\Omega^e. \tag{3.15}$$

Substitution of Eqn. 3.15 into Eqn. 3.14 gives

$$\overset{\Delta}{\boldsymbol{\tau}} = \mathbf{F}^e\ \mathcal{C}^e : \dot{\mathbf{E}}^e\ \mathbf{F}^{eT} + \mathbf{D}^e\boldsymbol{\tau} + \boldsymbol{\tau}\mathbf{D}^e. \tag{3.16}$$

Differentiating Eqn. 3.11 and substituting into Eqn. 3.16, we get

$$\overset{\Delta}{\boldsymbol{\tau}} = \mathcal{C}^* : \mathbf{D}^e + \mathbf{D}^e\boldsymbol{\tau} + \boldsymbol{\tau}\mathbf{D}^e \tag{3.17}$$

where $\mathcal{C}^*$ is given by

$$\mathcal{C}^* = \mathbf{F}^e\mathbf{F}^e\mathcal{C}^e\mathbf{F}^{eT}\mathbf{F}^{eT}. \tag{3.18}$$

For small elastic deformations of an isotropic material, Eqn. 3.18 simplifies to $\mathcal{C}^* = \mathcal{C}^e$. In addition, the last two terms of Eqn. 3.17 can be neglected if the magnitudes of the stress components are much smaller than the elastic moduli. Eqn. 3.17 can then be written as

$$\overset{\Delta}{\boldsymbol{\tau}} = \mathcal{C}^e : (\mathbf{D} - \mathbf{D}^p). \tag{3.19}$$

Including deformation due to thermal straining, we can rewrite Eqn. 3.19 as

$$\overset{\Delta}{\boldsymbol{\tau}} = \mathcal{C}^e : (\mathbf{D} - \mathbf{D}^p - \mathbf{D}^T) \tag{3.20}$$

where $\mathbf{D}^T$ is given by

$$\mathbf{D}^T = \alpha \dot{\theta_m} \mathbf{I}. \tag{3.21}$$

Here, α is the thermal coefficient of expansion and θ_m is the temperature at the material point.

3.3 The Gurson Model for Porous Viscoplastic Solids

To complete the operations required for describing the plastic flow response of each of the materials we need viscoplastic constitutive equations for calculating $\mathbf{D}^p$. Our formulation of the viscoplastic response of voided microstructures relies on Gurson's constitutive model (Gurson 1977) for porous plastic solids. The model introduces two scalar internal state variables to characterize the microstructure of the voided material. The accumulation of damage in the material is characterized by the void volume fraction f. The strain hardening of the incompressible matrix material surrounding the voids is characterized by its effective flow stress σ_m. A schematic of the idealized voided microstructure with the state variable representation is shown in

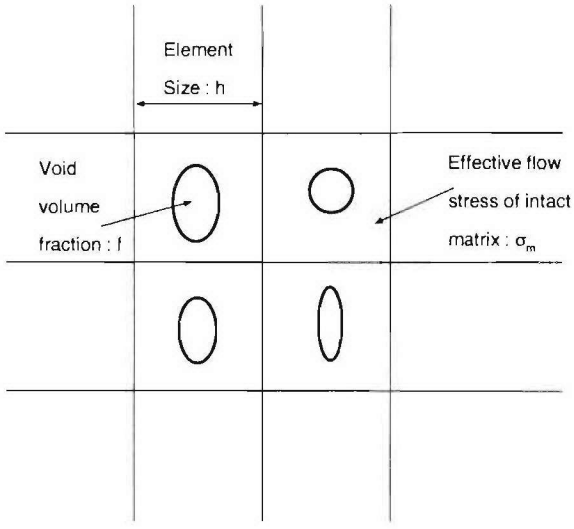

Figure 3.2: Schematic of the voided microstructure represented by two internal state variables: f and σ_m.

Figure 3.2. Let $\mathbf{\Sigma}$ represent the macroscopic Cauchy stress at the material point. The Gurson model for porous viscoplastic solids consists of an associative flow potential $\Phi(\mathbf{\Sigma}, \sigma_m, f)$ together with evolution laws for the two state variables f and σ_m. The flow potential $\Phi(\mathbf{\Sigma}, \sigma_m, f)$ can be written in the form

$$\Phi(\mathbf{\Sigma}, \sigma_m, f) = \frac{\Sigma_G^2}{\sigma_m^2} + 2q_1 f \cosh(\frac{3q_2\Sigma_h}{2\sigma_m}) - 1 - q_1^2 f^2. \tag{3.22}$$

Here, Σ_G and Σ_h are, respectively, the macroscopic flow stress and hydrostatic stress given by

$$\Sigma_G^2 = \frac{3}{2}\mathbf{\Sigma}' : \mathbf{\Sigma}' \tag{3.23}$$

$$\Sigma_h = \frac{1}{3}\mathbf{\Sigma} : \mathbf{I} \tag{3.24}$$

where $\mathbf{\Sigma}' = \mathbf{\Sigma} - \Sigma_h \mathbf{I}$ is the macroscopic deviatoric stress tensor. The coefficients q_1, q_2 were introduced by Tvergaard (1981, 1982) to match predictions of the Gurson model

with full finite elements simulations of periodic voided microstructures. The plastic part of the rate of deformation tensor $\mathbf{D}^p$ is derived from the Gurson potential (Eqn. 3.22) by assuming associative flow

$$\mathbf{D}^p = \Lambda \frac{\partial \Phi}{\partial \boldsymbol{\Sigma}}. \tag{3.25}$$

The pre-factor Λ is derived by equating the macroscopic rate of plastic work to the internal dissipation in the matrix, *i.e.*

$$\boldsymbol{\Sigma} : \mathbf{D}^p = (1-f)\sigma_m \dot{\epsilon}_m \tag{3.26}$$

where $\dot{\epsilon}_m$ is the effective matrix strain rate. Substituting Eqn. 3.25 in Eqn. 3.26, we obtain

$$\Lambda = \frac{(1-f)\sigma_m \dot{\epsilon}_m}{\boldsymbol{\Sigma} : \frac{\partial \Phi}{\partial \boldsymbol{\Sigma}}}. \tag{3.27}$$

Substituting for Λ in Eqn. 3.25, we find

$$\mathbf{D}^p = \Lambda \left[\frac{3}{\sigma_m^2} \boldsymbol{\Sigma}' + \frac{q_1 q_2 f}{\sigma_m} \sinh\left(\frac{3 q_2 \Sigma_h}{2\sigma_m} \right) \mathbf{I} \right]. \tag{3.28}$$

The evolution of the damage parameter f is determined by the growth of existing voids in the surrounding incompressible matrix and through the initiation of new nucleation sites in the matrix. Nucleation of new voids at the sites of large inclusions takes place by particle cracking or interface debonding through a process that is assumed to be stress-controlled. The growth of fine scale inclusions is assumed to be a strain-controlled process and is activated typically after the primary nucleation event from the sites of the larger inclusions. The overall rate of evolution of the void volume fraction is given by

$$\dot{f} = \underbrace{(1-f)\mathbf{D}^p : \mathbf{I}}_{growth} + \underbrace{N_\epsilon \dot{\epsilon}_m + N_\sigma (\dot{\sigma}_m + \dot{\Sigma}_h)}_{nucleation} \tag{3.29}$$

where N_ϵ and N_σ are given by (Chu and Needleman 1980)

$$N_\epsilon = \frac{f_N^\epsilon}{s_N^\epsilon \sqrt{2\pi}} \exp\left[-\frac{1}{2}\left(\frac{\bar{\epsilon}_m - \epsilon_c}{s_N^\epsilon}\right)^2\right] \tag{3.30}$$

$$N_\sigma = \frac{f_N^\sigma}{s_N^\sigma \sqrt{2\pi}} \exp\left[-\frac{1}{2}\left(\frac{\bar{\sigma}_m + \Sigma_h - \sigma_c}{s_N^\sigma}\right)^2\right]. \tag{3.31}$$

For a void nucleation mechanism controlled by the plastic strain (*i.e.* $N_\sigma = 0$), f_N^ϵ represents the volume fraction of strain-controlled void nucleating particles and $\bar{\epsilon}_m$ is the accumulated effective strain in the matrix. The void nucleation strain is assumed to follow a normal distribution with a mean given by ϵ_c and standard deviation characterized by s_N^ϵ. Similarly for the stress-controlled void nucleation mechanism ($N_\epsilon = 0$), f_N^σ represents the volume fraction of stress-controlled void nucleating particles, and the void nucleation stress is assumed to follow a normal distribution with a mean given by σ_c and standard deviation characterized by s_N^σ.

The evolution of the matrix effective stress σ_m is determined by the assumed constitutive model for the incompressible matrix. Material models for the strain hardening of stainless steel AL6XN and IN-625 superalloy are discussed briefly in the following sections. In particular, the effective strain rate in the matrix $\dot{\epsilon}_m$ in Eqn. 3.26 is determined from the assumed constitutive model for the matrix material.

The evolution of temperature θ_m, at the material point under assumed adiabatic conditions is given by

$$\rho_m c_p \dot{\theta_m} = \beta \sigma_m \dot{\epsilon}_m \tag{3.32}$$

where ρ_m is the density of the matrix, c_p is the specific heat capacity of the matrix and β is the fraction of the plastic work converted to heat.

A Constitutive Model for Stainless Steel AL6XN

The thermo-mechanical response of stainless steel AL6XN over a wide range of strain rates and temperatures has been investigated recently by Nemat-Nasser *et al.* (2000). We will adopt their framework to model the constitutive response of AL6XN in the base metal and in the heat-affected zone (HAZ). For the range of strain rates and temperatures of interest in this study, we neglect the effects of creep and diffusion and assume that plastic flow of material in the matrix is due solely to dislocation motion. The primary internal variable characterizing the evolution of the microstructure is the average dislocation density and its distribution. As in Nemat-Nasser *et. al.* (2000), we assume that the overall flow stress of the matrix σ_m can be decomposed into three parts

$$\sigma_m(\epsilon_m, \dot{\epsilon}_m, T) = \sigma_a + \sigma_d + \sigma^* \tag{3.33}$$

where σ_a is the contribution due to athermal hardening, σ_d is the contribution from viscous-drag effects at high strain rates and high temperatures and σ^* is the contribution to the flow stress from thermally-activated motion of dislocations past short-range barriers.

The athermal hardening of the microstructure is due to the effect of long-range stress fields of dislocation forests and grain boundaries on dislocation motion. Assuming that the accumulated plastic strain ϵ_m to be representative of the average dislocation density, we approximate the athermal hardening component of the flow stress as

$$\sigma_a = \sigma_0 + \tau_{a0}\epsilon_m^n \tag{3.34}$$

where σ_0 and τ_{a0} are constants, ϵ_m is the accumulated plastic strain in the matrix material and n is a strain-hardening exponent. The viscous-drag component σ_d is activated only at high strain rates ($> 10^3/sec$) due to the presence of phonon-drag

effects on the mobility of dislocations. This effect is modeled as

$$\sigma_d = m_0(1 - \exp(-\alpha_s \dot{\epsilon}_m)) \tag{3.35}$$

where m_0 is a material constant representing the high-temperature, high-strain-rate flow stress and α_s is a viscous damping coefficient. The remaining contribution to the flow stress comes from the thermally-activated motion of dislocations past obstacles (alloying elements, precipitates, interstitials, Peirls barrier). This effect is modeled as

$$\sigma^* = \tau_0 \left\{ 1 - \left(-\frac{KT}{G_0} \ln \frac{\dot{\epsilon}_m f(\epsilon_m, T)}{\dot{\epsilon}_0} \right)^{1/q} \right\}^{1/p} \tag{3.36}$$

where the function $f(\epsilon_m, T)$ is given by

$$f(\epsilon_m, T) = 1 + a \left\{ 1 - \left(\frac{T}{T_m} \right)^2 \right\} \epsilon_m^r. \tag{3.37}$$

Here, G_0 is the free energy required by a dislocation to overcome the obstacle by thermal activation alone, k is the Boltzmann constant, $\dot{\epsilon}_0$ is a reference strain rate, τ_0, p and q are parameters that characterize the strength and profile of the energy barrier at the obstacle and $f(\epsilon_m, T)$ is a function characterizing the evolution of the average dislocation spacing. The above constitutive model was used to fit experimental AL6XN stainless steel flow stress data measured under quasi-static conditions in an Instron test machine and under high-strain-rate conditions in a Kolsky Bar configuration. Results from a least-squares best-fit routine used to match model parameters with experimental data are shown in Figure 3.3. Table 3.1 shows the material parameters for AL6XN stainless steel that best fit the response of the base material (JD-197-AL6XN) in compression. As described in §2.2, the response of the HAZ was overmatched by $\approx 5\%$ compared to that of the base material. The material parameters $\sigma_0, \tau_{a0}, m_0, \tau_0$ for the HAZ are therefore chosen to be 5% higher than corresponding values for the base material.

Material Parameter	Description	AL6XN Stainless steel
E	Elastic Modulus	208 GPA
ν	Poisson's Ratio	0.30
ρ_m	Density	8040.0 Kg/m^3
α	Thermal Expansion Coefficient	1.0e-5 /Kelvin
β	Eqn. 3.32: Adiabatic Heating	0.90
c_p	Specific Heat	500.0 J/Kg-Kelvin
T_m	Melting Point	1673.0 K
T_0	Reference Temperature	273.0 K
σ_0	Initial Athermal Hardness	400.0 MPa
τ_{a0}	Eqn. 3.34: Athermal Hardening	1280.0 MPa
n	Athermal Hardening Exponent	0.375
m_0	Viscous Drag Stress	140.0 MPa
α_s	Viscous Damping Coefficient	3.0×10^{-4} sec
τ_0	Dislocation Obstacle Strength	455 MPa
K/G_0	Temperature Sensitivity	6.6×10^{-5} /Kelvin
$\dot{\epsilon}_0$	Reference Strain Rate	2×10^{10} /sec
p	Dislocation Barrier Energy Profile	2/3
q	Dislocation Barrier Energy Profile	2.0
a	Dislocation Spacing Parameter	5.0
r	Dislocation Spacing Parameter	0.5

Table 3.1: Material parameters in the constitutive model for AL6XN stainless steel.

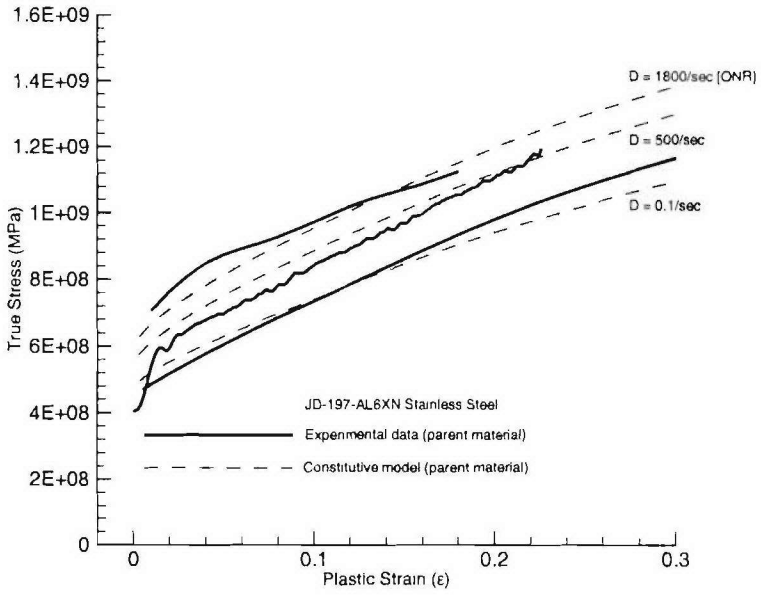

Figure 3.3: Constitutive model for the strain hardening of AL6XN stainless steel.

A Constitutive Model for INCONEL-625 Superalloy

The constitutive modeling framework used to model the base metal was also used to model the strain-hardening behavior of the weld Inconel-625 superalloy. Results from a least-squares best-fit routine used to match model parameters with experimental weld data are shown in Figure 3.4. Table 3.2 shows the material parameters for the weld metal that best fit the response of the material (JD-197-AL6XN-IN625) in compression.

In the final stages of void coalescence and complete failure, the localized mode of deformation can lead to enormously high strain rates and matrix hardening due to the exponential nature of Eqn. 3.36. A limiting strain rate has to be imposed to handle the numerical difficulties associated with integrating the matrix material response at very strain rates for a short period of time preceding complete failure of the finite element. A limiting strain rate is introduced by computing the effective

Material Parameter	Description	INCONEL-625 Superalloy
E	Elastic Modulus	212 GPA
ν	Poisson's Ratio	0.30
ρ_m	Density	8400.0 Kg/m^3
α	Thermal Expansion Coefficient	1.0e-5 /Kelvin
β	Eqn. 3.32: Adiabatic Heating	0.90
c_p	Specific Heat	500.0 J/Kg-Kelvin
T_m	Melting Point	1673.0 K
T_0	Reference Temperature	273.0 K
τ_{a0}	Eqn. 3.34: Athermal Hardening	1350.0 MPa
σ_0	Initial Athermal Hardness	400.0 MPa
n	Athermal Hardening Exponent	0.400
m_0	Viscous Drag Stress	125.0 MPa
α_s	Viscous Damping Coefficient	3.0×10^{-4} sec
τ_0	Dislocation Obstacle Strength	235 MPa
K/G_0	Temperature Sensitivity	6.6×10^{-5} /Kelvin
$\dot{\epsilon}_0$	Reference Strain Rate	2×10^{10} /sec
p	Dislocation Barrier Energy Profile	2/3
q	Dislocation Barrier Energy Profile	2.0
a	Dislocation Spacing Parameter	5.0
r	Dislocation Spacing Parameter	0.5

Table 3.2: Material Parameters in the constitutive model for INCONEL-625 superalloy.

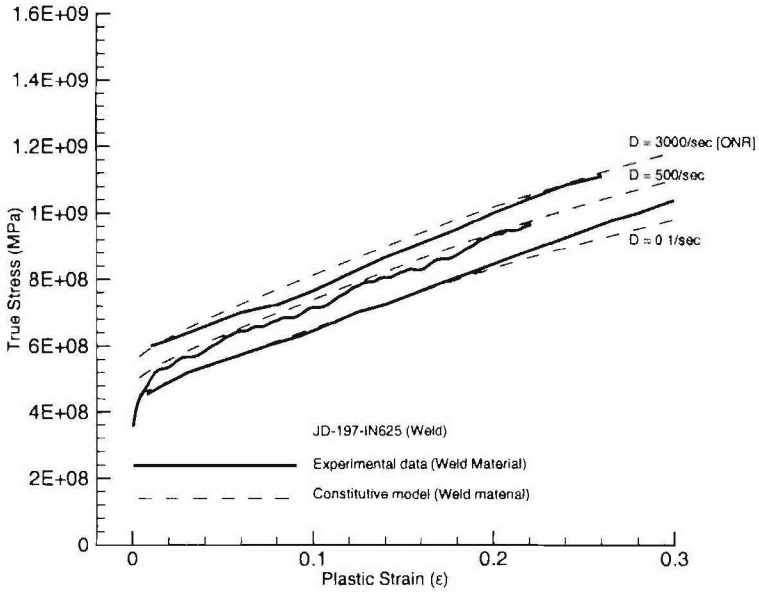

Figure 3.4: Constitutive model for the strain hardening of INCONEL-625 superalloy.

matrix strain rate as

$$\frac{1}{\dot{\epsilon}_m} = \frac{1}{\dot{\epsilon}_m^R} + \frac{1}{\dot{\epsilon}_m^C}. \tag{3.38}$$

Here, $\dot{\epsilon}_m^C$ is the strain rate computed using the constitutive model as described above, and $\dot{\epsilon}_m^R$ is a limiting strain rate ($\approx 7.5 \times 10^5$). This limiting strain rate is well beyond the range of strain rates for which we have valid experimental data for AL6XN.

3.4 The Post-coalescence Model of Tvergaard and Needleman

In the Gurson-Tvergaard-Needleman (GTN) model for ductile fracture, the primary internal variable characterizing the geometry of the voided material prior to coalescence is the void volume fraction f. The viscoplastic GTN flow potential prior to

coalescence is given by

$$\Phi_{c_-} = \frac{\Sigma_G^2}{\sigma_m^2} + 2q_1 f \cosh(\frac{3q_2\Sigma_h}{2\sigma_m}) - 1 - q_1^2 f^2. \tag{3.39}$$

In the post-coalescence regime, the primary internal variable characterizing the geometry of the voided zone is the isotropic variable f^* derived from the void volume fraction f. The modified void volume fraction f^* is defined as

$$f^*_{c_-} = f \tag{3.40}$$

$$f^*_{c_+} = f_c + \frac{f^*_u - f_c}{f_f - f_c}(f - f_c) = f_c + \delta(f - f_c). \tag{3.41}$$

Here, f_c is the critical void volume fraction signaling the onset of void coalescence. δ is an acceleration parameter (> 1) used to enhance void growth after coalescence. The modified GTN flow potential after coalescence is given by

$$\Phi_{c_+} = \frac{\Sigma_G^2}{\sigma_m^2} + 2q_1 f^* \cosh(\frac{3q_2\Sigma_h}{2\sigma_m}) - 1 - q_1^2 f^{*2}. \tag{3.42}$$

A schematic of the modified GTN flow potential after coalescence is shown in Figure 3.5. The primary motivation for the construction of the modified flow potential is the unrealistically large values of ductilities predicted by the continued use of Φ_{c_-} after coalescence. As shown in Figure 3.5, the modification to the flow potential after coalescence leads to a rotation of the normal (or the direction of straining) towards the hydrostatic axis.

In Eqn. 3.42, as $f \to f_f$, the function f^* approaches the ultimate void volume fraction $f^*_u = 1/q_1$, wherein the material is assumed to have lost all stress carrying capacity. In practice, the failure of the material element is initiated when $f^* = 0.9f^*_u$ to avoid numerical difficulties. The failed element is thereafter unloaded elastically over a few time increments following $f^* = 0.9f^*_u$ and is removed from the finite element assembly when it is fully unloaded. The use of the modified void volume fraction f^* therefore models the experimentally observed enhanced rate of void growth after

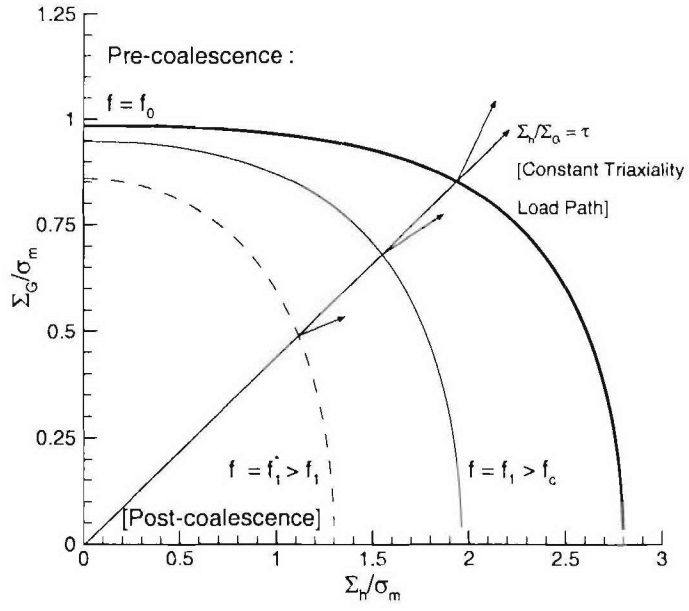

Figure 3.5: Modified GTN flow potential after the onset of void coalescence.

coalescence. Note that the overall framework of the viscoplastic GTN flow potential is still retained and the formulation relies on this modification of the void volume fraction to model the rapid loss of stress carrying capacity after the onset of void coalescence. This dual parameter description of the post-coalescence behavior has the added advantage of being simple to implement within an existing Gurson-type model for ductile fracture and qualitatively reproduces the final stages of material failure.

While it is obvious that the parameters (f_c, δ) depend on the material microstructure at coalescence, the identification of this functional dependence is non-trivial. Pardoen and Hutchinson (2000) have recently carried out an exhaustive study on the onset of void coalescence and the post-coalescence behavior using the computational void cell method of Needleman (1972). In particular, they have studied the influence of void shape, relative void spacing, strain hardening, imposed stress triaxiality and

initial void volume fraction on the critical void volume fraction f_c. A quantitative characterization of the dependence of f_c and the acceleration parameter δ on these microstructural variables could in principle be extracted from their results. However, it is more attractive to develop a physically-motivated model for the onset of coalescence and to collapse the functional dependencies derived from the void cell computations into a single relationship.

The onset of void coalescence in ductile materials signals the final stage of evolution of the microstructure before complete failure. As revealed by experimental observations (Garrison Jr and Moody 1987) and finite element calculations of void-containing unit-cells, (Koplik and Needleman (1988), Sovik and Thaulow (1997), Pardoen and Hutchinson (2000), Benzerga (2001)) void coalescence is characterized by localization of the plastic deformation in the inter-void ligament with the material immediately outside the localization band undergoing elastic unloading. In unit cell calculations, this transition to a localized mode of deformation is characterized by a macroscopic lateral strain rate becoming zero and the unit-cell undergoing uniaxial extension Koplik and Needleman (1988). This transition from a diffuse mode of deformation to a macroscopic uniaxial straining mode of deformation leads to an accelerated void growth in lateral directions and a rapid increase in the overall void volume fraction.

3.5 The Plastic Limit-Load Criterion for Void Coalescence

The primary goal of this section is to establish a critical condition for the onset of void coalescence in ductile materials. In addition, we will describe the evolution of the geometry of the voided material after coalescence and its implementation within

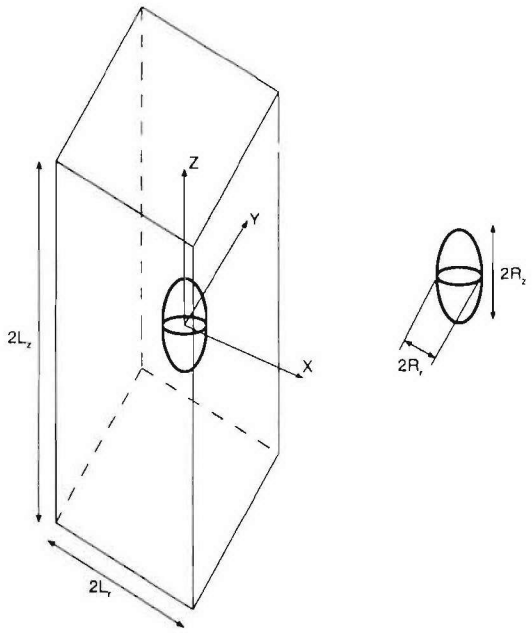

Figure 3.6: Geometry of the unit-cell containing the central ellipsoidal void.

a finite element framework.

Consider the schematic of the unit cell containing an ellipsoidal void as shown in Figure 3.6. The primary internal variables characterizing the geometry of the voided unit cell are the ligament ratio χ, void aspect ratio W and the void spacing ratio λ defined as below

$$\chi = \frac{R_r}{L_r} \tag{3.43}$$

$$W = \frac{R_z}{R_r} \tag{3.44}$$

$$\lambda = \frac{L_z}{L_r}. \tag{3.45}$$

The void volume fraction f in the unit-cell can be computed from the unit-cell geometry as

$$f = \frac{\pi}{12\gamma}\frac{\chi^3 W}{\lambda} \tag{3.46}$$

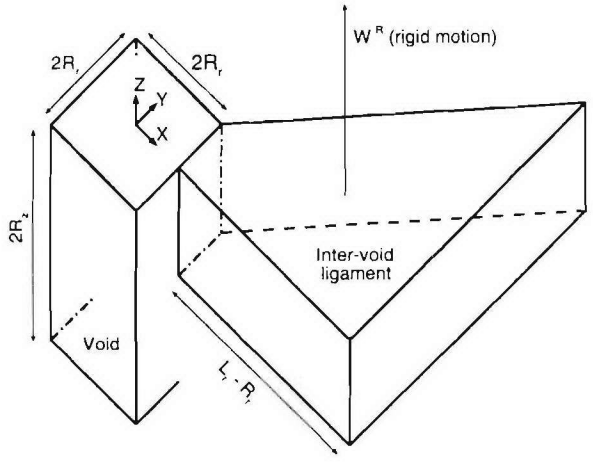

Figure 3.7: Geometry of the unit-cell containing the rectangular void with a trapezoidal inter-void ligament.

where γ (=1/2 for a spheroid) is a shape factor.

The onset of coalescence for elastic-perfectly plastic solids has been studied by Thomason (Thomason (1985), Thomason (1998)) using slip-line field solutions and upper-bound methods. Thomason analyzed the plastic limit mode of failure of a three-dimensional periodic array of square-prismatic cells by replacing the inner ellipsoidal void with a square-prismatic void. Consider the geometry of the equivalent unit cell containing the rectangular void and the velocity fields for the trapezoidal (Fig. 3.7 and prismatic (Fig. 3.8) inter-void regions. The velocity fields have to satisfy (a) the appropriate symmetry boundary conditions associated with the localized plastic zone, (b) incompressibility and (c) continuity of the normal component of velocity across the interface between the localized zone and the rigid region where the velocity is $\dot{W}^R$, parallel to the Z axis.

In the following analysis, the expressions for the velocity field and the plastic limit-load derived by Thomason (1985) will be re-written using the microstructural variables L_r, L_z, χ and W. A kinematically admissible velocity field in the plastically

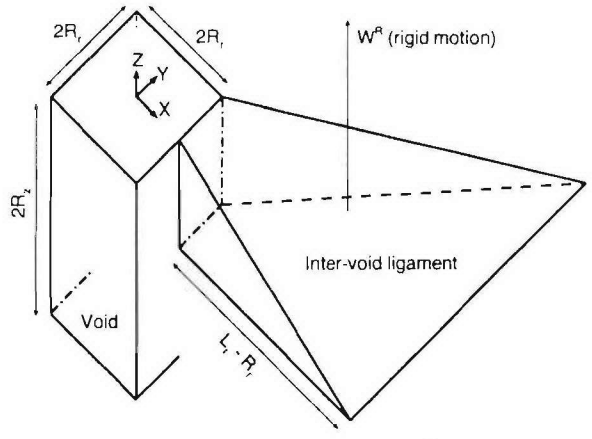

Figure 3.8: Geometry of the unit-cell containing the rectangular void with a prismatic inter-void ligament.

deforming zone shown in Fig. 3.7 is given by

$$\dot{u} = \frac{\dot{W}^R}{2R_z x}(L_r^2 - x^2) \tag{3.47}$$

$$\dot{v} = \frac{\dot{W}^R y}{2R_z x^2}(L_r^2 - x^2) \tag{3.48}$$

$$\dot{w} = \frac{\dot{W}^R z}{R_z}. \tag{3.49}$$

The tangential velocity discontinuity at the boundary between the deforming plastic zone and the rigidly moving portion of the unit-cell is given by

$$\dot{s} = \sqrt{\dot{u}_I^2 + \dot{v}_I^2}. \tag{3.50}$$

Here, $\dot{u}_I$ and $\dot{v}_I$ are evaluated at the interface between the plastically deforming zone of material in the inter-void ligament and the rigid zone. A kinematically admissible velocity field in the plastic deforming zone shown in Fig. 3.8 is given by

$$\dot{u} = \frac{\dot{W}^R(L_r - R_r)}{2R_z x}(L_r + x) \tag{3.51}$$

$$\dot{v} = \frac{\dot{W}^R y(L_r - R_r)}{2R_z x^2}(L_r + x) \tag{3.52}$$

$$\dot{w} = -\frac{\dot{W}^R z(L_r - R_r)}{2R_z x}. \tag{3.53}$$

The tangential discontinuity across the interface with the region that is moving rigidly upward is given by

$$\dot{s} = \frac{\dot{W}^R}{2x}(L_r + x)\left[1 + (\frac{L_r - R_r}{L_z})^2 + (\frac{y(L_r - R_r)}{xR_z})^2\right]^{1/2}. \tag{3.54}$$

The plastic limit-load Σ_{zz} for localization of plastic flow in the intervoid matrix is derived by equating the rate of internal energy dissipation for either of the above velocity fields $\dot{I}_i$, to the macroscopic rate of external work $\dot{I}_m$, *i.e,*

$$\dot{I}_i = \dot{I}_m \tag{3.55}$$

where $\dot{I}_i$ and $\dot{I}_m$ are given by

$$\dot{I}_i = \int_\Omega \sigma_m^L \dot{\epsilon}_m^L(x,y,z)dV + \int_S \frac{1}{\sqrt{3}}\sigma_m^L \dot{s}(x,y,z)dS \tag{3.56}$$

$$\dot{I}_m = 4L_r^2 \Sigma_{zz} \dot{W}^R. \tag{3.57}$$

Here σ_m^L represents the flow stress of the matrix material within the localized plastic zone and $\dot{\epsilon}_m^L(x,y,z)$ represents the corresponding effective strain rate computed from the velocity fields described earlier. The volume Ω is one-half of the total intervoid ligament volume and the surface S is one-half of the total surface between the plastically deforming ligament and the rigidly moving regions. For a range of representative values of χ and W, the plastic limit-load is obtained by numerical integration of the above equations and choosing the lower upper-bound obtained from either velocity field.

Thomason (1985) obtained a closed-form expression to represent the plastic limit-load variation as

$$\frac{\Sigma_{zz}}{\sigma_m^L} = (1 - \chi^2)C_F(\chi, W) \tag{3.58}$$

where the upper-bound constraint factor C_F is given by

$$C_F(\chi, W) = F\frac{(1-\chi)^2}{\chi^2 W^2} + G\chi^{-1/2}. \tag{3.59}$$

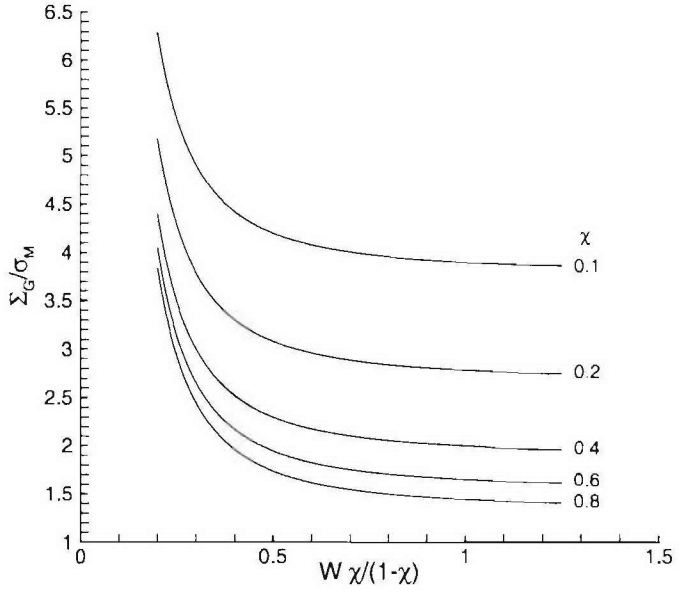

Figure 3.9: Plastic limit-load criterion for the onset of void coalescence.

In the original expression of Thomason (1985), F and G are constants equal to 0.1 and 1.2 respectively. A schematic of Eqn. 3.58 showing the functional dependence of plastic limit-load Σ_{zz} on the geometry of the inter-void matrix is shown in Figure 3.9. While Thomason (1985) carried out his analysis for an elastic-perfectly plastic solid, we use the current value of the matrix effective flow stress in Eqn. 3.58.

Onset of Void Coalescence

Pardoen and Hutchinson (2000) have carried out a rigorous comparison of the predictions of the above limit load criterion (Eqn. 3.58) with finite element simulations of unit-cells containing ellipsoidal voids. In their simulations, they use a rate independent J_2 elastoplastic constitutive model for the matrix material. They find that the onset of coalescence predicted by the plastic limit-load criterion to be extremely accurate irrespective of the void shape. A schematic of their results is shown in Figure

3.10. In Fig. 3.10, X and Y are given by

$$X = \frac{\Sigma_{zz}}{\sigma_m^L(1-\chi^2)} \tag{3.60}$$

$$Y = C_F(\chi, W). \tag{3.61}$$

Pardoen and Hutchinson (2000) also report a slight dependence of the Thomason (1985) constants F and G on the strain-hardening exponent.

Within a finite element framework for the evolution of voided microstructures, the onset of coalescence can be predicted by accounting for the evolution of the inter-void geometry, void shape, porosity and strain hardening of the matrix. At every time step during the explicit numerical integration procedure, the plastic limit-load needed to initiate failure of the inter-void matrix according to the constrained uniaxial straining deformation mode is compared with the principal normal stress in the element. Prior to the onset of coalescence, this virtual mode of deformation predicts a higher value of Σ_{zz} than the actual value in the unit-cell which deforms in a diffuse manner. However, at the onset of void coalescence, the diffuse mode of deformation in the unit-cell transitions into a localized mode and the principal macroscopic normal stress reaches the plastic limit-load as computed for the current inter-void geometry, void shape, porosity, and effective matrix stress. The critical void volume fraction f_c is, therefore, not a specified material parameter as in the GTN formulation. Instead, f_c and the critical ligament ratio χ_c are computed from the current inter-void geometry at the onset of coalescence.

Evolution of the Voided Microstructure in the Post-coalescence regime

In this section we will discuss a methodology to implement the evolution of the microstructure from the onset of coalescence to complete failure by necking of the

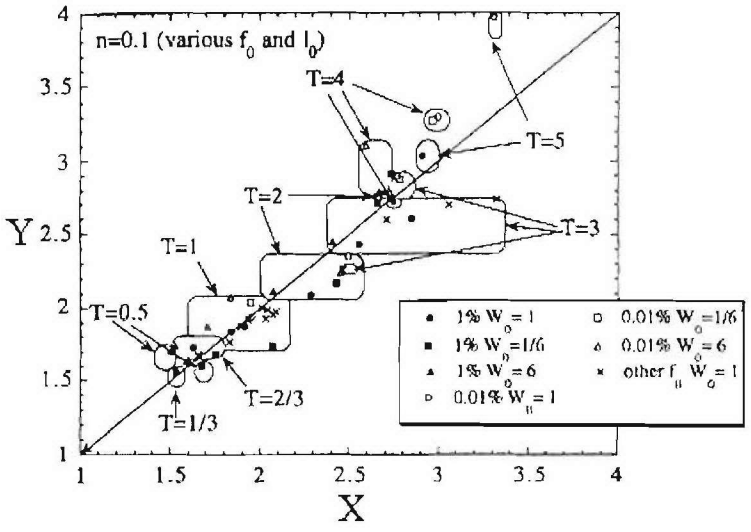

Figure 3.10: Comparison of finite element simulations of void coalescence with the Thomason upper-bound criterion.

intervoid ligament. The post-coalescence mode of deformation is fully determined by the following three assumptions:

(a) The macroscopic deformation is in a state of uniaxial straining with the lateral inter-void spacing remaining constant:

$$\dot{L}_r = 0. \tag{3.62}$$

(b) The extension strain of the ellipsoidal void is captured by the macroscopic axial strain:

$$\dot{R}_z = \dot{L}_z. \tag{3.63}$$

(c) The inter-void ligament supports the plastic limit-load computed from the current unit-cell geometry and matrix effective stress. Assuming an axisymmetric stress state, we can rewrite Eqn. 3.58 as

$$\left| \frac{\frac{2}{3}\Sigma_G + \Sigma_h}{\sigma_m^L} \right| = (1 - \chi^2) C_F(\chi, W). \tag{3.64}$$

Rewriting Eqn. 3.64, we associate the macroscopic viscoplastic flow behavior of the porous microstructure after void coalescence with a potential of the form

$$\Phi_{c_+} = \left(\frac{\Sigma_G + \frac{3}{2}\Sigma_h}{\sigma_m^L} \right)^2 - \frac{9}{4}(1-\chi^2)^2 C_F^2(\chi, W). \tag{3.65}$$

For associative plastic flow, the macroscopic rate of deformation after coalescence has the form

$$\mathbf{D}_{c_+}^p = \Lambda_{c_+} \left(\frac{\partial \Phi_{c_+}}{\partial \boldsymbol{\Sigma}} \right). \tag{3.66}$$

Prior to the onset of void coalescence, the pre-factor corresponding to Λ_{c_+} in Eqn. 3.66 is computed by equating the macroscopic dissipation with the internal dissipation in the entire matrix. However, after the onset of coalescence, such an approach is no longer valid because of the presence of elastic unloading zones surrounding the localized plastic flow in the inter-void ligament. Consider a schematic of the unit cell after the onset of coalescence as shown in Figure 3.11. The plastic flow is assumed to localize to a narrow band of height $2h$ as shown in Figure 3.11. The matrix material outside of the localization band is assumed to be rigid. Within the localization band, the matrix material is assumed to be incompressible and characterized by a Von Mises flow potential. Equating the macroscopic dissipation to the internal dissipation in the localized plastic zone, one obtains

$$V_c \boldsymbol{\Sigma} : \mathbf{D}_{c_+}^p = (V_p - V_v)\sigma_m^L \dot{\epsilon}_m^L. \tag{3.67}$$

where V_c is the volume of the unit-cell, V_p is the volume of the central porous layer and V_v is the volume of the void. Substitution of Eqn. 3.66 into (3.67) gives

$$\Lambda_{c_+} = \frac{V_p - V_v}{V_c} \frac{\sigma_m^L \dot{\epsilon}_m^L}{\boldsymbol{\Sigma} : \left(\frac{\partial \Phi}{\partial \boldsymbol{\Sigma}}\right)_{c_+}}. \tag{3.68}$$

The macroscopic rate of deformation tensor after coalescence is obtained as

$$\mathbf{D}_{c_+}^p = \dot{\epsilon}_m^L \left[\frac{3}{2\Sigma_G} \boldsymbol{\Sigma}' + \frac{1}{2} \mathbf{I} \right] H(\chi, W, \lambda, \gamma) \tag{3.69}$$

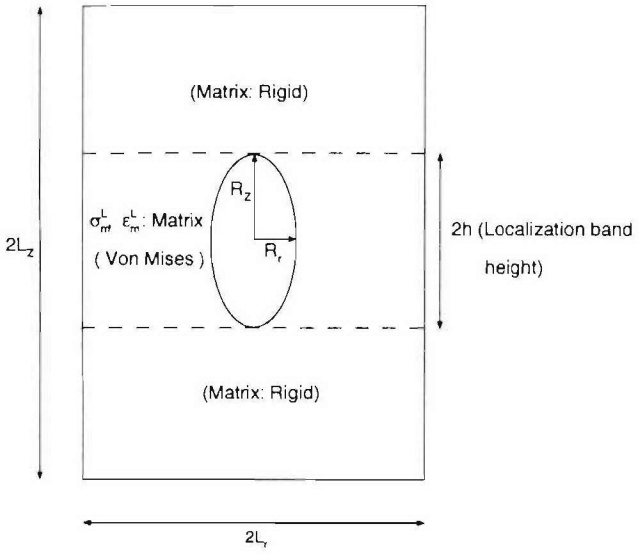

Figure 3.11: Geometry of the unit-cell after void coalescence.

where the function $H(\chi, W, \lambda, \gamma)$ is given by

$$H(\chi, W, \lambda, \gamma) = \frac{2}{3}\left(1 - \frac{\pi\chi^2}{12\gamma}\right)\frac{W\chi}{\lambda(1-\chi^2)C_F(\chi, W)}. \tag{3.70}$$

The magnitude of the macroscopic rate of deformation tensor $\mathbf{D}^p_{c_+}$ is related to the effective matrix deformation rate $\dot{\epsilon}^L_m$ by

$$D^p_{c_+} = \frac{2}{3}\left[\mathbf{D}^p_{c_+} : \mathbf{D}^p_{c_+}\right]^{1/2} = \dot{\epsilon}^L_m H(\chi, W, \lambda, \gamma). \tag{3.71}$$

The effective matrix deformation rate in the localized zone is used to compute the evolution of temperature, $\dot{\theta}^L_m$, in the localized zone using

$$\rho_m c_p \dot{\theta}^L_m = \beta \sigma^L_m \dot{\epsilon}^L_m. \tag{3.72}$$

Post-coalescence Evolution of the Inter-void Geometry

The evolution of the void spacing ratio λ is influenced by the current dispersion of voids, the anisotropy of the material and the imposed state of deformation. Prior

to the onset of coalescence, the variation in the spacing ratio can be computed approximately from the principal values of the stretch tensor $\mathbf{U}$, derived from the polar decomposition of the local deformation gradient $\mathbf{F} = \mathbf{RU}$. After the onset of void coalescence, the uniaxial straining mode of deformation leads to

$$\dot{\lambda} = \frac{\dot{L}_z}{L_r} = \frac{3}{2}\lambda D^p_{c+}. \tag{3.73}$$

The void ligament ratio χ is computed directly from Eqn. 3.46 prior to the onset of coalescence. During the post-coalescence regime, the evolution of the ligament ratio is determined by the plastic incompressibility constraint of the matrix material:

$$8{L_r}^2 L_z - \frac{2\pi}{3\gamma}{R_r}^2 R_z = constant. \tag{3.74}$$

Differentiating Eqn. 3.74 leads to

$$8{L_r}^2 \dot{L}_z - \frac{2\pi}{3\gamma}\{2R_r R_z \dot{R}_r + {R_r}^2 \dot{R}_z\} + \frac{2\pi}{3\gamma^2}{R_r}^2 R_z \dot{\gamma} = 0 \tag{3.75}$$

where we have explicitly allowed for variation in the shape parameter γ. From (3.75) and the kinematic constraints on the evolution of L_r, L_z and R_z, one can show that

$$\dot{\chi} = \frac{\dot{R}_r}{L_r} = \frac{3\gamma}{2}\frac{\lambda}{W}\left(\frac{6}{\pi\chi^2} - \frac{1}{2\gamma}\right)D^p_{c+} + \frac{\chi}{2\gamma}\dot{\gamma}. \tag{3.76}$$

In the current formulation, we neglect the evolution of the void shape prior to the onset of coalescence. This approximation is expected to be reasonable for nucleation-dominated ductile fracture at high stress triaxialities. During the post-coalescence period, the evolution of the void aspect ratio W is given by

$$\frac{\dot{W}}{W} = \frac{\dot{R}_z}{R_z} - \frac{\dot{R}_r}{R_r} \tag{3.77}$$

which can be reduced to

$$\dot{W} = \frac{3}{2}\frac{\lambda}{\chi}D^p_{c+} - \frac{W}{\chi}\dot{\chi}. \tag{3.78}$$

Experimentally, the void shape at complete failure ($\chi = 1$) shows considerable variation from the initially assumed spheroidal or ellipsoidal geometry. This effect can be captured by allowing for variation in the shape parameter γ in a manner similar to that for f^* in Eqn. 3.41:

$$\gamma_{c_-} = \gamma_0 \tag{3.79}$$

$$\gamma_{c_+} = \gamma_0 + \frac{\chi - \chi_c}{1 - \chi_c}(\gamma_f - \gamma_0) \tag{3.80}$$

where γ_0 the initial shape factor (=1/2) and γ_f is the final shape factor. Differentiating Eqn. 3.80 and substituting in Eqn. 3.76, we get

$$\dot{\chi} = \frac{\frac{3\gamma}{2}\frac{\lambda}{W}\left(\frac{6}{\pi\chi^2} - \frac{1}{2\gamma}\right)}{1 - \frac{\chi}{2\gamma}\left(\frac{\gamma_f - \gamma_0}{1-\chi_c}\right)} D^p_{c_+}. \tag{3.81}$$

Similarly, the evolution of the void aspect ratio can be obtained by substituting for $\dot{\chi}$ from Eqn. 3.81 to obtain

$$\dot{W} = \frac{\frac{9\lambda}{4\chi}\left(\frac{2}{3}(1+\frac{\gamma}{2}) - \frac{4\gamma}{\pi\chi^2}\right) - \frac{3\lambda}{4\gamma}\left(\frac{\gamma_f - \gamma_0}{1-\chi_c}\right)}{1 - \frac{\chi}{2\gamma}\left(\frac{\gamma_f - \gamma_0}{1-\chi_c}\right)} D^p_{c_+}. \tag{3.82}$$

Note that allowing for explicit variation in the shape factor γ has led to a considerable increase in the rate of evolution of the ligament ratio.

Transition from Pre-coalescence to a Post-coalescence Mode of Deformation

Consider the schematic of the GTN pre-coalescence flow potential Φ_{c_-} before the onset of coalescence and the post-coalescence flow potential Φ_{c_+} as shown in Figure 3.12. In a finite element formulation for the integration of post-coalescence behavior, numerical difficulties were encountered due to the abrupt transition ($\Phi_{c_-} \rightarrow \Phi_{c_+}$) in the normal to the flow potential. In order to successfully make the transition between

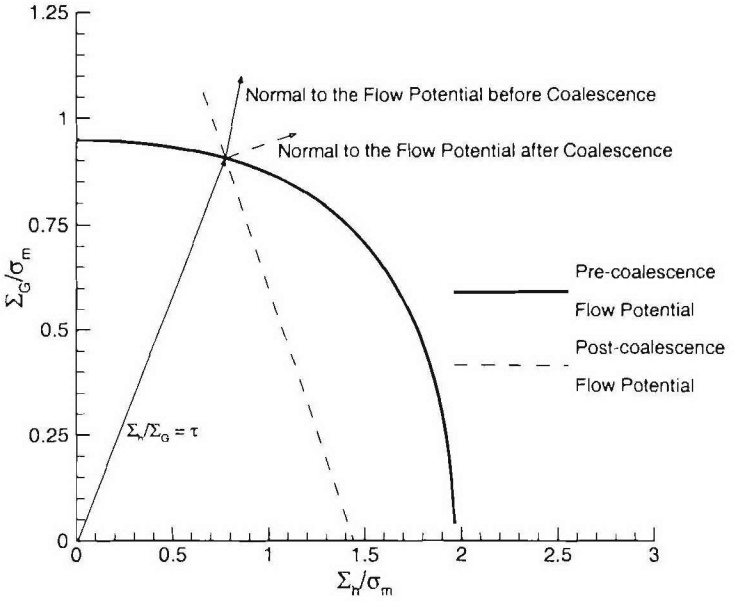

Figure 3.12: Transition from the pre-coalescence GTN potential to the post-coalescence flow potential Φ_{c_+}.

the two modes of deformation, we construct a modified flow potential $\tilde{\Phi}_{c_+}$ as follows

$$\tilde{\Phi}_{c_+} = \left(\frac{c_1 \Sigma_G + \frac{3}{2} c_2 \Sigma_h}{\sigma_m^L} \right)^2 - \frac{9}{4}(1-\chi^2)^2 C_F^2(\chi, W) = 0 \tag{3.83}$$

where c_1 and c_2 are functions of the ligament ratio χ. In particular, as $\chi \to \chi + \Delta\chi$, $c_1, c_2 \to 1$. The modification results in the transition from the diffuse mode of deformation to the localized mode predicted by Φ_{c_+} taking place over a finite interval of the ligament ratio $\Delta\chi$, rather than abruptly at $\chi = \chi_c$. Consider the normal to the viscoplastic GTN flow potential at the onset of void coalescence

$$\mathbf{D}^p_{c_-} = \Lambda_{c_-} \left[\frac{3}{\sigma_m^2} \boldsymbol{\Sigma}' + \frac{q_1 q_2 f}{\sigma_m} \sinh\left(\frac{3 q_2 \Sigma_h}{2\sigma_m} \right) \mathbf{I} \right]. \tag{3.84}$$

The normal to the modified flow potential $\tilde{\Phi}_{c_+}$ is given by

$$\tilde{\mathbf{D}}^p_{c_+} = \tilde{\Lambda}_{c_+} \left(\frac{\partial \tilde{\Phi}}{\partial \boldsymbol{\Sigma}} \right)_{c_+}. \tag{3.85}$$

The pre-factor $\tilde{\Lambda}_{c_+}$ is obtained by equating the macroscopic dissipation rate over the unit cell with the internal dissipation rate in the matrix as

$$V_c \boldsymbol{\Sigma} : \mathbf{D}^p_{c_+} = (\tilde{V}_p - V_v)\sigma^L_m \dot{\epsilon}^L_m. \tag{3.86}$$

During the transition from $\chi_c \rightarrow \chi_c + \Delta\chi$, we let the volume of the central porous layer vary smoothly as

$$\tilde{V}_p = V_c \left[(1-p) + \frac{R_z}{L_z} p \right] \tag{3.87}$$

where p is an interpolation parameter defined as

$$p = \frac{\chi - \chi_c}{\Delta\chi}. \tag{3.88}$$

In order to smooth the transition between the two flow potentials, we will let the orientation of the normal to $\tilde{\Phi}_{c_+}$ be the same as the orientation of the normal to the viscoplastic GTN flow potential at coalescence. This simplification leads to

$$\left.\frac{c_2}{c_1}\right|_{p=0} = \sinh\left(\frac{3q_2\Sigma_h}{2\sigma_m}\right)\frac{q_1 q_2 f \sigma_m}{\Sigma_G} = \hat{N}_c. \tag{3.89}$$

After the transition to the true post-coalescence mode, we let the constants c_1 and c_2 be unity, thereby recovering the original post-coalescence flow potential Φ_{c_+}. Using Eqn. 3.89, we define

$$\frac{c_2(\chi)}{c_1(\chi)} = \hat{N}_c(1-p) + p = \hat{N}. \tag{3.90}$$

We impose the additional constraint that the principal normal stress Σ_{zz} satisfies the plastic limit load criterion during the transition. This constraint leads to

$$c_1(\chi)\Sigma_G + \frac{3}{2}c_2(\chi)\Sigma_h = \Sigma_G + \frac{3}{2}\Sigma_h. \tag{3.91}$$

Using Eqns. 3.90 and 3.91, we can show that

$$c_1(\chi) = \frac{2+3\tau}{2+3\tau\hat{N}} \tag{3.92}$$

$$c_2(\chi) = \frac{2+3\tau}{2+3\tau\hat{N}}\hat{N} \tag{3.93}$$

where $\tau = \Sigma_h/\Sigma_G$ is the triaxiality ratio.

3.6 Numerical Implementation of the Fracture Model in ABAQUS/Explicit

The basis for the finite element implementation of the computational ductile fracture model is the dynamic principal of virtual work given by

$$\int_{B^*} \boldsymbol{\Sigma} : \delta\mathbf{D}\, dV + \int_{B^*} \rho \frac{\partial^2 \mathbf{u}}{\partial t^2} \cdot \delta\mathbf{u}\, dV = \int_{B^*} \rho\mathbf{b} \cdot \delta\mathbf{u}\, dV + \int_{\partial B^*_\Sigma} \mathbf{t} \cdot \delta\mathbf{u}\, ds. \tag{3.94}$$

Here, $\boldsymbol{\Sigma}$ and $\mathbf{D}$ are the macroscopic Cauchy stress and deformation rate tensor in the current configuration B^*, and $\mathbf{u}, \mathbf{b}, \mathbf{t}$ are the corresponding nodal displacement, body force and surface-traction distribution. The boundary conditions are specified as

$$\boldsymbol{\Sigma}\mathbf{n} = \mathbf{t} \ on \ \partial B^*_\Sigma \tag{3.95}$$

$$\mathbf{u} = \hat{\mathbf{u}} \ on \ \partial B^*_u \tag{3.96}$$

and the initial conditions are specified as

$$\mathbf{u}(t=0) = \mathbf{u}_0 \tag{3.97}$$

$$\dot{\mathbf{u}}(t=0) = \dot{\mathbf{u}}_0 \tag{3.98}$$

where $\mathbf{u}_0$ and $\dot{\mathbf{u}}_0$ are the prescribed initial displacement and velocity field, $\mathbf{n}$ is the normal to the boundary in the current configuration, and ∂B^*_Σ and ∂B^*_u are portions of the surface ∂B^* where the traction and displacement boundary conditions are specified. Using the finite element discrete approximation in Eqn. 3.94 for the nodal displacements $\mathbf{u}$, we get

$$\mathbf{M}\frac{\partial^2 \mathbf{U}}{\partial t^2} = \mathbf{F} \tag{3.99}$$

where $\mathbf{M}$ is the mass matrix, $\mathbf{U}$ is the vector of nodal displacements and $\mathbf{F}$ is the nodal force vector.

The finite element program ABAQUS/Explicit[1] was used to solve the governing system of equations with a user-implemented material model VUMAT. A user material routine for the porous elastic-viscoplastic finite deformation model described in previous sections was implemented because ABAQUS/Explicit supports only a very limited form of the Gurson-Tvergaard-Needleman model, for isotropic power-law hardening solids.

ABAQUS/Explicit uses an explicit central-difference technique for integrating the governing equations of motion as described by Eqn. 3.99. Let $\mathbf{U}^n$, $\mathbf{V}^n$ and $\mathbf{A}^n$ represent the vector of nodal displacements, velocities and accelerations at a time increment n. Assuming complete knowledge of the kinematic and material state at increment n, the kinematic state at increment $n+1$ is obtained from

$$\mathbf{V}^{(n+\frac{1}{2})} = \mathbf{V}^{(n-\frac{1}{2})} + \frac{\Delta t^{(n+1)} + \Delta t^{(n)}}{2}\mathbf{A}^n \tag{3.100}$$

$$\mathbf{U}^{(n+1)} = \mathbf{U}^{(n)} + \Delta t^{(n+1)}\mathbf{V}^{(n+\frac{1}{2})} \tag{3.101}$$

where the acceleration $\mathbf{A}^{(n)}$ at the beginning of increment n is obtained by inverting Eqn. 3.99 as

$$\mathbf{A}^{(n)} = \frac{\partial^2 \mathbf{U}^{(n)}}{\partial t^2} = \mathbf{M}^{-1}\mathbf{F}^{(n)}. \tag{3.102}$$

In the current formulation, we use a uniform time step $\Delta t^{(n)} = \Delta t^{(n+1)} = \Delta t$. The computational efficiency of the explicit dynamics procedure is facilitated by using a diagonal lumped-mass matrix $\mathbf{M}$ that enables Eqn. 3.102 to be solved without the use of matrix inversion. The material state at increment $n+1$ is updated in the user-material routine VUMAT using the current material and kinematic state at increment n and the updated kinematic state at time increment $n+1$. This procedure is described briefly in the following section.

[1]ABAQUS and ABAQUS/Explicit are registered trademarks of Hibbitt, Karlsson & Sorensen, Inc.

Material Update using VUMAT

The Cauchy stress state Σ_{ij} at time increment t_{n+1} is computed from the stress state at time t_n through

$$\Sigma_{ij}^{(n+1)} = \Sigma_{ij}^{(n)} + \Delta t \dot{\Sigma}_{ij}^{(n)} \tag{3.103}$$

where $\Delta t = t_{n+1} - t_n$. The convected derivative of the Cauchy stress, *i.e.*, $\dot{\boldsymbol{\Sigma}}$, is related to the corotational derivative (or the Jaumann rate) $\overset{\Delta}{\boldsymbol{\Sigma}}$, by

$$\dot{\boldsymbol{\Sigma}} = \overset{\Delta}{\boldsymbol{\Sigma}} + \boldsymbol{\Omega}^e \boldsymbol{\Sigma} - \boldsymbol{\Sigma} \boldsymbol{\Omega}^e. \tag{3.104}$$

The Jaumann rate of the macroscopic Cauchy stress can, from Eqn. 3.20, be expressed in terms of the rates of deformation by

$$\overset{\Delta}{\boldsymbol{\Sigma}} = \frac{1}{J} \mathcal{C}^e : [\mathbf{D} - \mathbf{D^e} - \mathbf{D^T}] - \frac{\dot{J}}{J} \boldsymbol{\Sigma}. \tag{3.105}$$

For the applications considered here, the stresses are much smaller than the elastic modulii. Consequently, we neglect the last term in Eqn. 3.105 and take the Jaumann rate of the Cauchy stress to be given by

$$\overset{\Delta}{\boldsymbol{\Sigma}} = \frac{1}{J} \mathcal{C}^e : [\mathbf{D} - \mathbf{D^p} - \mathbf{D^T}]. \tag{3.106}$$

In finite deformation problems, ABAQUS/Explicit passes on the Cauchy stress components to VUMAT on a corotational frame of reference. Therefore, the user is concerned with just the corotational rate of macroscopic Cauchy stress at each time increment. Integration of the corotational (or Jaumann) rate of the macroscopic Cauchy stress is carried out using the rate-tangent-modulus method of Peirce, Shih and Needleman (1984). A brief discussion of the rate-tangent-modulus method for isotropic, porous, elastic-viscoplastic materials is given in the following section. Further details of its implementation in ABAQUS/VUMAT are found in Appendix B and Appendix C.

Rate Tangent Modulus Method for Isotropic Elastic-Viscoplastic Solids

Prior to the onset of void coalescence, we represent the equivalent effective matrix strain rate $\dot{\epsilon}_m$ over the time interval (t_n, t_{n+1}) by and $n + 1$ as

$$\dot{\epsilon}_m = \dot{\epsilon}_m^{(n)}(1 - \Gamma) + \Gamma\dot{\epsilon}_m^{(n+1)} \tag{3.107}$$

where $\dot{\epsilon}_m^{(n)}$ and $\dot{\epsilon}_m^{(n+1)}$ are the effective matrix strain rates at the beginning and end of the time step and Γ is a parameter that can range from 0 to 1. At $\Gamma = 0$, the scheme reduces to the Euler integration rule and is characterized by extremely small time steps to ensure numerical stability. As Γ is increased, the stability of the method increases. The strain rate $\dot{\epsilon}_m^{(n+1)}$ at the end of the time step is given by a Taylor approximation as

$$\dot{\epsilon}_m^{(n+1)} = \dot{\epsilon}_m^{(n)} + \Delta t \left[\frac{\partial\dot{\epsilon}_m}{\partial\sigma_m}\dot{\sigma}_m + \frac{\partial\dot{\epsilon}_m}{\partial\epsilon_m}\dot{\epsilon}_m + \frac{\partial\dot{\epsilon}_m}{\partial\theta_m}\dot{\theta}_m\right]_{t=t_n} \tag{3.108}$$

where the derivatives are calculated at the beginning of the time increment n. Similarly, after the onset of void coalescence, we represent the equivalent effective local matrix strain rate $\dot{\epsilon}_m^L$ by

$$\dot{\epsilon}_m^L = \dot{\epsilon}_m^{L(n)}(1 - \Gamma) + \Gamma\dot{\epsilon}_m^{L(n+1)} \tag{3.109}$$

where $\dot{\epsilon}_m^{L(n)}$ and $\dot{\epsilon}_m^{L(n+1)}$ are the effective local matrix strain rates at the beginning and end of the time step. Using a Taylor approximation for $\dot{\epsilon}_m^{L(n+1)}$, we get

$$\dot{\epsilon}_m^{L(n+1)} = \dot{\epsilon}_m^{L(n)} + \Delta t \left[\frac{\partial\dot{\epsilon}_m^L}{\partial\sigma_m^L}\dot{\sigma}_m^L + \frac{\partial\dot{\epsilon}_m^L}{\partial\epsilon_m^L}\dot{\epsilon}_m^L + \frac{\partial\dot{\epsilon}_m^L}{\partial\theta_m^L}\dot{\theta}_m^L\right]_{t=t_n}. \tag{3.110}$$

Expressions for the rates of temperature change, θ_m and θ_m^L, are given in Eqns. 3.32 and 3.72, respectively. The evolution of the matrix effective stresses σ_m and σ_m^L are determined by the consistency condition for plastic flow. Prior to the onset of void

coalescence, this consistency condition for the potential $\Phi_{c_-}(\boldsymbol{\Sigma}, \sigma_m, f)$ can be written as

$$\dot{\Phi}_{c_-} = \frac{\partial \Phi}{\partial \boldsymbol{\Sigma}} :\overset{\Delta}{\boldsymbol{\Sigma}} + \frac{\partial \Phi}{\partial \sigma_m}\dot{\sigma}_m + \frac{\partial \Phi}{\partial f}\dot{f} = 0 \tag{3.111}$$

where Φ_{c_-} is given by Eqn. 3.39. After the onset of void coalescence, the plastic consistency condition for the potential $\Phi(\boldsymbol{\Sigma}, \sigma_m^L, \chi, W)$ is given by

$$\dot{\Phi}_{c_+} = \frac{\partial \Phi}{\partial \boldsymbol{\Sigma}} :\overset{\Delta}{\boldsymbol{\Sigma}} + \frac{\partial \Phi}{\partial \sigma_m^L}\dot{\sigma}_m^L + \frac{\partial \Phi}{\partial \chi}\dot{\chi} + \frac{\partial \Phi}{\partial W}\dot{W} = 0 \tag{3.112}$$

where Φ_{c_+} is given by Eqn. 3.65. As shown in Appendix B and Appendix C, the rate of evolution of the matrix stress can be computed from expressions having the form

$$\dot{\sigma}_m = \mu_b + \mu_a \dot{\epsilon}_m \tag{3.113}$$

$$\dot{\sigma}_m^L = \mu_b^L + \mu_a^L \dot{\epsilon}_m^L \tag{3.114}$$

where μ_b, μ_a, μ_b^* and μ_a^* are complex expressions. The equivalent matrix strain rates before and after coalescence can be computed by substituting Eqn. 3.108 into Eqn. 3.107 and Eqn. 3.110 into Eqn. 3.109 to obtain

$$\dot{\epsilon}_m = \frac{\dot{\epsilon}_m^{(n)} + \Gamma \frac{\partial \dot{\epsilon}_m}{\partial \sigma_m}_{t_n} \mu_b \Delta t}{1 - \Gamma \Delta t \left(\frac{\partial \dot{\epsilon}_m}{\partial \sigma_m}_{t_n} \mu_a + \frac{\partial \dot{\epsilon}_m}{\partial \sigma_m}_{t_n} + \frac{\partial \dot{\epsilon}_m}{\partial \sigma_m}_{t_n} \frac{\beta \sigma_m}{\rho c_p} \right)} \tag{3.115}$$

$$\dot{\epsilon}_m^L = \frac{\dot{\epsilon}_m^{L(n)} + \Gamma \frac{\partial \dot{\epsilon}_m^L}{\partial \sigma_m^L}_{t_n} \mu_b^L \Delta t}{1 - \Gamma \Delta t \left(\frac{\partial \dot{\epsilon}_m^L}{\partial \sigma_m^L}_{t_n} \mu_a^L + \frac{\partial \dot{\epsilon}_m^L}{\partial \sigma_m^L}_{t_n} + \frac{\partial \dot{\epsilon}_m^L}{\partial \sigma_m^L}_{t_n} \frac{\beta \sigma_m^L}{\rho c_p} \right)}. \tag{3.116}$$

Using the equivalent effective matrix strain rates, we can compute the plastic part of the rate of deformation tensor $\mathbf{D}^p$ and the contribution due to thermal straining $\mathbf{D}^T$. The material state at the end of the time increment is obtained by integrating the corotational derivative of the macroscopic Cauchy stress and updating the state variables : $\sigma_m, f, \chi, W, \lambda$ and γ.

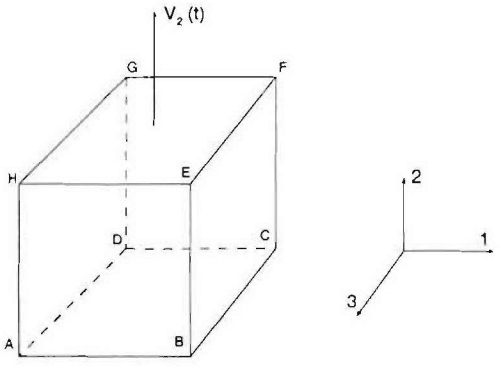

Figure 3.13: ABAQUS/VUMAT integration of the material model for 1 C3D8R Finite Element.

Simulation of ABAQUS/VUMAT

To gain understanding of the material model, the computational response of a single 8-noded C3D8R element loaded in uniaxial tension was evaluated in ABAQUS/Explicit. The size of the cubic element shown in Figure 3.13 was chosen to be $66\mu m$. Symmetry boundary conditions are imposed on faces ABCD, ADHG and DCFG as

$$u_2(t) = 0 \; on \; [ABCD] \tag{3.117}$$

$$u_3(t) = 0 \; on \; [DCFG] \tag{3.118}$$

$$u_1(t) = 0 \; on \; [ADGH]. \tag{3.119}$$

The velocity boundary conditions on face EFGH is given by

$$V_2(t) = \begin{cases} V_0 t/t_r & \text{if } t \leq t_r \\ V_0 & \text{if } t > t_r \end{cases} \tag{3.120}$$

where the rise time t_r is $50\mu s$ and the steady state velocity V_0 is $0.05m/s$. The two remaining faces ABEH and BCFE are allowed to be traction free. The internal state

variables used in the material model are initialized as

$$\sigma_{m,t=0} = 0 \tag{3.121}$$

$$f_{t=0} = 1.0 \times 10^{-6} \tag{3.122}$$

$$\lambda_{t=0} = 1.0 \tag{3.123}$$

$$W_{t=0} = 1.0 \tag{3.124}$$

$$\gamma_{t=0} = 0.5 \tag{3.125}$$

$$\chi_{t=0} = \left(\frac{6f}{\pi}\right)^{1/3}_{t=0}. \tag{3.126}$$

The strain-hardening response of the matrix material is assumed to be given by the constitutive model for AL6XN as developed earlier. A list of material parameters governing the hardening of the matrix is given in Table 3.1. The GTN flow potential (Eqn. 3.39) is used to model the macroscopic flow response prior to void coalescence and the Thomason upper-bound criterion (Eqn. 3.65) is used to simulate the micromechanics of post-coalescence. Additional model parameters relevant for integration of the macroscopic flow response and evolution of the state variables are given in Table 3.3.

The integration of the kinematic state in the explicit dynamics algorithm imposes an upper limit on the stable time step that can be employed. This condition is satisfied by using a time step that satisfies the Courant-Friedrichs-Levy condition, ($\frac{c_1 \Delta t}{h} < 1$) where c_1 is the elastic longitudinal wave speed and h us the size of the element. However, the integration of the material state imposes an even more stringent requirement on the magnitude of the overall time step. For the mesh size of $66\mu m$, a time step of $1 \times 10^{-9} s$ was used in the rate-tangent-modulus integration routine. During the post-coalescence stage, the localized matrix deformation rates tend to be extremely high compared to the macroscopic extensional strain rates. In particular, the magnitude of the overall time step is determined by the need to ensure a stable

Model Parameter	Description	AL6XN Stainless Steel
f_N^{ϵ}	Strain controlled nucleation	0.088
ϵ_c	Nucleation strain: mean	0.425
s_N^{ϵ}	Nucleation strain: Eqn. 3.30	0.225
N_σ	Stress controlled nucleation	0.0
γ_0	Initial shape factor	0.50
γ_f	Final shape factor	0.75
χ_f	Final ligament ratio	0.995
$\dot{\epsilon}_m^R$	Limiting strain rate	2.5×10^5 /sec
q_1	Tvergaard parameter	1.50
q_2	Tvergaard parameter	1.00
F	Eqn. 3.58	0.1
G	Eqn. 3.58	1.2
Γ	Tangent modulus interpolation	0.75

Table 3.3: Model parameters for integration of user-material subroutine VUMAT.

and accurate integration of the constitutive equations at these high strain rates.

Results from integration of the macroscopic flow response in ABAQUS/VUMAT are shown in Figure 3.14. The evolution of the internal state variables $f, \chi, W, \lambda, \gamma$ are shown in Figure 3.15. The evolution of the macroscopic Cauchy stress Σ_G is similar to that of the matrix effective stress until effects of void growth and nucleation become important around $\epsilon_m \approx 0.2$. The onset of void coalescence leads to rapid unloading and the element is unloaded ($\Sigma_{22} < 50MPa$) when the final ligament ratio (≈ 0.975) is reached. After the final ligament ratio is reached, the stress in the element is unloaded elastically over the next few time increments. An interesting result that emerges in the simulation of the post-coalescence phase is that the stress drop remains linear almost until the final ligament ratio is reached. This behavior has also been observed in finite element simulations of void cells by Pardoen and Hutchinson (2000) and Tvergaard (1997).

The transition to the post-coalescence mode of behavior takes place when the principal macroscopic normal stress (Σ_{22} in this case) reaches the plastic limit-load

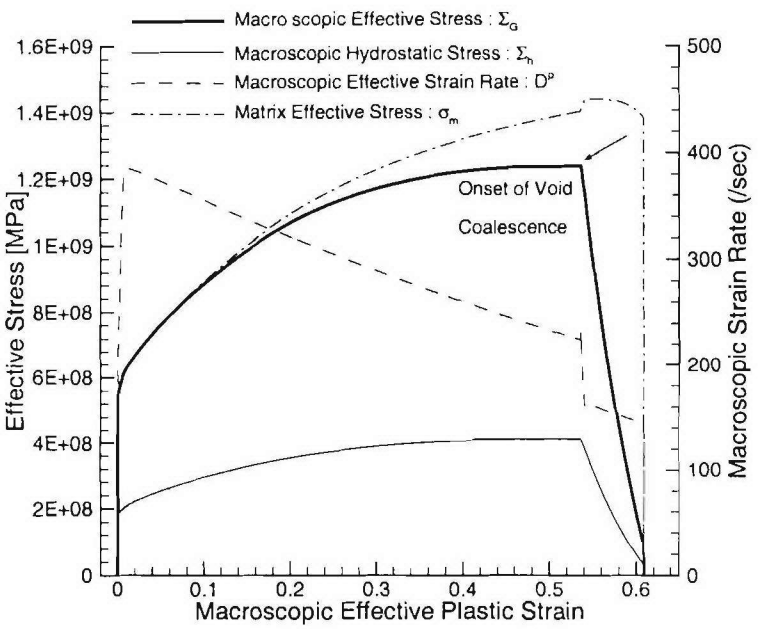

Figure 3.14: ABAQUS/VUMAT integration for 1 C3D8R element: Macroscopic flow stress.

for the current inter-void geometry and matrix effective stress. The rapid change in macroscopic and matrix deformation rates at the onset of void-coalescence is successfully handled through the use of the flow potential $\tilde{\Phi}_{c_+}$. In the post-coalescence regime, the user-material routine checks for de-activation of the plastic limit-state in the inter-void ligament at each time increment. While in most instances, elements unload to complete failure after undergoing transition to a post-coalescence mode, some elements that are not on the primary plane of crack propagation tend to become de-activated due to elastic unloading before the final ligament ratio is reached.

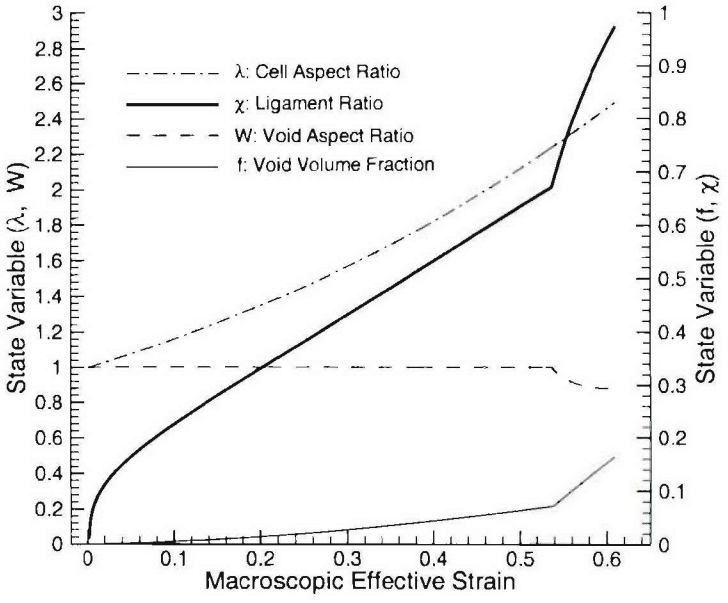

Figure 3.15: ABAQUS/VUMAT integration for 1 C3D8R element: Evolution of internal state variables.

3.7 Summary

A computational model for ductile fracture based on the micromechanics of void nucleation, growth and coalescence has been developed in this chapter. The response of the material at the macroscopic length scale has been related to the microstructural response through a set of internal state variables: matrix effective stress, ligament ratio, void spacing ratio, void aspect ratio and void shape factor. The evolution of the macroscopic material response and the internal state variables have been derived for two distinctive flow regimes: pre-coalescence and post-coalescence. The transition from pre-coalescence to post-coalescence has been analyzed using an upper-bound model to obtain the limit-loads needed to sustain a localized mode of plastic flow in the inter-void ligament. The computational material model for ductile fracture has been implemented as a user material routine VUMAT in ABAQUS/Explicit within a

framework for modeling the finite deformation of porous, elastic-viscoplastic materials. In Chapter 4, the above material model will be used to simulate the high strain rate deformation and fracture experiments on AL6XN-IN625 weldments.

Chapter 4

A Finite Element Study of Ductile Fracture in AL6XN-IN625 Weldments

4.1 Introduction

Results from an experimental investigation of the high-strain-rate flow and fracture of stainless steel welds were presented in Chapter 2. Based on these observations, a constitutive model for dynamic ductile fracture in a porous, elastic-viscoplastic material was developed in Chapter 3. A user material routine VUMAT was implemented in ABAQUS/Explicit to integrate the material response under high-strain-rate loading conditions. A finite element study of ductile fracture in AL6XN stainless steel welds is presented here. In this study, fully three-dimensional simulations of the high-strain-rate tension experiments (§2.3) and the quasi-static experiments on notched cylindrical specimens (§2.5) were conducted. These simulations were carried out on finite element models of the tensile specimen together with the appropriate initial

and boundary conditions imposed during the test. For the high-strain-rate experiments described in §2.3, the simulated FE results are compared with the recorded load-displacement response of the test specimen. For the quasistatic experiments on notched cylindrical tensile specimens, the distribution of void clusters are compared with corresponding observations obtained using X-ray Computed Microtomography (XCMT).

We begin with a study of the sensitivity of finite element simulations of ductile fracture to progressive refinements in mesh size. Ductile fracture in metallic alloys involves an interplay of a rich array of microstructural length scales (inclusion shape and radius, void spacing and distribution) and it is important to understand their relative effects. A material characteristic length is then identified for use in numerical simulations of ductile fracture of AL6XN weldments. Finite element models of tensile test specimens are then constructed on the basis of this characteristic length scale.

4.2 Mesh Sensitivity of Ductile Fracture Simulations

Numerical simulations of the evolution of ductile damage through void nucleation, growth and coalescence are known to be mesh sensitive (Needleman and Tvergaard 1994) due to localization of plastic flow. Therefore, finite element simulations of ductile fracture have to include the mesh size either explicitly as a material parameter or be based on a non-local formulation (Pijaudier-Cabot and Bazant (1987), Leblond, Perrin and Devaux (1994), Tvergaard and Needleman (1997)) in which a length scale is incorporated n the constitutive formulation. In the following section, we present the results of a study to understand the mesh dependence of ductile fracture simulations of AL6XN/Inconel-625 welds.

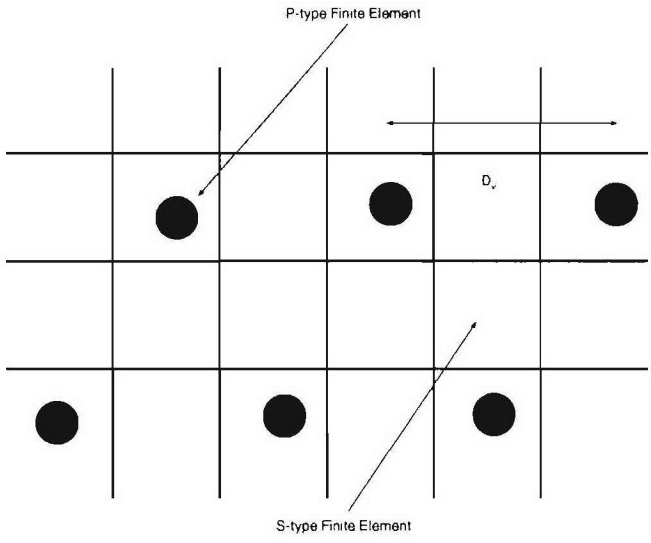

Figure 4.1: P and S-type finite elements used in ductile fracture simulations.

A study of the ductile fracture surfaces of the base stainless steel and the weld superalloy reveals the presence of a dual-size population of voids. The fracture surface is dominated by the presence of a few large voids interspersed with void sheets containing a profusion of small-scale voids. We define the primary nucleation centers as the sites where large voids are nucleated during the fracture evolution. Similarly, we define the secondary nucleation centers as the sites where the smaller-scale voids are nucleated. While, the distribution of the primary nucleation sites can be characterized by a length scale, the finely dispersed secondary nucleation centers are too closely spaced to be represented explicitly for any reasonably-sized finite element calculation.

Consider a finite element representation of the material microstructure as shown in Figure 4.1. The P-type finite elements are characterized by the presence of a primary nucleation site and the S-type finite elements are characterized by the presence of secondary nucleation sites. While the constitutive description of strain hardening, void growth and coalescence in both P and S elements are identical, the void

nucleation rules are determined by their respective nucleation site distribution. In view of the observed ductility, let us assume that the strain-controlled mode of void nucleation is the dominant mechanism in both P and S elements. Then, the rate of void nucleation is given by Eqn. 3.30 as

$$\dot{f} = N_\epsilon \dot{\epsilon}_m \tag{4.1}$$

$$N_\epsilon = \frac{f_N^\epsilon}{s_N^\epsilon \sqrt{2\pi}} \exp\left[-\frac{1}{2}\left(\frac{\bar{\epsilon}_m - \epsilon_c}{s_N^\epsilon}\right)^2\right]. \tag{4.2}$$

Typically, small-scale nucleation in an S-element takes place after primary nucleation in the surrounding P-elements. Therefore, the mean nucleation strain ϵ_c for S-elements is much larger than for a P-element. In addition, the amplitude of the void-nucleation parameter f_N^ϵ, for a P-element depends on the finite element mesh size h through

$$f_N^\epsilon(P) = f_0 \left[\frac{D_v}{h}\right]^3 \tag{4.3}$$

where f_0 is a constant and D_v is the average spacing between primary nucleation sites, as shown in Figure 4.1. In contrast, the void nucleation parameter for an S-element is assumed to be independent of the mesh size due to the much smaller scale of the dispersion of secondary nucleation centers. In addition to these P and S-type finite elements, E-type elements, which are modeled as being purely elastic, are used at locations sufficiently far from the plastically deforming zone.

In order to evaluate the mesh dependence of ductile fracture simulations, a sequence of finite element simulations was carried out on a flat-notched tensile specimen at various mesh refinements. A layout of the high-strain-rate tensile specimen (excluding symmetries) is shown in Figure 4.2. The specimen is loaded on face AJFB with a velocity ramp in the negative X1 direction. Symmetry boundary conditions are imposed on faces JIHGF ($U_2 = 0$), DEIH ($U_1 = 0$) and AJIE ($U_3 = 0$) respectively. The remaining faces of the specimen (BFCG, AEDCB and DHGC) are assumed to be

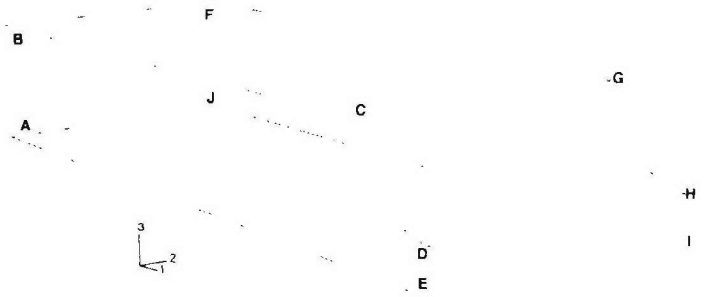

Figure 4.2: High-strain-rate notched tensile specimen.

traction free over the duration of the loading pulse. The velocity boundary condition on face AJFB is specified as

$$V_1(t) = \begin{cases} V_0 t/t_r & \text{if } t \leq t_r \\ V_0 & \text{if } t > t_r \end{cases} \tag{4.4}$$

where t_r is $20\mu s$ and the steady state velocity V_0 is $2.5m/s$. In all instances, the magnitude and duration of the loading pulse was sufficient to initiate dynamic fracture at the root of the notch. A finite element simulation of the behavior of the notched tensile specimen using the weld constitutive model was carried out on 4 different mesh configurations near the root of the notch as shown in Figures 4.3-4.6. The void nucleation parameters employed in this set of calculations are those that were used subsequently to model the load-displacement data from Kolsky Bar experiments. The complete set of void-nucleation parameters used to model the response of the base stainless steel and the weld material is shown in Table 4.1.

The division of the fracture process zone into P and S-type finite elements is also shown in Figures 4.3-4.6. In the coarsest discretization employed, every element near the root of the notch in Fig. 4.3 is a P-type element. (There are no S-type elements in Fig. 4.3) In contrast, only one out of 64 elements near the root of the notch

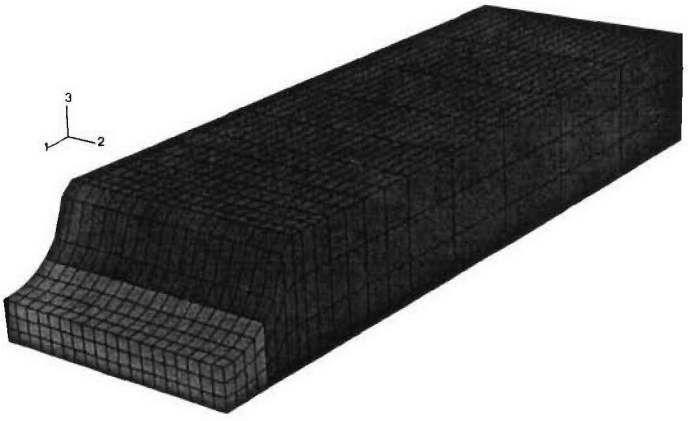

Figure 4.3: Finite element discretization and location of primary nucleation centers for $h = D_v = 132\mu m$.

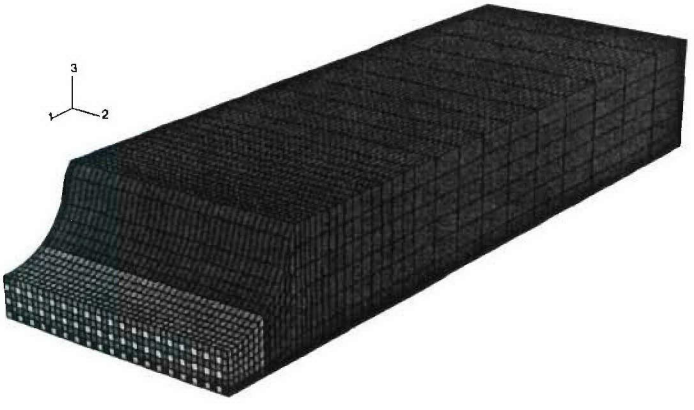

Figure 4.4: Finite element discretization and location of primary nucleation centers for $h = 0.5D_v = 66\mu m$.

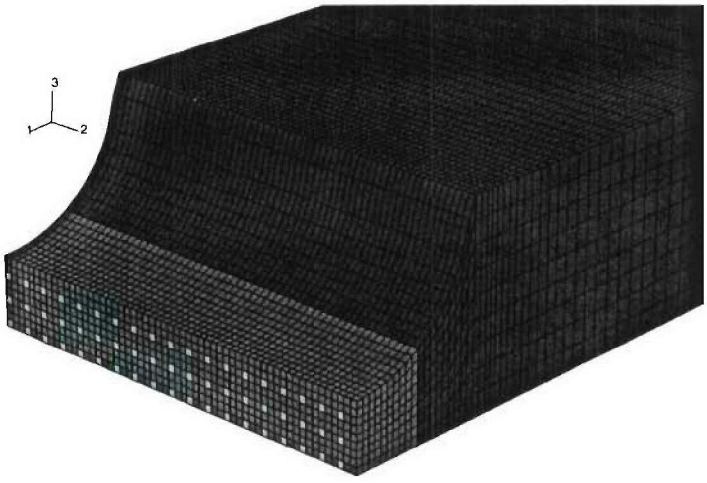

Figure 4.5: Finite element discretization and location of primary nucleation centers for $h = 0.33D_v = 44\mu m$.

Figure 4.6: Finite element discretization and location of primary nucleation centers. $h = 0.25D_v = 33\mu m$.

Parameter	Element	AL6XN	Inconel-625
ϵ_c	P	0.42	0.27
s_N^ϵ	P	0.22	0.10
f_0	P	0.011	0.011
ϵ_c	S	0.67	0.50
s_N^ϵ	S	0.20	0.10
f_0	S	0.0015	0.0015

Table 4.1: Void nucleation parameters for AL6XN and Inconel-625 alloys.

in Fig. 4.6 are P-type elements and the remaining 63 are S-type finite elements. Load-displacement data was extracted from the computed stress distribution and the applied velocity boundary conditions. Results from such an analysis for each of the 4 finite element models are shown in Figure 4.7. As expected, the early elastic response of the tensile specimen is virtually identical in all 4 finite element models. In addition, the early stages of the plastic response (which is dominated by the strain hardening of the matrix) is very similar across all mesh densities. The onset of void coalescence (Eqn. 3.58) in the primary P-type elements is earliest in the finest mesh ($h = 33\mu m$) at $130\mu m$ and latest in the coarsest mesh ($h = 132\mu m$) at $284\mu m$. Even though the onset of coalescence in the P-elements varies widely across the 4 mesh densities employed, the overall load-displacement behavior is quite similar until the onset of coalescence in the S-type finite elements. As the mesh size is reduced below $h = 66\mu m$, the failure response indicated by the falling load-displacement curve becomes relatively insensitive to mesh size.

For the reduced-integration C3D8R elements used in our simulations, we also studied the effect of hourglass control in ABAQUS/Explicit. For the finite element model with $h = 66\mu m$, the load-displacement response was nominally identical to that obtained in a simulation where the default hourglass parameter was increased by 50%. Slight differences ($< 2\%$) were observed in the ligament ratio only within the heavily deformed S-elements in the failure plane. Therefore, the default hourglass

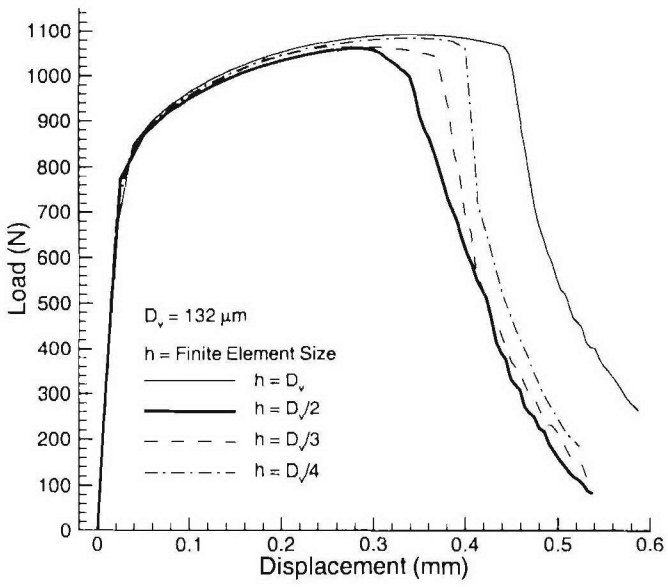

Figure 4.7: Mesh sensitivity of finite element dynamic fracture simulations.

control for C3D8R elements in ABAQUS/Explicit does not influence the localization events (onset of void coalescence and width of flow localization) near the failure plane.

4.3 *Finite Element Simulation of Dynamic Fracture Tests in a Kolsky Bar*

Detailed finite element simulations were carried out to model experimental observations on the high-strain-rate constitutive and fracture behavior of welded stainless steel plates. The finite element model was constructed using eight-noded C3D8R elements in ABAQUS/Explicit. The regions where material behavior is expected to be dominated by void nucleation and growth are modeled using P and S-type finite elements with $h \approx 66\mu m$. The porous elastic-viscoplastic constitutive model with void nucleation, growth and coalescence is used to describe the material behavior of

these P and S-type elements. In order to achieve computational efficiency, elements sufficiently far away from the plastically deforming zone are modeled as being purely elastic. These finite elements, called E-type elements, are typically not constrained by as stringent requirements on their mesh size as are those within the plastically deforming zone of the material. In addition, all elements are also identified as belonging to either the base, weld or heat-affected zones. Therefore, the overall finite element model for a typical heterogeneous specimen machined from the heat-affected zone consists of nine different types of finite elements: PE, PP, PS, WE, WP, WS, HE, HP and HS. Here PE, PP and PS are the base E, P and S-type finite elements, WE, WP and WS are the weld E, P and S-type finite elements and, HE, HP and HS are the E, P and S-type finite elements from the heat-affected zone.

The strain hardening behavior of the PP, PS, WP and WS elements are modeled based on the constitutive model developed earlier for AL6XN stainless steel and Inconel-625 superalloy. Based on observations from Kolsky bar experiments in compression on specimens machined from near the base/weld interface, the strain hardening of the HAZ (HP and HS elements) is taken to be overmatched by 5% with respect to the base material. As noted in Chapter 2, the weld material is clearly undermatched with respect to the base material. Table 3.1 and 3.2 list the elastic, thermal and strain hardening model parameters used in finite element simulations of base and weld material specimens.

Table 4.2 shows a list of fracture experiments for which fully 3-dimensional finite element calculations of ductile fracture are presented. Test specimens T041201C and T032001F are notched tensile test specimens machined entirely from the base material. Similarly, T051401E is a notched weld specimen machined from the weld material. T051401C and S3 are notched tensile test specimens machined such that the notch is located near the base/weld interface zone.

Test	Material	Description of Test
T041201C	AL6XN (P)	High Strain-Rate Kolsky Bar Test
T032001F	AL6XN (P)	High Strain-Rate Kolsky Bar Test
T051401E	Inconel-625 (W)	High Strain-Rate Kolsky Bar Test
T051401C	AL6XN/IN-625 (P/W Interface)	High-Strain Rate Kolsky Bar Test
S3	AL6XN/IN-625 (P/W Interface)	Quasi-static Loading in Instron.

Table 4.2: Summary of finite element simulations of ductile fracture experiments conducted on AL6XN/IN-625 welded plate.

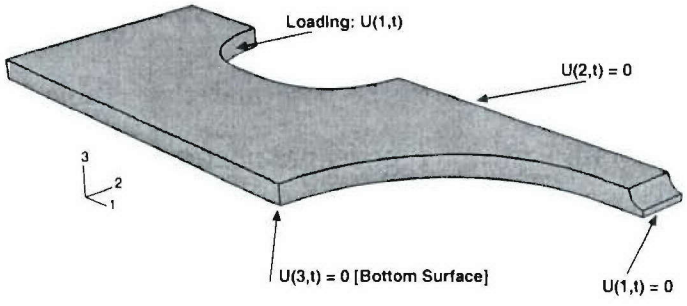

Figure 4.8: Finite element model of the Kolsky bar notched tensile specimens T041201C and T051401E.

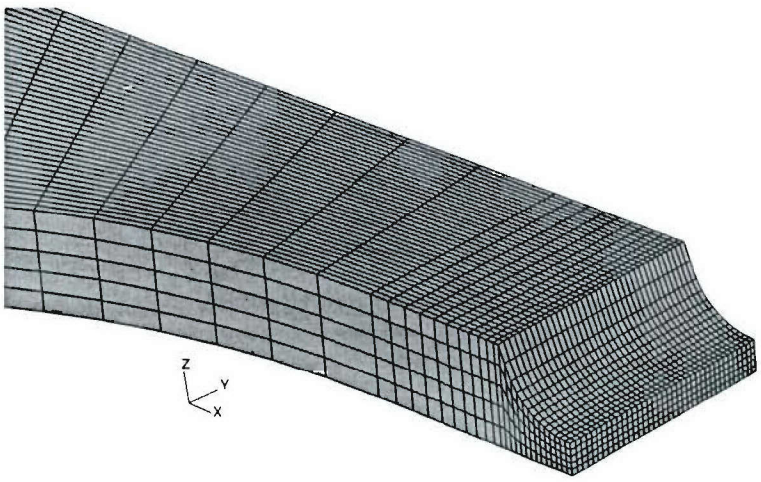

Figure 4.9: Finite element mesh near the notch of the Kolsky bar tensile specimens T041201C and T051401E. $h = 66\mu m$. Directions X, Y and Z correspond to the rolling, weld and transverse directions respectively.

Figure 4.8 shows one-eighth of the notched tensile specimen (Fig. 2.16) machined from the base material zone. The finite element model of the tensile specimen is 38.10 mm along the X-axis, 2.54 mm along the Y-axis at the root of the notch and 1.15 mm in thickness along the Z-axis. The radius of the notch and its depth are both equal to 0.79 mm. Symmetry boundary conditions are applied on three surfaces of the finite element model as shown in Fig. 4.8. Details of the finite element mesh used to model the notch are shown in Figure. 4.8. The FE model consists entirely of PP and PS elements near the notch and PE elements far away from it. The full mesh consists of 8,580 eight-noded C3D8R elements with a total of 32,706 degrees of freedom. In order to minimize sensitivity of the results to the discretization, the elements near the root of the notch are designed to have a side length $h \approx 66\mu m$. Therefore, the number of PP and PS elements in the plastically deforming zone of the test specimen is entirely determined by this microstructural length scale.

Figure 4.10 shows the experimental strain-time record obtained at the location of the strain gage stations on the incident and transmitter bars. The incident, reflected

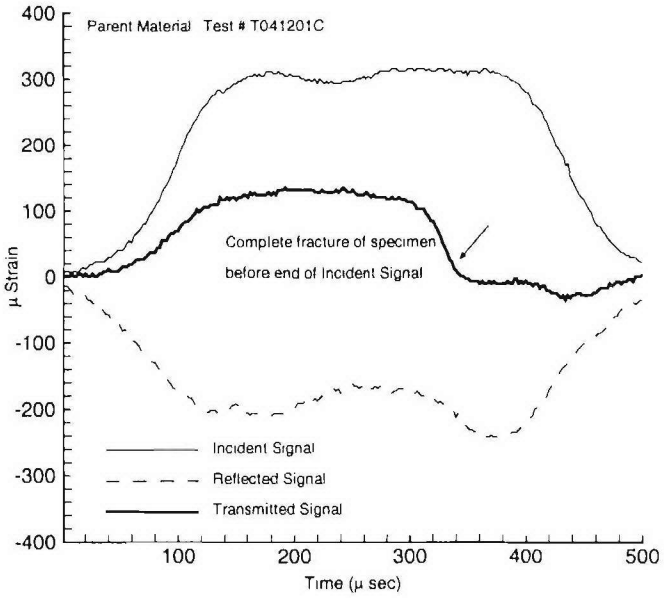

Figure 4.10: Experimental strain-time record of Kolsky bar test T041201C conducted on base AL6XN stainless steel.

and transmitted signals have all been superimposed on the same time scale to allow for easy comparison. The strain-time record at the gage stations was propagated to the specimen/bar interfaces using the Pochhammer-Chree dispersion relation as described in Appendix A. The dynamic load-displacement relationship obtained from the reconstructed strain-time pulse at the specimen/bar interfaces is shown in Figure 4.11. The tensile specimen undergoes a complete loss of stress-carrying capacity after $\approx 336\mu sec$. Note that the unloading of the specimen (and the transmitted signal) takes place well before the unloading of the incident pulse.

The velocity boundary conditions on the specimen/bar interfaces were obtained using the relations described in §2.3. The duration of the loading pulse in the simulation was chosen to be $336\mu sec$ to allow for complete loss of stress-carrying capacity (or failure) of the tensile test specimen. The time step chosen for integration was determined by the need for accurate integration of the matrix response in the PP and

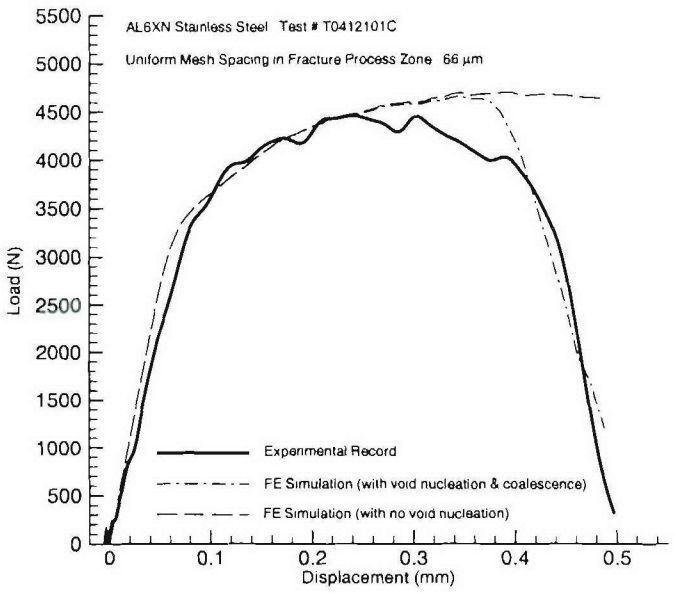

Figure 4.11: Finite element simulation of Kolsky bar fracture test T041201C.

PS elements after the onset of void coalescence. The time step chosen for integration was $2 \times 10^{-9} sec$ and is much less than the stability limit imposed by the CFL condition ($\Delta t_{CFL} \approx 13 \times 10^{-9} sec$). Results of a finite element simulation of the ductile fracture process in Test T041201C is shown in Figure 4.11. Results from a simulation of the response of the tensile specimen in the absence of damage evolution are also shown in Figure 4.11. In the absence of void nucleation, the FE simulation provides an accurate prediction of the load-displacement response only over the first $190 \mu sec$ (corresponding to $\approx 240 \mu m$). If void nucleation is specified to occur as in Table 4.1, the FE simulation compares quite well with the experimental record. Note that the Kolsky bar experiments provide an accurate measure of the overall load-displacement response of the specimen even after the onset of void coalescence or crack propagation in a portion of the specimen. These are inherently dynamic events and the measured elastic wave propagation record provides an essential tool for investigating the onset

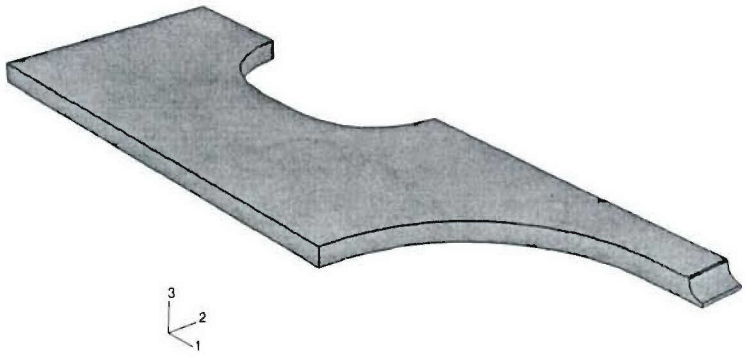

Figure 4.12: Finite element model of the Kolsky bar notched tensile specimen T032001F. Directions 1, 2 and 3 correspond to the rolling, weld and transverse directions respectively.

of coalescence and the extent of post-coalescence deformation in the specimen. The dual element description (PP and PS) was also found to be essential in describing the unloading response.

An additional set of fracture experiments were carried out on tensile specimens from the base material with a different notch profile. Figure 4.12 shows the finite element model for test specimen T032001F. The finite element model of the tensile specimen is 38.10 mm along the X-axis, 2.55 mm along the Y-axis at the root of the notch and 1.05 mm in thickness along the Z-axis. The radius of the notch and its depth are both equal 0.84 mm. The mesh consists of 6864 elements with a total of 27255 degrees of freedom. Details of the finite element mesh near the root of the notch are shown in Figure 4.13. The experimental strain-time record obtained at the gage stations for test specimen T032001F is shown in Figure 4.14. Even though the magnitude of the incident pulse is quite similar to that of T041201C, the magnitude of the transmitted pulse and the duration over which the specimen is intact are quite different. Complete of loss of stress carrying capacity is evident after $\approx 200\mu sec$. In

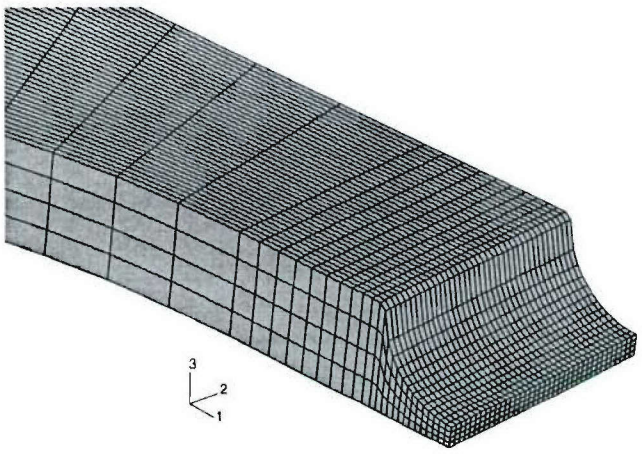

Figure 4.13: Finite element mesh near the notch of the Kolsky bar tensile specimen T032001F. $h = 66\mu m$.

addition, the strain rates at the root of notch in T032001F are much higher than in T041201C.

A finite element simulation of the Kolsky bar fracture test T032001F is shown in Figure 4.15. For comparison, results from a FE simulation of the tensile test in the absence of void nucleation is also shown in Figure 4.15. Notice the rapid loss in stress-carrying capacity after a net displacement of 0.24 mm and the reduced ductility of the tensile specimen. The experimental record shows oscillations that are not observed in the FE simulations. These oscillations are believed to be related mainly to the lower signal-to-noise ratio evident in the transmitted signal (see Figure 4.14). The finite element results are however, quite successful in predicting the overall response of the stainless steel tensile specimen.

A similar set of finite element simulations was carried out on notched tensile specimens machined from the weld Inconel-625 superalloy. Figure 4.16 shows a record of the strain-time pulse obtained at the gage stations for Test T051401E. The design of the tensile specimen and the finite element model was identical to the base tensile

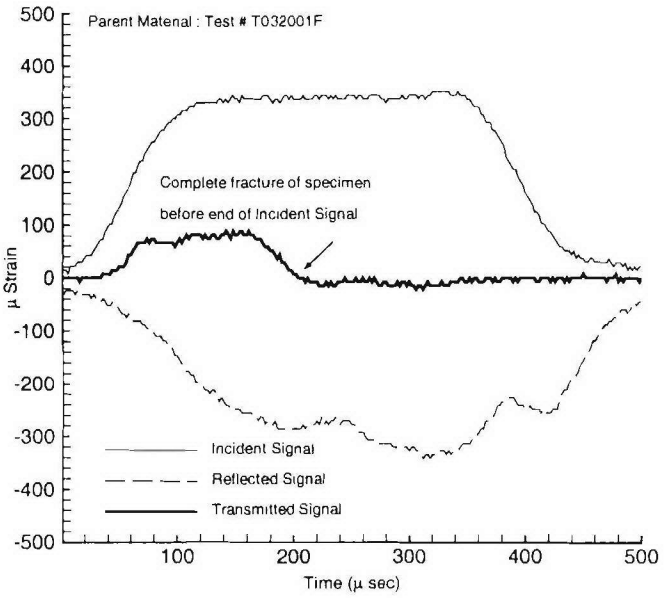

Figure 4.14: Experimental strain-time record of Kolsky bar test T032001F conducted on base AL6XN stainless steel.

specimen T041201C. The tensile specimen was machined from the welded stainless steel plate such that the orientation of the loading was along the rolling direction. Even though portions of the tensile specimen T051401E are located within the base material, the plastically deforming zone and the region immediately adjacent to it are entirely within the weld zone. Therefore, the overall response of T051401E is determined by the plastic response of the weld material along with the elastic constraint imposed by the outside base material. The finite element model of T051401E consists of 8580 C3D8R elements with WP and WS elements near the root of the notch and WE/PE elements outside the zone of plastic deformation.

Results from a finite element simulation of the Kolsky bar fracture test T051401E are shown in Figure 4.17. The duration of the loading pulse before complete loss of stress-carrying capacity is $\approx 232\mu sec$. A $2ns$ time step is used to integrate the response of the material. The results from the FE simulations closely approximate the

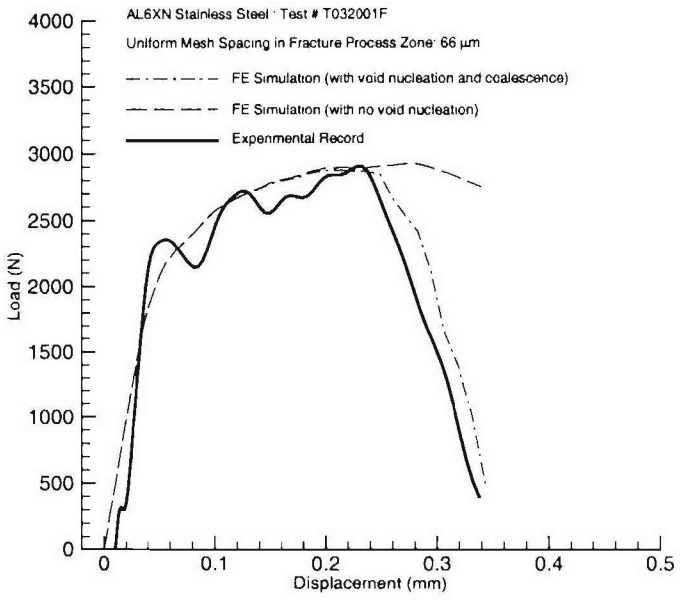

Figure 4.15: Finite element simulation of Kolsky bar fracture test T032001F.

measured load-displacement response. Near the initial knee in the load-displacement response, the FE results show a more gradual transition compared to the sharp change in slope seen in the experimental record. This discrepancy could be related mainly to the lack of reliable data for modeling in the low-strain regime ($< 5\%$) at high strain rates.

Figure 4.18 shows a finite element model for tensile test specimen T051401C. The tensile test specimen was machined from the welded plate such that the orientation of the loading was along the rolling direction. Unlike the weld specimen T051401E, the notch is located such that it is near the heat-affected base/weld interface zone. Due to the lack of symmetry in the tensile specimen, the finite element model for T051401C is much larger than that for homogeneous test samples. The overall model consists of 34320 eight-noded C3D8R elements with a total of 130824 degrees of freedom. Due to the heterogeneous nature of the specimen, the finite element model consists

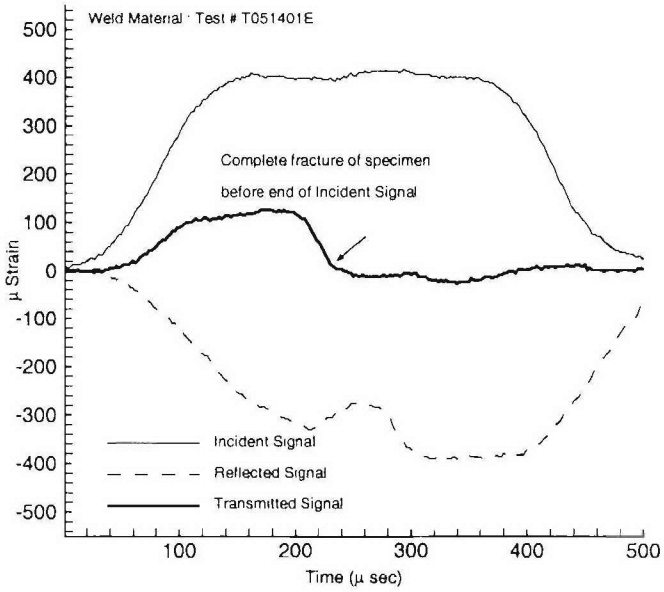

Figure 4.16: Experimental strain-time record of Kolsky bar test T051401E conducted on weld Inconel-625 superalloy.

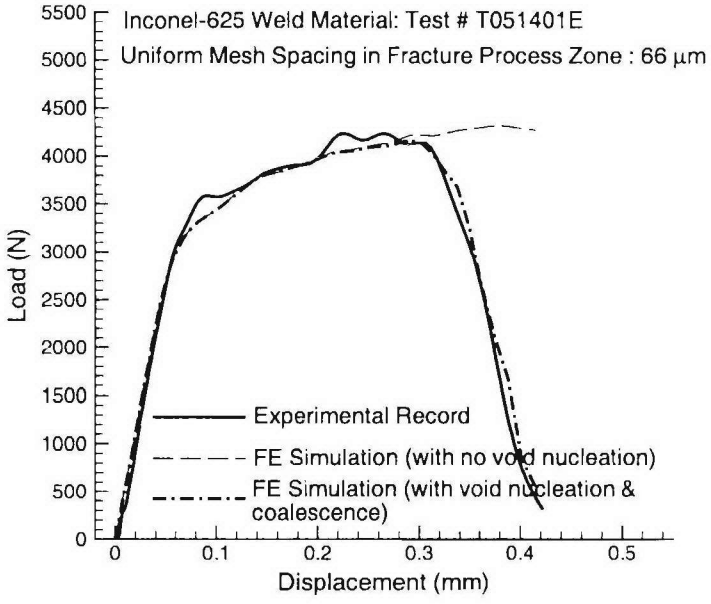

Figure 4.17: Finite element simulation of Kolsky bar fracture test T051401E.

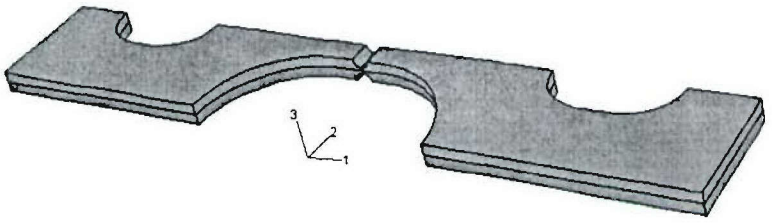

Figure 4.18: Finite element model of a Kolsky bar notched tensile specimen with a base/weld interface zone. Directions 1, 2 and 3 correspond to the rolling, weld and transverse directions respectively.

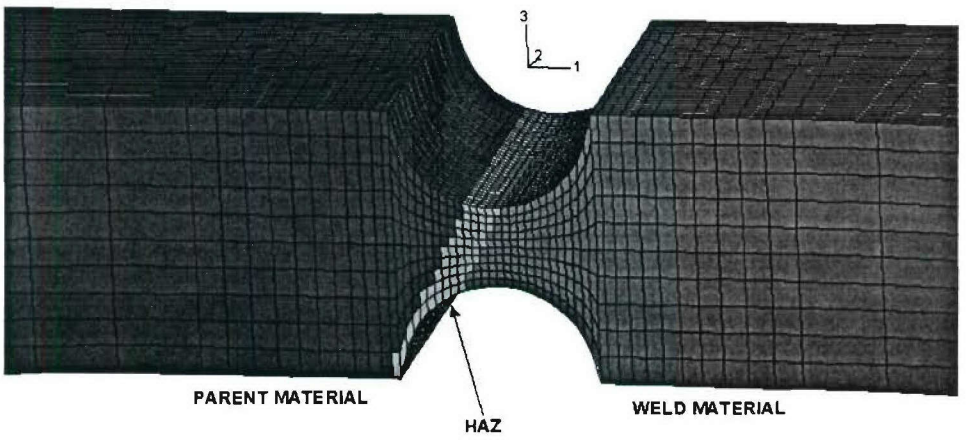

Figure 4.19: Finite element mesh near the notch of the Kolsky bar tensile specimen T051401C with a base/weld interface zone. $h = 66\mu m$.

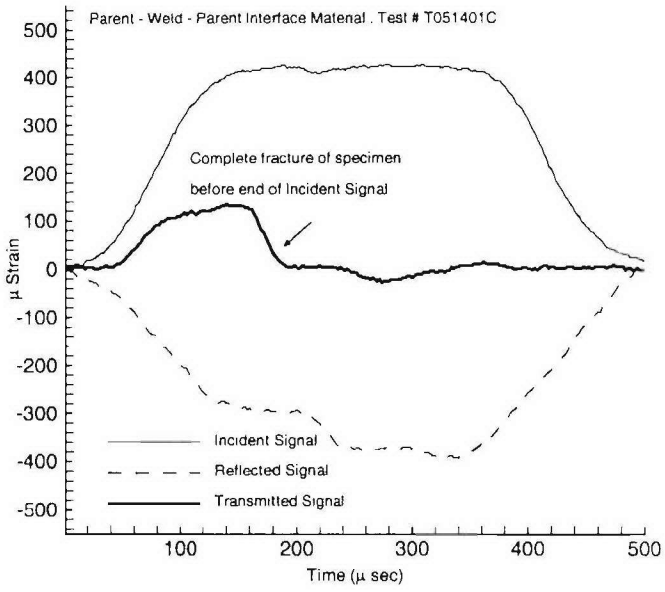

Figure 4.20: Experimental strain-time record of Kolsky bar test T051401C conducted on base/weld interface material.

of 8 different types of elements: PE, PP, PS, HP, HS, WE, WP and WS. Details of the mesh discretization near the root of the notch is shown in Figure 4.19. In Fig. 4.19, the darker material zone to the left consists of the base material and the lighter material zone to the right consists of the weld material. The region shown in light gray between the base and weld material zones is the heat-affected zone. The width of the HAZ is $300\mu m$ and is comparable to the width over which intense variations in the material compositions were observed during XEDS. The location of the HAZ and its orientation was determined by metallography of a cross-section of the welded stainless steel plate. Note that the location of the notch near the base/weld interface provides a direct measure of the strength of the interface when compared to either the base metal or the weld material.

An experimental record of the observed strain-time pulse at the gage stations for test specimen T051401C is shown in Figure 4.20. An analysis of the transmitted signal

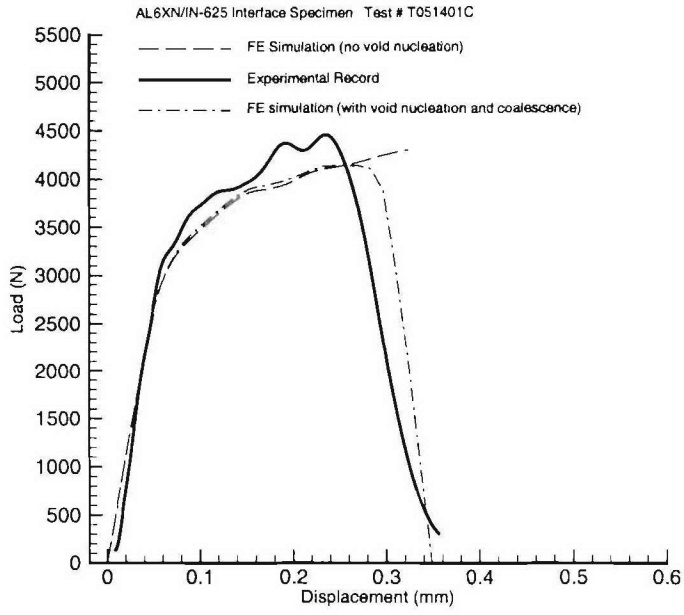

Figure 4.21: Finite element simulation of Kolsky bar fracture test T051401C.

shows that the ductility of the specimen is lower than either T041201C or T051401E. The duration of the loading pulse before complete loss of load-carrying capacity is $\approx 200\mu sec$. A finite element study of the loss of ductility at high strain rates of tensile specimens machined from the HAZ would require an understanding of the strain hardening and damage evolution at the interface. Note that the width of the HAZ is a significant fraction of the thickness of the specimen at the root of the notch. Therefore, the properties of the interface have a strong influence on the deformation and fracture behavior of the test specimen. In our study, we prescribe the flow stress behavior of the HAZ to be overmatched by 5% with respect to the base material. This is consistent with experimental observations on the measured flow stress behavior of specimens machined from near the base/weld interface. The damage evolution in the HAZ is also assumed to be similar to that in the base material.

Results from a finite element simulation of the interface test specimen T051401C

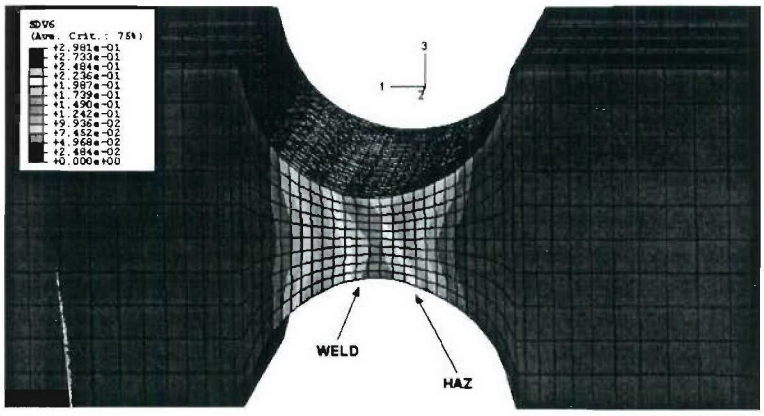

Figure 4.22: Distribution of the effective macroscopic plastic strain (State Variable: SDV6) near the base/weld interface in tensile specimen T051401C. Time T = 159.6μsec. Directions 1, 2 and 3 correspond to the rolling, transverse and weld directions respectively.

are shown in Figure 4.21. The figure also shows FE results of the deformation behavior of the test specimen in the absence of damage evolution. The predicted load-displacement response of the specimen compares quite well with the observed experimental record. The FE results predict a weaker load response and a slightly larger ductility than the measured flow behavior of the specimen. The loss of ductility in the specimen is understood as being due to the increased triaxiality of deformation in the undermatched weld zone. The first instance of void coalescence is at 155.9μsec and is much earlier than in specimens where the HAZ is outside of the zone of plastic deformation. The distribution of plastic strain at the root of the notch in specimen T051401C after 159.6μsec is shown in 4.22. Notice the onset of strain localization in the weld material just ahead of the HAZ. Since the HAZ is clearly overmatched when compared to the weld zone, the imposed far-field displacement is accommodated over a smaller region near the root of the notch.

Figure 4.23 shows the location of failed elements in the tensile specimen T051401C after 200μsec of loading. The specimen is almost fully unloaded as the 'crack'(consisting

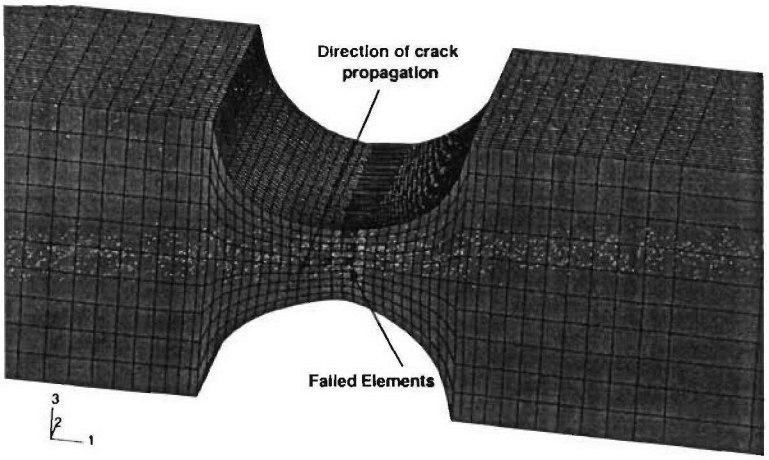

Figure 4.23: Location of failed elements in tensile specimen T051401C after 200μsec. Directions 1, 2 and 3 correspond to the rolling, transverse and weld directions respectively.

of the union of failed elements) has almost fully propagated through the entire specimen. The primary crack plane consists entirely of WP and WS elements in the weld zone. This observation is consistent with SEM observations on the fracture surface of the failed test specimen. Several WP elements, which have either failed or have undergone transition to a post-coalescence mode of deformation, exist in a row of elements adjacent to the primary crack plane. However, the small-scale void growth in these adjacent elements is insufficient to bridge the ligaments between the primary nucleation centers.

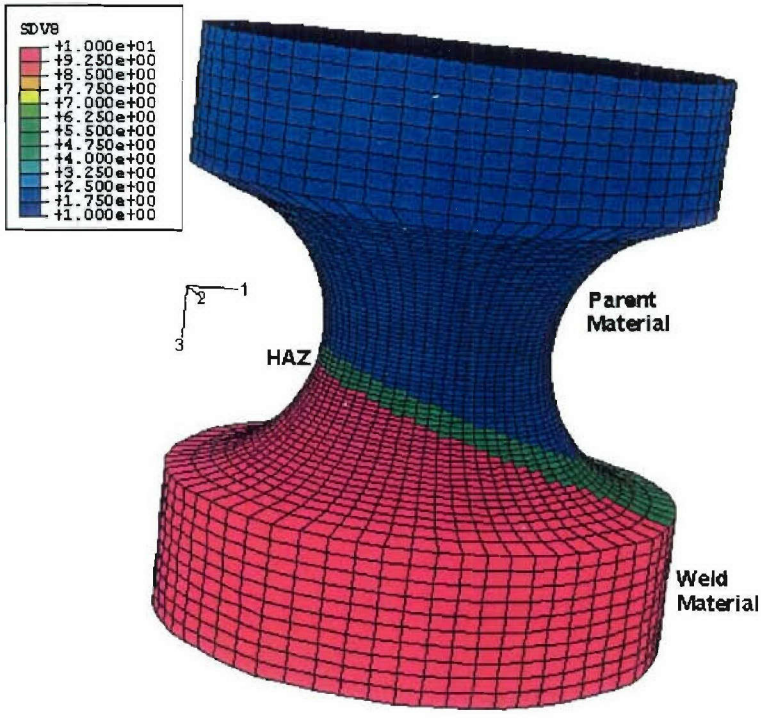

Figure 4.24: Finite element model of a notched cylindrical tensile specimen with a base/weld interface zone. State variable SDV8 stores the material index at each integration point (1.00: Parent, 5.00: HAZ and 10.0: Weld).

4.4 *Finite Element Simulation of Notched Cylindrical Specimens*

Figure 4.24 shows a finite element model for the notched cylindrical tensile specimen S3 machined from the heat-affected zone of the AL6XN stainless steel welded plate P_C. As described in §2.5, the tensile specimen S3 was loaded quasistatically in an Instron until the onset of rapid unloading. Results from an X-ray tomographic investigation of the voided fracture process zone in S3 were described in §2.5. In this section, we will present the results from an attempt to model the deformation and damage evolution in this heterogeneous tensile test specimen using finite element analysis. We will compare the distribution of the void volume fraction predicted by the numerical

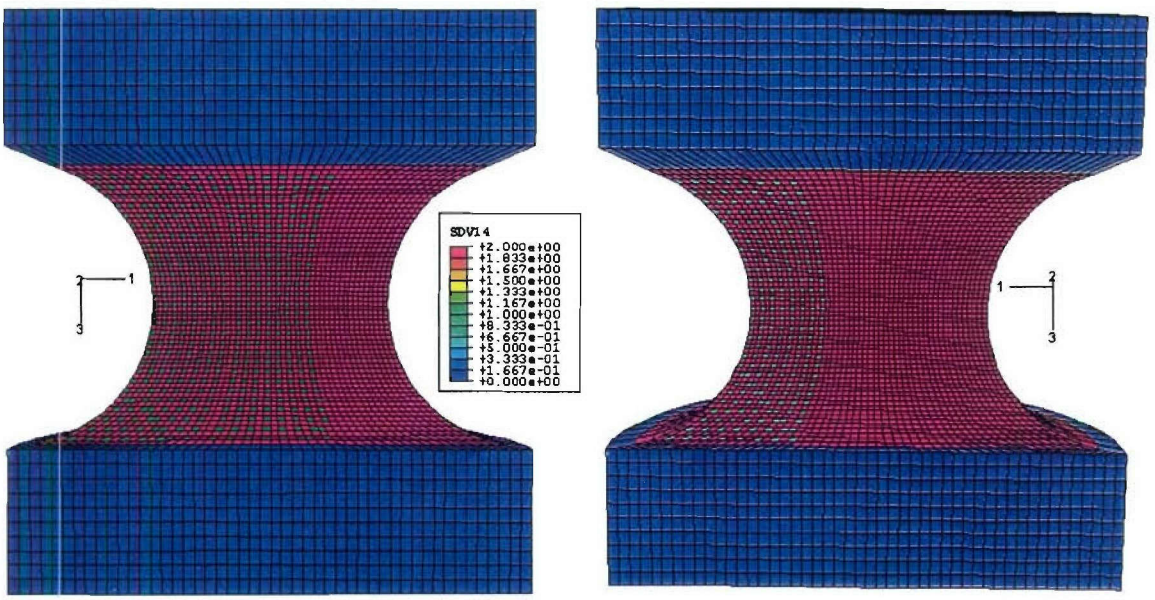

Figure 4.25: Distribution of primary and secondary nucleation centers over a cross-section of the notched cylindrical tensile specimen S3. State variable SDV14 stores the nucleation index (0: E-element, 1.00: P-element and 2.00: S-element).

simulation of ductile fracture in tensile specimen S3 with corresponding experimental observations obtained using X-ray Computed Microtomography.

As shown in Figure 4.24, the tensile test specimen S3 was machined such that the notch is located in the HAZ/weld interface zone and the orientation of the loading is along the rolling direction. The orientations 1,2 and 3 shown in Figure 4.24 correspond to the transverse, weld and rolling directions respectively. The diameter of the tensile specimen S3 is 7.144 mm. The cylindrical specimen has a notch with a radius and depth both equal to 1.985 mm. A gage length of 8 mm symmetrically located above and below the root of the notch is used to construct a finite element model of the tensile specimen. Only a portion of the tensile specimen is included within the FE model as the plastically deforming zone is fully enclosed within the notch over the duration of the experiment. Due to the non-axisymmetric nature of the HAZ/weld interface geometry, a fully three-dimensional discretization based on

eight-noded C3D8R elements is used in the finite element simulation. The overall finite element model consists of 101120 C3D8R elements with a total of 315120 degrees of freedom.

As described in §4.3, the finite element model in the plastically deforming zone of interface tensile test specimens consists of 6 different types of elements: PP, PS, WP, WS, HP and HS. The finite element model outside of the root of the notch consists of either PE or WE-type finite elements. The distribution of the E, P and S-type finite elements across the notch of the tensile specimen S3 is shown in Figure 4.25. The flow stress behavior of the HAZ is prescribed to be overmatched by 5% with respect to the base material. As previously, the flow stress behavior of the base and weld material are described by the constitutive models developed in Chapter 3.

Our finite element formulation of damage evolution, and the numerical integration of the constitutive model, have been optimized for simulation of high-speed impact events in ABAQUS/Explicit. An analysis of this tension test using an explicit dynamics procedure in ABAQUS with a quasistatic loading rate is computationally inefficient due to the large number of time steps required. In our numerical calculations, we applied an enhanced loading rate of $1m/sec$ to the finite element model of the test specimen.

A time step of 4 nanoseconds was used in the numerical integration of the material response before the first instance of void coalescence in the finite element model while a time step of 2 nanoseconds was used thereafter. Using the enhanced loading rate, velocity boundary conditions for uniaxial extension along the 3-direction were applied at the bottom surface of the finite element model. Traction-free boundary conditions were imposed on the curved surfaces of the finite element model for the duration of the simulation. Results from a finite element simulation of the deformation and the damage evolution in tensile test specimen S3 are shown in Figure 4.26. The

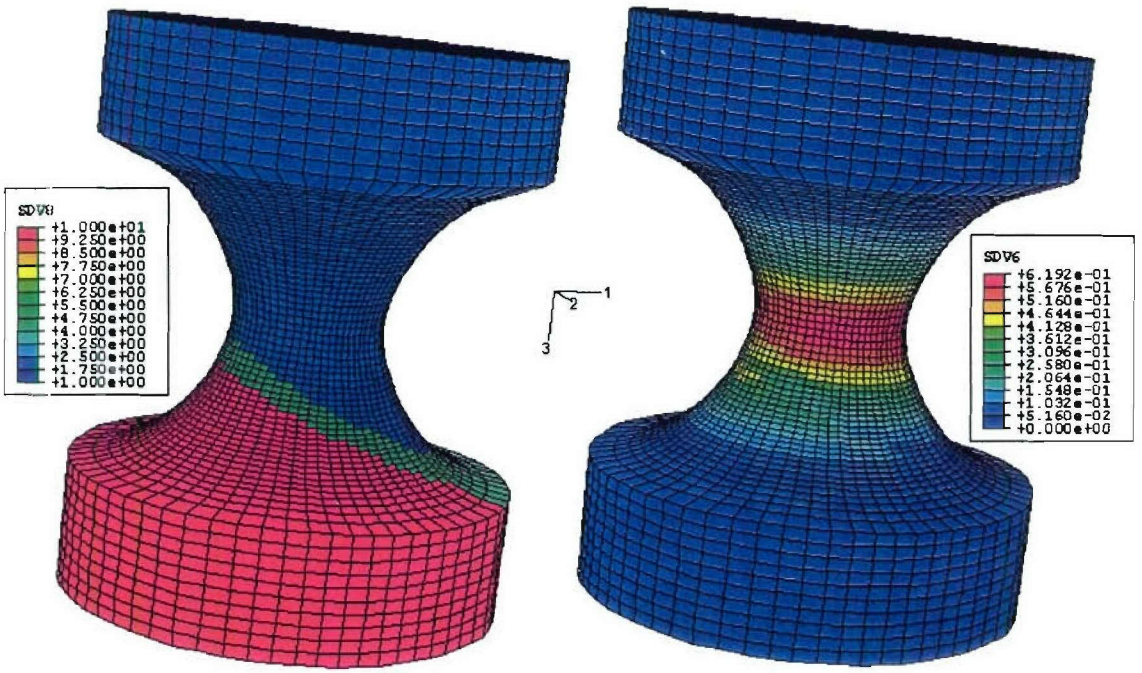

Figure 4.26: Deformation of the notched cylindrical tensile specimen S3 after a displacement of $960\mu m$ in the rolling direction. The figure on the left shows the distribution of the base, weld and HAZ materials in the deformed finite element model. State variable SDV8 stores the material index at each integration point (1.00: Parent Material, 5.00: HAZ and 10.0: Weld). The figure on the right shows the distribution of the macroscopic effective plastic strain (State Variable: SDV6).

computed load-displacement response of the finite element model for S3 is shown in Figure 4.27. The XCMT imaging data was obtained after an extension of $870\mu m$. The finite element model predicted failure of P-elements near the location of the primary void cluster after a vertical displacement of approximately $960\mu m$. Even though substantial growth of voids was observed in the finite element model at a displacement of $870\mu m$, it was insufficient to cause failure of any of the P-elements. The distribution of the effective macroscopic plastic strain (state variable: SDV6) and the constituent material index (state variable: SDV8) are shown in Figure 4.26. The primary effect of the presence of the HAZ/weld interface in the tensile specimen is seen in the asymmetric nature of the deformation about the rolling direction (3-axis).

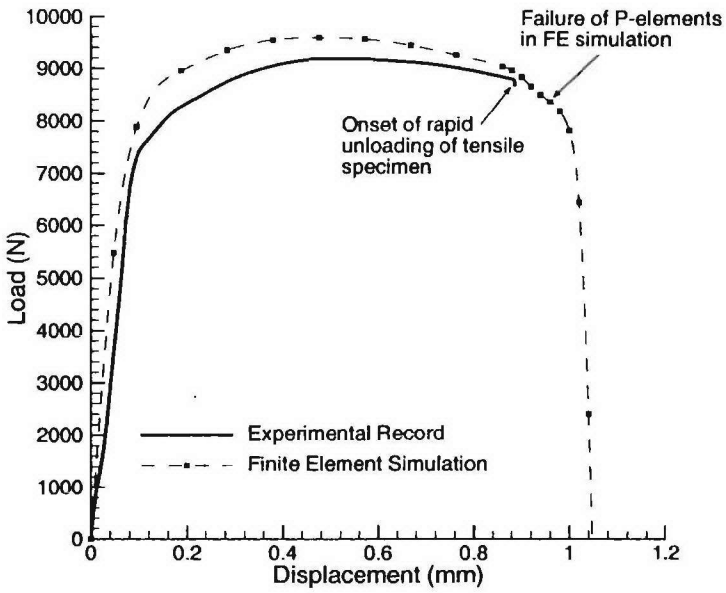

Figure 4.27: Computed load-displacement response of the finite element model for the interface tensile test specimen S3. The predicted loads are slightly higher due to the enhanced loading rate in the FE simulation.

The distribution of the macroscopic effective plastic strain over a cross-section of the finite element model is shown in Figure 4.28. The distribution of the void volume fraction over a cross-section of the finite element model is shown in Figure 4.29.

The location of the failed finite elements (i.e. where the ligament ratio $\chi > 0.975$) across a section of the notched tensile specimen are shown in Figures 4.30-4.32. The primary plane of failed elements in this finite element model of the tensile specimen S3 is indicated in Figure 4.30. The progressive development of damage in the row of finite elements corresponding to this primary crack propagation plane is also shown in Figures 4.30-4.32. The evolution of damage within the primary plane of crack propagation is distributed quite evenly about the transverse 1-direction, except for some effects associated with local variations in the nucleation site distribution within the plane.

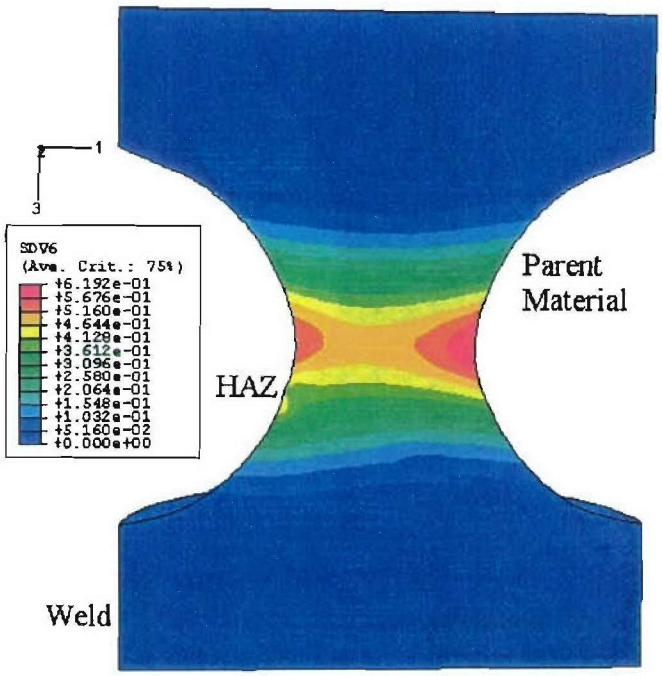

Figure 4.28: Distribution of the effective macroscopic plastic strain over a cross-section of the finite element model for tensile specimen S3 after a vertical displacement of $960\mu m$ along the rolling direction.

An analysis of the entire finite element model indicated that the failure zone was localized entirely within the base material i.e., no failed elements were located in the HAZ/weld interface zone. While some enhanced void growth is shown in the weld material adjacent to the HAZ (see Figure 4.29), all of the WP/WS/HP/HS elements in the region were intact at the end of the simulation. As seen in Figure 4.26, the HAZ/weld interface region is inclined away from the centerline of the notch. The lower accumulated plastic strains and the reduced triaxiality of deformation in this region appears to have contributed significantly to the structural integrity of the HAZ/weld interface in tensile specimen S3. This result also correlates with X-ray tomographic observations in §2.5 wherein the primary void cluster was found to be located within the base AL6XN material. In addition, there is a significant variation in the void volume fraction distribution near the base/HAZ interface. In

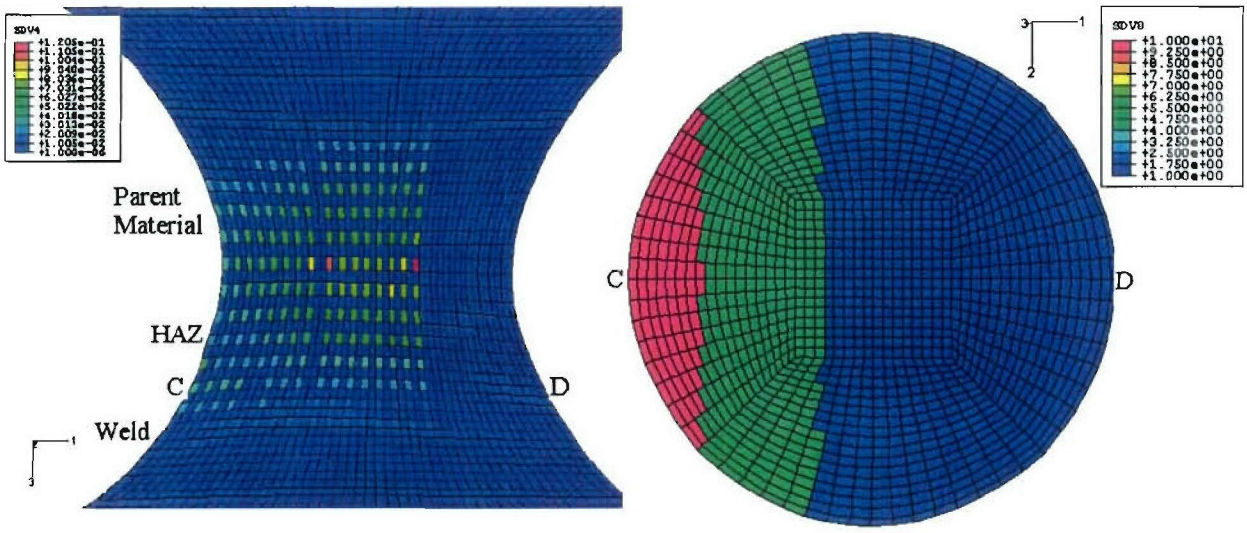

Figure 4.29: Distribution of the void volume fraction (state variable: SDV4) over a cross-section of the finite element model for tensile specimen S3 after a vertical displacement of $960\mu m$ along the rolling direction. The circular section on the right is from the slice of finite elements corresponding to plane CD. State variable SDV8 stores the material index (1.00: Parent, 5.00: HAZ and 10.0: Weld) at each integration point. Enhanced void growth is seen in the weld zone adjacent to the inclined HAZ.

particular, the void volume fraction within the HAZ is significantly lower than in the base material immediately adjacent to it. We believe that the emergence of contrast in the XCMT sample (near the location of the microvoid clusters) is due to such a density variation near the base/HAZ interface.

Our numerical simulations indicate that the primary plane of crack propagation in the finite element model is approximately $300\mu m$ below the plane where the primary void cluster is observed in the XCMT data, as shown in Frame 155 (Figure 2.32). The projection of the imaged primary void cluster on the failure plane in the finite element model in shown in Figure 4.30. As shown in Figure 4.30, the location of the primary void cluster is slightly offset from the 1-3 symmetry plane (formed by the transverse and rolling directions). The offset of the primary void cluster from the 2-3 plane (formed by the weld and rolling directions) is attributed to the presence of the inclined

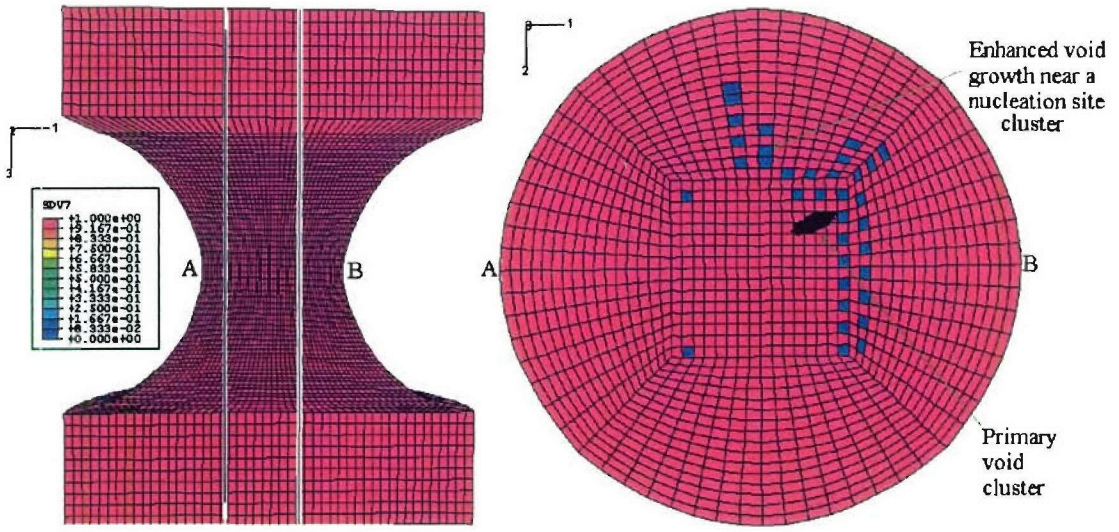

Figure 4.30: Location of failed elements in the finite element model for tensile specimen S3 after a vertical displacement of $960\mu m$. Failed elements are shown in blue and have the ligament ratio $\chi > 0.975$. Intact elements are shown in red. The region between the two white lines corresponds to the zone from which the XCMT sample was prepared using EDM. AB is the primary plane of crack propagation. The circular section shown on the right is from the slice of finite elements in plane AB. The physical location of the primary void cluster in the 1-2 plane is as shown above.

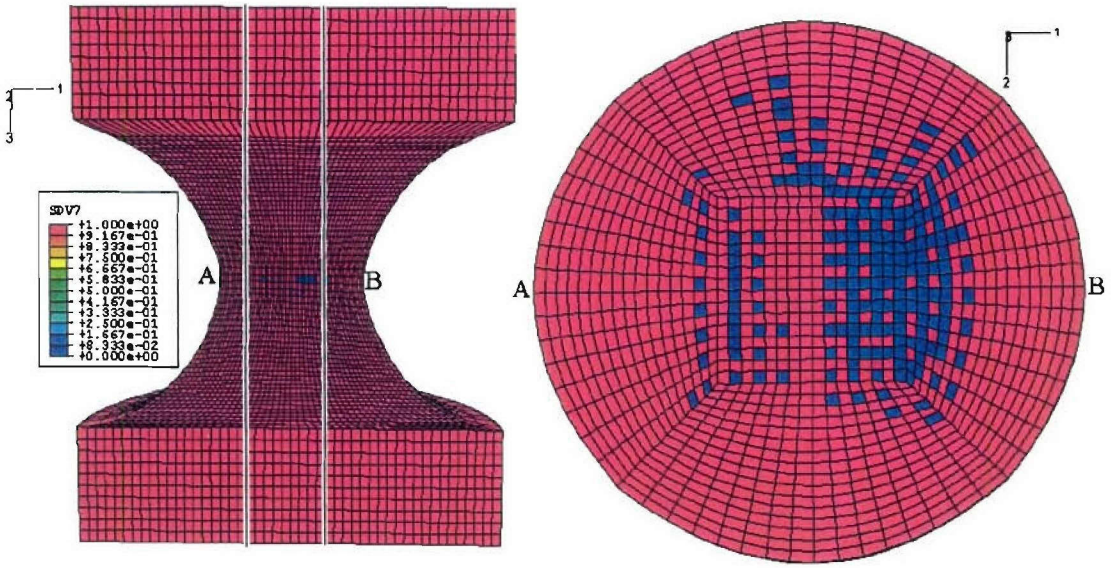

Figure 4.31: Location of failed elements in the finite element model for tensile specimen S3 after a vertical displacement of 1.020 mm. AB is the primary plane of crack propagation. Failed elements are shown in blue.

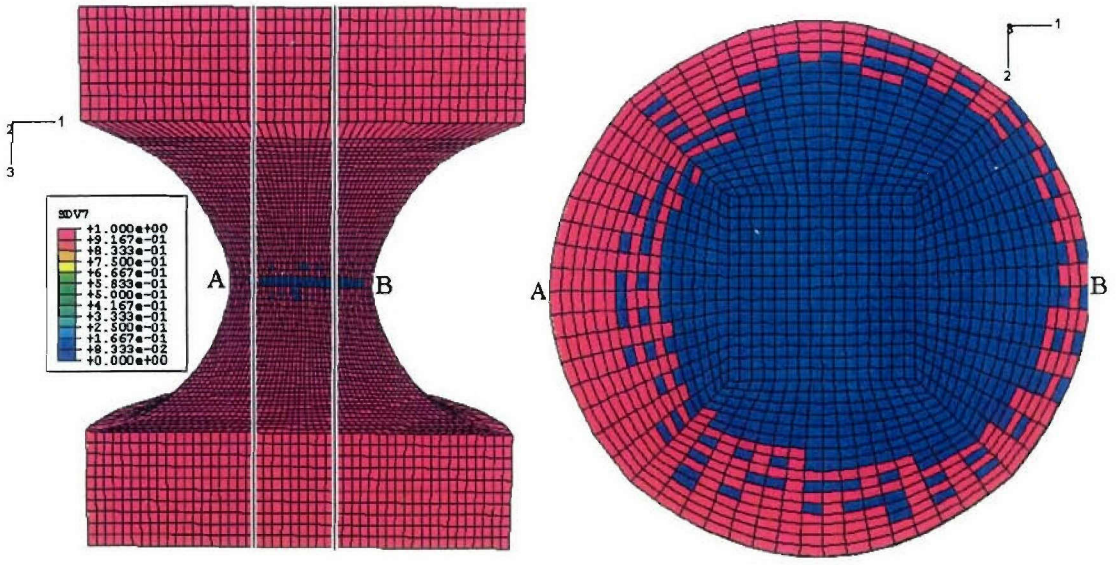

Figure 4.32: Location of failed elements in the finite element model for tensile specimen S3 after a vertical displacement of 1.040 mm. AB is the primary plane of crack propagation.

HAZ/weld interface (see Figure 4.28). The location of the primary void cluster could also be affected by local variations in the strength of the base/weld/HAZ material which are not described by the constitutive models developed in Chapter 3. However, we believe that the offset of the primary void cluster from the 1-3 symmetry plane is due mainly to local variations in strength and spacing of the primary nucleation sites in the matrix. Notice the artifact in Figure 4.29 showing enhanced void growth near a nucleation site cluster formed by the inadvertent placement of two P-elements adjacent to each other. A similarly located nucleation site cluster at a more favorable location (for instance, on the 1-3 symmetry plane and offset in the positive 1-direction from the center of the of the tensile specimen) could serve to localize the deformation and the void volume fraction over a much smaller region than obtained by assuming a uniform site distribution.

Discussion

The primary differences between our finite element simulations of damage evolution in tensile specimen S3 and the experimental observations obtained using XCMT lie in the predicted distribution of the void volume fraction. In particular, the finite element simulations predict much higher void volume fractions at locations outside of the primary void cluster. Predicted void volume fractions are sufficiently large that they should be observed if present in the experiments. For example, a 5% void volume fraction (corresponding to approximately a $30\mu m$ diameter void in a cube of size $h = 66\mu m$) is entirely within our limits of detection in beamline X27A at the National Synchrotron Light Source. While the finite element calculations predict preferential evolution of damage near the location where the primary void cluster was observed, substantial amounts of additional void growth are also predicted both within the primary plane of crack propagation and outside of it. As shown in Figure 4.29, some of the P-elements outside of the primary plane of crack propagation have failed. (It should be noted that none of the S-elements outside of the primary plane of crack propagation have failed.) The XCMT observations indicate, however, that the damage was confined entirely to a $77\mu m$ thick slice of the base AL6XN stainless steel.

The differences between the numerical simulation of the void volume fraction and the experimental observations raise several issues relative to modeling ductile fracture in these high-strength steels using Gurson-type constitutive models. These issues include: (a) choice of the q-parameters (q_1 *and* q_2 in Eqn.3.22) in the Gurson-Tvergaard-Needleman formulation for void growth; (b) choice of void nucleation parameters; (c) importance of void shape effects prior to coalescence and its effect on void growth models; and (d) difficulties in modeling failure at low triaxialities ($T < 2/3$).

Tvergaard (1981) introduced the parameters q_1 and q_2 in the original Gurson

criterion to match its predictions with numerical simulations of strain localization between voids. He suggested the use of $q_1 = 1.5$ and $q_2 = 1.00$ in Eqn. 3.22. Tvergaard (1991) reviewed the experimental evidence for the use of various values of q_1 and q_2 in the Gurson constitutive model. Based on experiments conducted on sintered materials with known porosity, he reported that a value of q_1 in the range of 1.25 to two and $q_2 \approx 1$ provides a generally accurate representation of the load-displacement response of ductile porous solids. However, experimental evidence for the use of various q values for industrial alloys with extremely small voids (with initial size $\approx 1-2\mu m$) is lacking. Koplik and Needleman (1988) carried out extensive axisymmetric void cell calculations for stress triaxialities in the range of $1 \leq T \leq 3$. They compared the macroscopic effective stress-strain response and the void growth response of the computational cell (under proportional loading) with corresponding predictions of the Gurson model for various values of q_1 and q_2. They report that using $q_1 \approx 1.25$ and $q_2 \approx 1.00$ gives a very good fit to cell-model results. However, as can be seen from the results of Koplik and Needleman (1988), their comparisons deteriorate for $T = 1$ in comparison with those for $T = 2$ or $T = 3$. In fact, their results suggest that there may be no set of values for the parameters q_1 and q_2 (within the framework of the Gurson-Tvergaard-Needleman formulation) that accounts simultaneously for the evolution of void volume fraction and the macroscopic flow response at low triaxialities.

In our finite element model, we assume that the void aspect ratio W (defined as $W = R_Z/R_r$) is equal to one before void coalescence and evolves only after the onset of void coalescence. While this assumed behavior is expected to be reasonably accurate for void evolution at high stress-triaxialities, at low stress-triaxialities, significant variations can be expected in void shape even prior to void coalescence. Lee and Mear (1999) have studied the effects associated with neglecting the void shape in constitutive models for porous materials. They examine the error associated with

predicting the growth in void-volume fraction for initially circular cylindrical voids growing in a power-law viscous matrix. They find that for sufficiently small triaxialities ($T < 0.6$), the void volume is overestimated (sometimes by a factor of 2) when the evolution of the void aspect ratio is neglected.

Constitutive models which take into account the evolution of void shape prior to coalescence have been proposed recently by Gologanu (1997). Gologanu (1997) has developed a Gurson-type model for prolate and oblate shaped voids by incorporating a class of axisymmetric velocity fields developed by Lee and Mear (1992). They base their model on the analysis of the growth of a spheroidal void in a finite, perfectly plastic solid with an outer confocal surface. Early results by Benzerga (2000) based on finite element implementation of this enhanced Gurson model show promise for improved predictions of void growth rates and coalescence at low triaxialities. Using a computational void cell approach similar to Koplik and Needleman (1988), Benzerga (2000) obtains a fairly good fit in modeling the macroscopic stress-strain response and the void-volume fraction at stress triaxialities in the range of $1/3 \leq T \leq 3$. While our Gurson-Tvergaard-Needleman formulation for void growth predicts a more diffuse damage zone near the root of the notch than observed experimentally, we expect that the use of this enhanced Gurson-type constitutive model would predict lower void growth rates and a more localized zone of damage.

In this thesis, void nucleation parameters were prescribed by matching the global load-displacement response for finite element simulations of tensile tests on homogeneous specimens of base or weld material. While these parameters were sufficiently accurate to model the global load-displacement response of the tensile test specimens, they appear to be unreliable in predicting the void volume fraction at coalescence. It appears that our choice of the volume fraction of void nucleating particles (f_0 in Eqn. 4.3) is much higher than what could be expected from debonding of the micron-sized

precipitates in these high strength alloys. The use of a lower value for f_0 would necessitate use of larger values of q_1 to match the global load-displacement response of the Kolsky bar tensile specimens. However, the use of q_1 outside of the range of 1.00 to 1.50 leads to a significant mismatch between the computational cell-model results and predictions of Gurson-type constitutive models (as observed by Koplik and Needleman (1988)). In particular, the selection of void nucleation parameters $(f_N^\epsilon, \epsilon_c)$ to improve agreement with the measured load-displacement response at imminent failure, based on the void coalescence model proposed here, appears to overestimate the void-volume fractions at incipient failure. While extensive unit-cell calculations have shown that the Thomason upper-bound model to be fairly accurate in predicting the onset of a uniaxial straining mode of deformation, its correlation with the evolution of porosity has not been established experimentally.

4.5 Summary

In this chapter, we have presented the results from a finite element study of deformation and ductile fracture in AL6XN/INCONEL-625 stainless steel weldments. These simulations were conducted based on a finite-deformation, porous, elastic-viscoplastic constitutive model developed in Chapter 3. The constitutive models for the base, weld and heat-affected zone of the welded plate were incorporated as a user-material routine VUMAT in ABAQUS/Explicit. Finite element simulations of Kolsky bar tests on tensile test specimens machined from the various material zones of the AL6XN welded plate were conducted using ABAQUS/Explicit

In an attempt to evaluate the sensitivity of the finite element simulation of ductile fracture to progressive refinements in mesh size, we conducted a numerical study of the high rate deformation and fracture response of a notched tensile specimen at various discretizations. This study indicated that the post-coalescence behavior is strongly influenced by the small-scale void nucleation and growth behavior in the S-type finite elements. This behavior is expected to be the norm for high strength alloys which contain an insignificant concentration of primary nucleation centers in the form of weakly bonded precipitates. Because ultimate failure is strongly connected to the behavior of the S-type elements, the predicted results are relatively insensitive to mesh size for mesh sizes small enough that S-type elements surround the P-type elements, *i.e.*, mesh sizes less than or equal to $66\mu m$ for the model used here. In our numerical simulations, we consistently employ a microstructural length scale of $h \approx 66\mu m$ to discretize the plastically deforming zone in the tensile specimen.

The high rate tensile response of homogeneous notched tensile specimens from the base and weld zones were modeled quite successfully using the void nucleation parameters in Table 4.1. The predicted load-displacement response for these specimens

showed good agreement with the experimental record. The finite element simulations were also generally accurate in modeling the onset of void coalescence and rapid unloading in the post-coalescence regime. The high rate response of the notched tensile specimens machined from the heat-affected zone was explained as arising mainly from the interaction of the overmatched HAZ sandwiched between the base material and the undermatched weld zone. The finite element simulation of the interface test specimen T051401C was quite successful in predicting the overall strain hardening behavior and the measured failure response. The nature of deformation and void growth in the interface tensile test specimen S3 (from which the XCMT data was obtained) was also investigated using fully three-dimensional finite element simulations. The location of voided zones predicted by the FE simulations were found to be in approximate agreement with experimental observations obtained using XCMT. We believe that differences between the numerically simulated void-volume fraction and the experimentally observed distribution obtained using XCMT are arising primarily because of difficulties in modeling ductile fracture at low stress triaxialities.

The results from these finite element simulations indicate that the Gurson-type constitutive model for porous materials together with a microstructural length scale and an upper-bound approach for modeling the onset and evolution of void coalescence is a useful tool for modeling the dynamic failure of heterogeneous weldments.

Chapter 5

Concluding Remarks

The primary objective of this thesis was to study the high-rate viscoplastic flow and damage evolution in stainless steel welded plates under impact loading conditions. The mechanical response of two different stainless steel weldments: NITRONIC-50/ER-209 and AL6XN/IN-625 was studied using a combination of quasistatic experiments in an Instron and high rate experiments in two Kolsky bar configurations. The results of these experiments indicate the presence of an overmatched heat-affected zone and an undermatched weld zone in these stainless steel welded plates. Motivated by the interest expressed by the Navy in potentially using AL6XN/IN-625 as a hull material in surface combat ships, we investigated the dynamic response of notched tensile specimens under high rate tensile loading conditions in a novel Kolsky bar configuration. Under nominally identical loading conditions, the ductility of the IN-625 weld filler material was found to be lower than that of the AL6XN base stainless steel. The ductility of notched tensile specimens machined from the HAZ was found to be even lower than the weld material under similar test conditions.

As an attempt to model the mechanics of ductile fracture in these heterogeneous weldments, a finite-deformation, elastic-viscoplastic constitutive model was

developed for porous materials. The internal microstructure of the voided material was represented through 5 state variables: (i) effective flow stress of the matrix σ_m, (b) inter-void ligament ratio χ, (c) void aspect ratio W, (d) void spacing ratio λ and (e) void shape factor γ. A finite element framework for the evolution of the internal state variables ($\sigma_m, \chi, W, \lambda$ *and* γ) and integration of the macroscopic viscoplastic flow was developed for two distinct flow regimes: pre-coalescence and post-coalescence. The constitutive model was implemented as a user-material routine VUMAT in ABAQUS/Explicit.

The high rate tensile response of base and weld specimens from the AL6XN/IN-625 welded plate were successfully modeled using fully three-dimensional finite element simulations in ABAQUS/Explicit. A numerical analysis of the high rate tensile response of the HAZ was successful in predicting the overall strain hardening and the failure response of the heterogeneous interface specimen. In particular, the finite element simulations were able to predict the substantially lower ductility of HAZ specimens. The finite element simulations also reveal the strong sensitivity of the tensile failure response of the HAZ to the presence of porosity near the HAZ/weld interface and to strength fluctuations in the HAZ itself.

In this thesis, we have presented the results obtained from an X-ray tomographic investigation of the voided fracture process zone in a tensile specimen at incipient failure. A volumetric reconstruction of the microstructure from the root of a plastically deformed notched tensile specimen at the onset of void coalescence was obtained. A finite element simulation of the evolution of damage in the tensile specimen from which the tomographic images were obtained was in good agreement with the measured location of the void cluster. The finite element simulations indicate a need to further characterize the onset of void nucleation and nucleation site distribution in the matrix.

The differences between the computed void-volume fraction distribution and experimental observations obtained using XCMT provide insights into developing more physically motivated models of ductile fracture and designing additional experiments to probe them. From our discussion in §4.4, it is evident that current models of ductile fracture are more reliable at stress triaxialities outside of the range that occurred in the tensile specimen from which the XCMT sample was prepared. If so, could an XCMT sample be prepared from a tensile specimen which has undergone extensive plastic deformation at higher stress triaxialities? Such a test would facilitate a direct comparison of measured void volume fraction at stress triaxialities where current understanding of ductile fracture is more reliable. As discussed in §2.5, difficulties could arise due to the localized nature of deformation and the rapid sequence of events between void coalescence and complete rupture in the high strength alloys studied here. At high stress triaxialities, it would be a more challenging task to stop the loading in time to retain the voided fracture-process zone within the interior of the XCMT sample.

We also believe that recent efforts towards including the effect of void shape on modeling ductile fracture are of considerable importance in the low stress triaxiality regime. The general nature of the emergence of localized damage zones in diffuse deformation fields at low stress triaxialities also needs to be studied systematically.

Appendix A

Axisymmetric Stress Wave Propagation in a Kolsky Bar

In this appendix, we will present details of the dispersion correction to the measured elastic wave propagation record at the strain gage stations on the incident and transmitter bar. Let $\epsilon^I(t)$, $\epsilon^R(t)$ and $\epsilon^T(t)$ represent the trace of the recorded incident, reflected and transmitted strain signals. Consider the discrete representation of the strain pulse recorded at either gage station as

$$\epsilon_k = \epsilon(k\Delta); \quad k = 0, 1, 2, \ldots, N-1 \tag{A.1}$$

where Δ is the time interval at which data is recorded in the digital oscilloscopes and N is the number of sampled data points. The discrete Fourier transform of the strain pulse is given by

$$\tilde{\epsilon}(f_n) = \Delta \sum_{k=0}^{N-1} \epsilon_k e^{2\pi i f_n k\Delta} \tag{A.2}$$

where f_n is the frequency component defined as

$$f_n = \frac{n}{N\Delta}; \quad n = 0, \ldots, N-1. \tag{A.3}$$

A FORTRAN subroutine (*Numerical Recipes*: FOUR1) based on a Cooley-Tucker algorithm is used to obtain the complex Fourier transform of the real data string ϵ_k. To enable use of the Fast Fourier Transform subroutine, the number of sampled data points is increased to the nearest power of 2 by adding additional zeroes at the end of the signal. The phase angle ϕ_n of the frequency component f_n is given by

$$\tan(\phi_n) = \frac{IM[\tilde{\epsilon}(f_n)]}{RE[\tilde{\epsilon}(f_n)]} \tag{A.4}$$

where IM and RE represent the imaginary and real parts of the transformed strain pulse. The amplitude of the frequency component f_n is given by

$$AMP(f_n) = \sqrt{IM[\tilde{\epsilon}(f_n)]^2 + RE[\tilde{\epsilon}(f_n)]^2}. \tag{A.5}$$

The propagation of the dispersive strain pulse from the strain gage stations to the specimen/bar interface is obtained by propagating each individual frequency component of the signal by its phase velocity. The phase velocity of each individual component is obtained through Bancroft's numerical solution (Bancroft 1941) of the Pochhammer-Chree dispersion relation (Pochhammer (1876), Chree (1889)) for the first mode of vibration as

$$\frac{c_n}{c_0} = B(\frac{b}{\Lambda_n}, \nu). \tag{A.6}$$

where c_0 is the bar velocity $\left(\frac{E}{\rho}\right)^{1/2}$ predicted by the non-dispersive one-dimensional longitudinal wave propagation theory, b is the diameter of the Kolsky bar, Λ_n is the wavelength of the Fourier component and $B(\frac{b}{\Lambda_n}, \nu)$ is a complex nonlinear function. The phase velocity of any frequency component f_n is also given by

$$c_n = f_n \Lambda_n. \tag{A.7}$$

The phase velocity of any individual Fourier component is therefore obtained by a simultaneous solution of Eqn. A.6 with Eqn. A.7. Figure A.1 shows the numerical

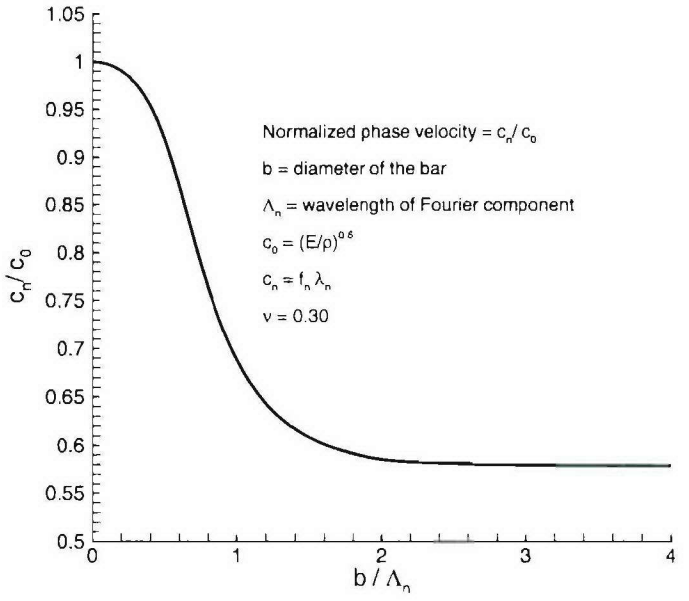

Figure A.1: Numerical solution to the Pochhammer-Chree dispersion relation for the first vibrational mode.

solution to the Pochhammer-Chree dispersion relation for the first mode of vibration as obtained by Bancroft (1941).

Let D_s represent the distance between the strain gage station and the specimen/bar interface. The phase shift undergone by a frequency component f_n, propagating in a non-dispersive fashion is given by

$$\phi_0 = 2\pi f_n \frac{D_s}{c_0}. \tag{A.8}$$

If the same frequency component were to propagate dispersively, the phase angle difference would be given by

$$\phi^* = 2\pi f_n \frac{D_s}{c_n}. \tag{A.9}$$

The phase angle of any individual Fourier component at the specimen/bar interface

is therefore given by

$$\phi_n^{INT} = \phi_n + \phi^* - \phi_0. \tag{A.10}$$

The reconstructed Fourier components at the specimen/bar interface is given by

$$RE[\tilde{\epsilon}(f_n)]^{INT} = AMP(f_n)\cos(\phi_n^{INT}) \tag{A.11}$$

$$IM[\tilde{\epsilon}(f_n)]^{INT} = AMP(f_n)\sin(\phi_n^{INT}). \tag{A.12}$$

The strain pulse at the specimen/bar interface is thereafter obtained by an inverse Fourier transform of the reconstructed frequency components. Note that the distance D_s is positive for the incident signal which is propagated forward to the specimen/bar interface and negative for the reflected and transmitted strain signals.

Appendix B

Rate-Tangent-Modulus Method for Integration of the Porous Constitutive Model Prior to Void Coalescence

The flow potential governing the evolution of voided microstructures prior to the onset of coalescence is given by Eqn. 3.39 as

$$\Phi|_{c-} = \frac{\Sigma_G^2}{\sigma_m^2} + 2q_1 f \cosh(\frac{3q_2\Sigma_h}{2\sigma_m}) - 1 - q_1^2 f^2. \tag{B.1}$$

Define the equivalent effective strain rate during the time increment from t to $t + \Delta t$ as

$$\dot{\epsilon}_m = (1 - \Gamma)\dot{\epsilon}_m^{(n)} + \Gamma\dot{\epsilon}_m^{(n+1)} \tag{B.2}$$

where the effective strain rate the the end of the time step $\dot{\epsilon}_m^{(n+1)}$ is obtained using a Taylor approximation as

$$\dot{\epsilon}_m^{(n+1)} = \dot{\epsilon}_m^{(n)} + \Delta t \left[\frac{\partial\dot{\epsilon}_m}{\partial\sigma_m}\dot{\sigma}_m + \frac{\partial\dot{\epsilon}_m}{\partial\epsilon_m}\dot{\epsilon}_m + \frac{\partial\dot{\epsilon}_m}{\partial\theta_m}\dot{\theta}_m\right]_{t=t_n}. \tag{B.3}$$

Here, the derivatives $\frac{\partial \dot{\epsilon}_m}{\partial \sigma_m}$, $\frac{\partial \dot{\epsilon}_m}{\partial \epsilon_m}$ and $\frac{\partial \dot{\epsilon}_m}{\partial \theta_m}$ are evaluated at the beginning of the time step from the constitutive model for the incompressible matrix material. The rate of evolution of the matrix effective stress is obtained from the plastic consistency condition for integration of the above viscoplastic flow potential. The plastic consistency relation for the above flow potential can be written as

$$\frac{\partial \Phi|_{c-}}{\partial \Sigma_G}\dot{\Sigma}_G + \frac{\partial \Phi|_{c-}}{\partial \Sigma_h}\dot{\Sigma}_h + \frac{\partial \Phi|_{c-}}{\partial \sigma_m}\dot{\sigma}_m + \frac{\partial \Phi|_{c-}}{\partial f}\dot{f} = 0. \tag{B.4}$$

Substituting the pre-coalescence flow potential (Eqn. 3.39) in Eqn. B.4, we get

$$\frac{2\Sigma_G}{\sigma_m^2}\dot{\Sigma}_G - \left\{\frac{2\Sigma_G^2}{\sigma_m^3} + 3fq_1q_2s\frac{\Sigma_h}{\sigma_m^2}\right\}\dot{\sigma}_m + (2q_1c - 2q_1^2f)\dot{f} + \frac{3q_1q_2f}{\sigma_m}s\dot{\Sigma}_h = 0, \tag{B.5}$$

where c and s are given by

$$c = \cosh\left(\frac{3q_2\Sigma_h}{2\sigma_m}\right) \tag{B.6}$$

$$s = \sinh\left(\frac{3q_2\Sigma_h}{2\sigma_m}\right). \tag{B.7}$$

The hydrostatic component of the macroscopic Cauchy stress is given by

$$\Sigma_h = \frac{1}{3}\mathbf{I} : \mathbf{\Sigma}. \tag{B.8}$$

Differentiating Eqn. B.8 and using Eqn. 3.104, we get

$$\dot{\Sigma}_h = \frac{1}{3}\mathbf{I} : \overset{\Delta}{\mathbf{\Sigma}} + \underbrace{\frac{1}{3}\mathbf{I} : (\Omega^e\mathbf{\Sigma} - \mathbf{\Sigma}\Omega^e)}_{=0}. \tag{B.9}$$

The last term in Eqn. B.9 can be shown to vanish. The evolution of Σ_h is therefore given by

$$\dot{\Sigma}_h = \frac{1}{3}\mathbf{I} : \overset{\Delta}{\mathbf{\Sigma}} = \frac{1}{3}\left\{\boldsymbol{I} : \left(\frac{1}{J}\mathcal{C}^e : [\mathbf{D} - \mathbf{D^p} - \mathbf{D^T}]\right)\right\}. \tag{B.10}$$

The macroscopic Cauchy stress at a material point is defined by

$$\Sigma_G^2 = \frac{3}{2}\mathbf{\Sigma}' : \mathbf{\Sigma}' \tag{B.11}$$

where $\boldsymbol{\Sigma}'$ is the deviatoric Cauchy stress tensor. Differentiating Eqn. B.11, and using Eqn. 3.104 we get,

$$2\Sigma_G\dot{\Sigma}_G = 3\boldsymbol{\Sigma}' :\overset{\Delta}{\boldsymbol{\Sigma}} + \underbrace{3\boldsymbol{\Sigma}' : (\Omega^e\boldsymbol{\Sigma} - \boldsymbol{\Sigma}\Omega^e)}_{=0}. \tag{B.12}$$

The last term in Eqn. B.12 can be shown to vanish. The evolution of the macroscopic Cauchy stress is therefore given by

$$\dot{\Sigma}_G = \frac{3}{2\Sigma_G}\boldsymbol{\Sigma}' :\overset{\Delta}{\boldsymbol{\Sigma}} = \frac{3}{2\Sigma_G}\left\{\boldsymbol{\Sigma}' : \left(\frac{1}{J}\mathcal{C}^e : [\mathbf{D} - \mathbf{D^P} - \mathbf{D^T}]\right)\right\}. \tag{B.13}$$

Define the scalar quantities, C_Σ and C_I as

$$C_\Sigma = \mathbf{I} : (\mathcal{C}^e : [\mathbf{D}]) \tag{B.14}$$

$$C_I = \boldsymbol{\Sigma}' : (\mathcal{C}^e : [\mathbf{D}]) \tag{B.15}$$

Using Eqns. 3.28 and 3.21, and substituting in Eqn. B.10 and Eqn. B.13, we obtain

$$\dot{\Sigma}_G = \frac{3C_\Sigma}{2\Sigma_G J} - \frac{E\Sigma_G\Lambda_1}{J(1+\nu)}\,\dot{\epsilon}_m \tag{B.16}$$

$$\dot{\Sigma}_h = \frac{C_I}{3J} - \frac{E}{J(1-2\nu)}\left(\Lambda_2 + \frac{\beta\alpha\sigma_m}{\rho c_p}\right)\,\dot{\epsilon}_m \tag{B.17}$$

where the coefficients Λ_1 and Λ_2 are obtained from Eqn. 3.27 and Eqn. 3.28 as

$$\Lambda_1 = \frac{3(1-f)/\sigma_m}{\boldsymbol{\Sigma} : \frac{\partial\Phi}{\partial\boldsymbol{\Sigma}}} \tag{B.18}$$

$$\Lambda_2 = \frac{q_1 q_2 f(1-f)/\sigma_m}{\boldsymbol{\Sigma} : \frac{\partial\Phi}{\partial\boldsymbol{\Sigma}}}. \tag{B.19}$$

The evolution of the void volume fraction is computed from Eqn. 3.29 as

$$\dot{f} = 3(1-f)\Lambda_2\dot{\epsilon}_m + N_\epsilon\dot{\epsilon}_m + N_\sigma(\dot{\sigma}_m + \dot{\Sigma}_h). \tag{B.20}$$

Substituting for $\dot{\Sigma}_h$ from Eqn. B.17, we get

$$\dot{f} = \left\{3(1-f)\Lambda_2 + N_\epsilon - \frac{N_\sigma E}{J(1-2\nu)}\left(\Lambda_2 + \frac{\beta\alpha\sigma_m}{\rho_m c_p}\right)\right\}\dot{\epsilon}_m + N_\sigma\left(\frac{C_I}{3J} + \dot{\sigma}_m\right) = 0. \tag{B.21}$$

Solving for $\dot{\sigma}_m$ from Eqn. B.5, we get

$$\dot{\sigma}_m = \mu_b + \mu_a \dot{\epsilon}_m \tag{B.22}$$

where μ_a, μ_b are complex expressions which can be computed from the known material/kinematic state at the beginning of the time step and from the strain increment tensor, **strainInc**, passed on to the user-material routine by ABAQUS/Explicit.

Using Eqns B.22 and B.3, the equivalent effective matrix strain rate over the time increment $t \rightarrow t + \Delta t$ is given by

$$\dot{\epsilon}_m = \frac{\dot{\epsilon}_m^{(n)} + \Gamma \frac{\partial \dot{\epsilon}_m}{\partial \sigma_m}|_{t_n} \mu_b \Delta t}{1 - \Gamma \Delta t \left(\frac{\partial \dot{\epsilon}_m}{\partial \sigma_m}|_{t_n} \mu_a + \frac{\partial \dot{\epsilon}_m}{\partial \sigma_m}|_{t_n} + \frac{\partial \dot{\epsilon}_m}{\partial \sigma_m}|_{t_n} \frac{\beta \sigma_m}{\rho c_p} \right)} \tag{B.23}$$

Appendix C

Rate-Tangent-Modulus Method for Integration of the Porous Constitutive Model in the Post-coalescence Regime

The post-coalescence behavior of voided microstructures is governed by the flow potential given by Eqn. 3.65 as

$$\Phi|_{c_+} = (\frac{\Sigma_G + 3/2\Sigma_h}{\sigma_m^L})^2 - 9/4(1-\chi^2)^2 C_F^2(\chi, W). \tag{C.1}$$

The upper-bound constraint factor C_F derived by Thomason (1985) has been modified by other investigators to match predictions of the onset of void coalescence by finite element calculations on void-containing unit-cells. We employ a constraint factor recommended by Benzerga (2001) as

$$C_F = F\left(\frac{1/\chi - 1}{W^2 + 0.1/\chi + 0.02/\chi^2}\right)^2 + G\chi^{-1/2} \tag{C.2}$$

where F are G are constants equal to 0.1 and 1.3 respectively. As earlier, define the equivalent local effective strain rate in the matrix for the time increment from t to

$t + \Delta t$ as

$$\dot{\epsilon}_m^L = (1 - \Gamma)\dot{\epsilon}_m^{L(n)} + \Gamma\dot{\epsilon}_m^{L(n+1)} \tag{C.3}$$

where the strain rate at the end of the time increment is given by

$$\dot{\epsilon}_m^{L(n+1)} = \dot{\epsilon}_m^{L(n)} + \Delta t \left[\frac{\partial \dot{\epsilon}_m^L}{\partial \sigma_m^L}\dot{\sigma}_m^L + \frac{\partial \dot{\epsilon}_m^L}{\partial \epsilon_m^L}\dot{\epsilon}_m^L + \frac{\partial \dot{\epsilon}_m^L}{\partial \theta_m^L}\dot{\theta}_m^L \right] |_{t=t_n} \tag{C.4}$$

The derivatives of the effective matrix strain rate with the effective matrix stress, strain and temperature are obtained from the constitutive model for the incompressible matrix material.

The rate of evolution of the matrix effective stress is determined by the plastic consistency relation for flow potential Eqn. C.1. Differentiating Eqn. C.1, we get

$$\frac{\partial \Phi}{\partial \Sigma_G}\dot{\Sigma}_G + \frac{\partial \Phi}{\partial \Sigma_h}\dot{\Sigma}_h + \frac{\partial \Phi}{\partial \sigma_m}\dot{\sigma}_m + \frac{\partial \Phi}{\partial \chi}\dot{\chi} + \frac{\partial \Phi}{\partial W}\dot{W} = 0 \tag{C.5}$$

As shown in Appendix B, the rate of evolution of the macroscopic effective Cauchy stress and the hydrostatic component of the macroscopic Cauchy stress tensor can be expressed in terms of the corotational derivative of the Cauchy stress. During the post-coalescence regime, we can show

$$\dot{\Sigma}_G = \frac{3C_\Sigma}{2\Sigma_G J} - \frac{E\Sigma_G \Lambda_1}{J(1+\nu)}\,\dot{\epsilon}_m^L \tag{C.6}$$

$$\dot{\Sigma}_h = \frac{C_I}{3J} - \frac{E}{J(1-2\nu)}\left(\Lambda_2 + \frac{\beta\alpha\sigma_m^L}{\rho c_p}\right)\,\dot{\epsilon}_m^L \tag{C.7}$$

where C_Σ and C_I are defined to be

$$C_\Sigma = \mathbf{I} : (\mathcal{C}^e : [\mathbf{D}]) \tag{C.8}$$

$$C_I = \mathbf{\Sigma}' : (\mathcal{C}^e : [\mathbf{D}]) \tag{C.9}$$

The coefficients Λ_1 and Λ_2 are obtained from Eqn. 3.69 as

$$\Lambda_1 = \frac{3}{2\Sigma_G}H(\chi, W, \lambda, \gamma) \tag{C.10}$$

$$\Lambda_2 = \frac{1}{2}H(\chi, W, \lambda, \gamma) \tag{C.11}$$

The rate of evolution of the ligament ratio χ is given by Eqn. 3.76 as

$$\dot{\chi} = \frac{3\gamma}{2}\frac{\lambda}{W}\left(\frac{6}{\pi\chi^2} - \frac{1}{2\gamma}\right)\Lambda_1\frac{2}{3}\Sigma_G\dot{\epsilon}_m^L + \frac{\chi}{2\gamma}\dot{\gamma} \tag{C.12}$$

The evolution of the shape factor γ is obtained by differentiating Eqn. 3.80 as

$$\dot{\gamma} = \frac{\gamma_f - \gamma_0}{1 - \chi_c}\dot{\chi} \tag{C.13}$$

Substituting Eqn. C.13 in eqn. C.12, we get

$$\dot{\chi} = \frac{\frac{3\gamma}{2}\frac{\lambda}{W}\left(\frac{6}{\pi\chi^2} - \frac{1}{2\gamma}\right)\Lambda_1\frac{2}{3}\Sigma_G}{1 - \frac{\chi}{2\gamma}\left(\frac{\gamma_f - \gamma_0}{1-\chi_c}\right)}\,\dot{\epsilon}_m^L \tag{C.14}$$

The evolution of the void aspect ratio W is given by Eqn. 3.78 as

$$\dot{W} = \frac{9}{4}\frac{\lambda}{\chi}\left(1 - \frac{4}{\pi}\frac{\gamma}{\chi^2}\right)\Lambda_1\frac{2}{3}\Sigma_G\dot{\epsilon}_m^L - \frac{W}{2\gamma}\dot{\gamma} \tag{C.15}$$

Substituting for $\dot{\gamma}$ from Eqn. C.13, we get

$$\dot{W} = \frac{\frac{9}{4}\frac{\lambda}{\chi}\left(1 - \frac{4}{\pi}\frac{\gamma}{\chi^2}\right)\Lambda_1\frac{2}{3}\Sigma_G}{1 + \frac{W}{2\gamma}\left(\frac{\gamma_f - \gamma_0}{1-\chi_c}\right)}\,\dot{\epsilon}_m^L \tag{C.16}$$

Solving for $\dot{\sigma}_m^L$ from Eqn. C.5, we get

$$\dot{\sigma}_m^L = \mu_b^L + \mu_a\dot{\epsilon}_m^L \tag{C.17}$$

where μ_a^L, μ_b^L are complex expressions which can be computed from the known material/kinematic state at the beginning of the time step and from the strain increment tensor, **strainInc**, passed on to the user-material routine by ABAQUS/Explicit.

Using Eqns. C.17 and C.4, the equivalent effective local matrix strain rate over the time increment $t \to t + \Delta t$ is obtained as

$$\dot{\epsilon}_m^L = \frac{\dot{\epsilon}_m^{L(n)} + \Gamma\frac{\partial\dot{\epsilon}_m^L}{\partial\sigma_m^L}\Big|_{t_n}\mu_b^L\Delta t}{1 - \Gamma\Delta t\left(\frac{\partial\dot{\epsilon}_m^L}{\partial\sigma_m^L}\Big|_{t_n}\mu_a + \frac{\partial\dot{\epsilon}_m^L}{\partial\sigma_m^L}\Big|_{t_n} + \frac{\partial\dot{\epsilon}_m^L}{\partial\sigma_m^L}\Big|_{t_n}\frac{\beta\sigma_m^L}{\rho c_p}\right)} \tag{C.18}$$

A similar formulation is used for computing the equivalent effective local matrix strain rate during the transition from pre-coalescence to post-coalescence ($\chi \to \chi + \Delta\chi$).

Bibliography

Bancroft, D. (1941), 'The velocity of longitudinal waves in cylindrical bars', *Physical Review* **59**, 588–593.

Becker, R., Needleman, A., Suresh, S., Tvergaard, V. and Vasudevan, A. K. (1989), 'An analysis of ductile fracture by grain boundary void growth', *Acta Metallurgica* **37**, 99–120.

Benzerga, A. A. (2000), *Rupture ductile des toles anisotropes*, These de Doctorat, Ecole Nationale Superieure des Mines de Paris, Paris, France.

Benzerga, A. A. (2001), 'Micromechanics of Coalescence in Ductile Fracture', *Journal of the Mechanics and Physics of Solids*.

Chree, C. (1889), 'The equations of an isotropic elastic solid in polar and cylindrical coordinates, their solutions and applications', *Cambridge Philosophical Society Transactions* **14**, 250–369.

Chu, C. C. and Needleman, A. (1980), 'Void nucleation effects in biaxially stretched sheets', *Journal of Engineering Materials and Technology* **102**, 249–256.

Dowd, B. A. (1996), 'Synchrotron X-ray Computed Tomography at the NSLS', *NSLS Newsletter*.

Dowd, B. A., Andrews, A. B., Marr, R. B., Siddons, S. P., Jones, K. W. and Peskin, A. M. (1999), 'Advances in X-ray Computed Microtomography at the NSLS', *Advances in X-ray Analysis.*

Garrison Jr, W. M. and Moody, N. (1987), 'Ductile fracture', *Journal of the Physics and Chemistry of Solids* **48**(11), 1035–1074.

Giovanola, J. H. and Kirkpatrick, S. W. (1993), Methodology for evaluating strength and fracture resistance of weldments using a local approach to fracture, *in* W. E. Pennell, ed., 'Pressure Vessel Integrity', Vol. 250, ASME, New York, pp. 1–15.

Gologanu, M. (1997), *Etude de quelques problemes de rupture ductile des metaux*, These de Doctorat, Universite de la Mediterranee, Marseille, France.

Gologanu, M., Leblond, J. B., Perrin, G. and Devaux, J. (2001), 'Theoretical models for void coalescence in porous ductile solids. I. Coalescence in layers', *International Journal of Solids and Structures* **38**, 5581–5594.

Gurson, A. L. (1977), 'Continuum theory of ductile rupture by void nucleation and growth: Part I-Yield criteria and flow rules for porous ductile media', *Journal of Engineering Materials and Technology* **99**, 2–15.

Hartley, K. A., Duffy, J. and Hawley, R. H. (1985), 'The torsional Kolsky (split-Hopkinson) bar', *Metals Handbook,* 9^{th} *Ed.* **8**, 218–228.

Herman, G. T. (1980), *Image Reconstructions from projections: The fundamentals of computerized tomography,* Academic, New York.

Hval, M., Thaulow, C., Lange, J. H., Hoydal, S. H. and Zhang, Z. L. (1998), 'Numerical modeling of ductile fracture behavior in aluminum weldments', *Welding Journal* **77**(5), 208–217.

Kinney, J. H. and Nichols, M. (1992), 'X-ray tomographic microscopy using synchrotron radiation', *Annual Review of Materials Science* **22**, 121–152.

Koplik, J. and Needleman, A. (1988), 'Void growth and coalescence in porous plastic solids', *International Journal of Solids and Structures* **24**(8), 835–853.

Leblond, J. B., Perrin, G. and Devaux, J. (1994), 'Bifurcation effects in ductile metals with damage delocalization', *Journal of Applied Mechanics* **61**, 236–242.

Lee, B. J. and Mear, M. E. (1992), 'Axisymmetric deformation of power-law solids containing a dilute concentration of aligned spheroidal voids', *Journal of the Mechanics and Physics of Solids* **40**, 1805–1836.

Lee, B. J. and Mear, M. E. (1999), 'Evolution of elliptical voids in power-law viscous solids', *Mechanics of Materials* **31**, 9–28.

Lee, E. H. (1969), 'Elastic-plastic deformation at finite strain', *Journal of Applied Mechanics* **36**, 1.

McClintock, F. A. (1968), 'A criterion for ductile fracture by growth of holes', *Journal of Applied Mechanics* **35**, 363–371.

Needleman, A. (1972), 'Void growth in a elastic-plastic medium', *Journal of Applied Mechanics* **39**, 964.

Needleman, A. and Tvergaard, V. (1994), 'Mesh effects in the analysis of dynamic ductile crack growth', *Engineering Fracture Mechanics* **47**(1), 75–91.

Nemat-Nasser, S., Guo, W. and Kihl, D. P. (2000), 'Thermomechanical response of AL6XN stainless steel over a wide range of strain rates and temperatures', *International Journal of Solids and Structures.*

Pan, J., Saje, M. and Needleman, A. (1983), 'Localization of deformation in rate sensitive porous plastic solids', *International Journal of Fracture* **21**, 261–278.

Pardoen, T. and Delannay, F. (1998), 'Assessment of void growth models from porosity measurements in cold-drawn copper bars', *Metallurgical and Materials Transactions* **29A**, 1895–1909.

Pardoen, T. and Hutchinson, J. W. (2000), 'An extended model for void growth and coalescence', *Journal of the Mechanics and Physics of Solids* **48**, 2467–2512.

Peirce, D., Shih, C. F. and Needleman, A. (1984), 'A tangent modulus method for rate dependent solids', *Computers and Structures* **18**, 875.

Pijaudier-Cabot, G. and Bazant, Z. P. (1987), 'Nonlocal damage theory', *Journal of Engineering Mechanics, ASCE* **113**, 1512–1533.

Pochhammer, L. (1876), 'On the propagation velocities of small oscillations in an unlimited isotropic circular cyliner', *Journal fur die Reine und Angewandte Mathematik* **81**, 324–326.

Radon, J. (1917), 'Uber die bestimmung von funktionen durch ihre integralwerte langs gewisser mannigfaltigkeiten', *Ber. Verh. Sachs. Akad. Wiss. Leipzig* **69**, 262–277.

Reed, P. R. (1988), Austenitic stainless steels with emphasis on strength at low temperatures, *in* J. L. Walter, M. R. Jackson and C. T. Sims, eds, 'Alloying', ASM International, pp. 225–256.

Rice, J. R. and Tracey, D. M. (1969), 'On the ductile enlargement of voids in triaxial stress fields', *Journal of the Mechanics and Physics of Solids* **17**, 201–217.

Sovik, O. P. and Thaulow, C. (1997), 'Growth of spheroidal voids in elastic-plastic solids', *Fatigue and Fracture of Engineering Materials and Structures* **20**, 1731–1744.

Thomason, P. F. (1985), 'Three-dimensional models for the plastic limit-loads at incipient failure of the intervoid matrix in ductile porous solids', *Acta Metallurgica* **33**(6), 1079–1085.

Thomason, P. F. (1998), 'A view of ductile fracture modelling', *Acta Metallurgica* **21**, 1105–1122.

Tvergaard, V. (1981), 'Influence of voids on shear band instabilities under plane strain conditions', *International Journal of Fracture* **17**, 389–407.

Tvergaard, V. (1991), Material failure by void growth, *in* J. W. Hutchinson and T. Y. Wu, eds, 'Advances in Applied Mechanics', Vol. 27, Academic Press Ltd., pp. 83–147.

Tvergaard, V. (1997), 'Studies of void growth in a thin ductile layer between ceramics', *Computational Mechanics* **20**, 186–191.

Tvergaard, V. and Needleman, A. (1984), 'Analysis of the cup-cone fracture in a round tensile bar', *Acta Metallurgica* **32**, 157–169.

Tvergaard, V. and Needleman, A. (1997), 'Nonlocal effects on localization in void-sheets', *International Journal of Solids and Structures* **34**(18), 2221–2238.

Wagoner, A. (2001), Ph. D. Thesis, Brown University, Providence, RI.

Xia, L. and Shih, C. F. (1995), 'Ductile crack growth-I. A numerical study using computational cells with microstructurally-based length scales', *Journal of the Mechanics and Physics of Solids* **43**(2), 233–259.